POLITECNICO DI TORINO

AEROSPACE AND MECHANICAL DEPARTMENT

Master Course in Aerospace Engineering

Master Thesis

Outer Heliosphere: Investigation on the signal fluctuations of the data collected by the Voyager probes

Supervisor:
Prof. Lamberto RONDONI

Candidate:
Alessandra SACCO

ACADEMIC YEAR 2022/2023

A mio Fratello, A mia Madre
A Voi che ci siete sempre stati
A Voi che siete con noi da lassù
A Voi a cui non è stato consentito essere Libere e Indipendenti

Abstract

The following thesis analyses deep-space data recorded by the Voyager 1 and Voyager 2 probes, covering the period between January 1, 2016, and December 31, 2020. These data were collected at distances ranging from 133.57 to 151.41 astronomical units (AU) for Voyager 1 and from 109.98 to 125.83 AU for Voyager 2. The data were provided by NASA's @Omniweb database and include information on the magnetic field in its three components and magnitude, as well as data related to three proton parameters, as velocity, density, and temperature, when available.

Based on the available data, the investigation aims to contribute to predicting the future trends, with the goal of identifying the positions of the probes within the Interstellar Medium. Two methods of analysis are employed: the Fluctuation Theory, which examines the oscillations of variables over time, and a simple Fourier interpolation, which allows for the Fourier Transform of the signal into a function of frequency and thus, the power of the signal.

The thesis begins by examining the current state of the probes, including their positions and the paths they have reached. The data are contextualized through estimates of different regions of the Interstellar Medium found in the literature, based on energy conservation law calculations.

The core of the paper is the implementation of the two analysis methods. In the chapter applying Fluctuation Theory, trends in both the mean and the anomaly (deviation) of individual measurements from the data mean over hourly intervals of varying durations are studied to assess the probability distribution and density of probability distribution, both analytically and asymmetric Laplace probability distribution. It is noted that the curves narrow and lengthen as the duration of the averaging interval changes. Additionally, the analysis of different components under examination results in varying numbers of peaks in the probability density function (PDF).

Subsequently, calculations of variables, fluctuations, interpolation of the PDF at the identified values, and the scale factor between probability fluctuation functions are performed. This aims to estimate, through statistical indices, the evolution of data to identify the point at which the appropriate magnetic field value can indicate the conclusion of the Outer Heliosphere region, thereby officially marking the probes' exit from the solar system.

In the chapter dedicated to Fourier analysis, the hypotheses from the previous study are confirmed. There are sharp jumps in magnetic field values near critical positions (AU), and after estimating the transform, which allows for the evaluation of data as a function of

frequency (highlighting periodic trends), information about the signal's decreasing power spectrum is obtained.

In conclusion, from the data collected by the two probes, two critical periods are observed in which distinct variations in magnetic field magnitude and proton-related parameters occur. Both probes experience a decrease in magnetic field values, but Voyager 1, the more distant of the two, experiences a second, more significant drop, which could signify the definitive exit from the solar system.

Acknowledgments

Con il termine del mio corso magistrale di Ingegneria Aerospaziale, tengo a ringraziare le persone che mi sono state accanto in questi anni, intensi ed impegnativi, questa laurea è dedicata a voi, perchè, per qualsiasi motivo sia, questa laurea è anche vostra.

Ringrazio innanzitutto la mia famiglia perchè ci sosteniamo sempre ed insieme siamo fortissimi, in grado di fronteggiare qualsiasi situazione con amore incondizionato; ringrazio mia madre che è sempre in prima fila, ti supporta e ti sopporta a qualunque costo, è il fan numero 1 di mio fratello e me ed è grazie a lei che la nostra piccola famiglia vince ogni giorno. Ringrazio mio fratello che è compagno di vita, amorevole e testardo, che ascolta sempre, anche se spesso straparlo e nessuno capisce quello che dico. Sono fiera che tu stia seguendo la strada dei tuoi sogni: il sereno arriverà, raggiungerai tutti i tuoi obiettivi ed avrai un gran successo!

Ringrazio mia zia Daniela, che per me è come una seconda mamma, persona genuina e fantastica che è sempre stata al nostro fianco, in qualsiasi situazione, e sempre lo sarà (soprattutto per mangiare un panino dopo lezione); ringrazio mia cugina Francesca, piccola di casa, ma più grande di quello che dimostra, che nonostante viva al capo opposto della Terra, non fa mai mancare un sorriso o una parola dolce.

Ringrazio Nonna perchè c'è sempre e soprattutto ci prova pur essendo convinta che io sia in seconda superiore; ringrazio Nonno perchè lo sento sempre con me.

Ringrazio anche il cucciolino di casa Spid, che tanta allegria e compagnia ci regala ogni giorno.

Ringrazio tutti i miei amici, sia quelli di una vita, sia chi ho appena conosciuto, siete tutti preziosi. In particolare, ringrazio Arianna, ci siamo prese per mano a 6 anni all'estate ragazzi di Caramagna e non ci siamo più lasciate, tanto diverse, tanto uguali, ma sempre insieme. Ringrazio Aicha che è Aicha, che sa e che tutto ci siamo sempre dette, la mia anima gemella, e su cui non c'è nulla da aggiungere; grazie per le passeggiare notture, le vacanze, lo studio condiviso, le confidenze, i pianti, le risate e il gatto.

Ringrazio Aurora, che ha preso il volo, che è folle, avventuriera belgique ed è sempre sul pezzo: c'è sempre dovunque tu sia (ma soprattutto ovunque lei sia) e con lei non ti stanchi mai. Sono fiera di te.

Ringrazio Marco, Amico prezioso, confidente, spalla e super supporter, a cui tutto puoi dire e tutto viene custodito; talmente abbiamo parlato di spazio che potrebbe predere la pergamena con me anche lui. Aggiungo che è la miglior persona con cui condividere vacanze, cibo e meme.

Ringrazio Caffa, il cui umore e battute fanno impazzire, sei e sarai sempre il primo con cui guardare Sanremo. Le canzoni dei cartoni cantate insieme sono impossibili da contare. Ringrazio Ele, sempre presente, sempre dolce, è una delle persone che non dovrebbero mancare nella vita di nessuno. Ringrazio Pets, uomo impegnato, ma sempre disponibile, con cui parlare per ore: sempre un piacere lamentarsi insieme, soprattutto del *oli; sono sicura che sarà la svolta dell'energetica.

Ringrazio le mie amiche, conosciute all'università, senza cui supporto non avrei raggiunto questo traguardo; ringrazio Letizia e Carlotta, conosciute il secondo giorno di università, perchè cominciammo martedì ahah. Abbiamo intrapreso strade diverse ma sempre con interesse reciproco e supporto una per le altre, sono felice di avervi vicino e amo pranzare con voi.

Ringrazio Gaia, perchè la mia laurea è anche sua, senza lei, i mille giorni di studio, i sabati da Biraghi e le domeniche a casa sua non avrebbero fruttato così bene; siamo partite da piccole aspiranti ingegnerine aerospaziali il secondo anno di triennale e siamo arrivate fino qua (ad avere finito gli esami a luglio!!!!!). Grazie per aver condiviso gli appunti, i cappuccini alla soia, le risate, le lamentele, i viaggi fino a Lingotto Fiere e le foto di Susi. E il pranzo gramissimo. Nei contenitori verdi, soprattutto.

Ringrazio il Politecnico perchè mi ha dato modo di sperimentare e capire ciò che voglio essere e fare nella vita, mettendomi davanti a sfide intense e dandomi gli strumenti per fronteggiarle: ho capito che saper pensare è il sale della vita, qualsiasi sia il tuo obiettivo.

Infine ringrazio il gentilissimo prof. Lamberto Rondoni per la possibilità di cimentarmi in qualcosa di diverso per me e di avermi accettato per svolgere una tesi in matematica pur non essendo il mio campo; è stata una sfida, ma penso sia stata vinta, e soprattutto che sia stata estremamente stimolante. Spero che la collaborazione prosegua.

Grazie a tutti.

Contents

List of Figures

List of Tables

Chapter 1

Planetary Mission: Voyager

1.1 Introduction

In this first chapter, the interstellar mission par excellence, 'The Voyager Interstellar Mission' is introduced , by retracing each phase, since the very first insight. Against all expectations, it was to become the most successful and epic planetary mission of all time, up to now.
To find out and to understand the reasons that brought to the mission concept, it's needed to take a look back to late 60s, when the human being was running for reaching the space. As the space economy were emerging, after all new space studies, NASA and JPL were intended to embark on a planetary mission, aimed to observe in the nearest possible way multiple gas giants.
In sequence, from the nearest to the Sun, to the furthest : Jupiter, Saturn, Uranus and Neptune.

1.1.1 Planetary Grand Tour

Gary Flandro (1934) is an American aerospace engineer, who worked at JPL during summer 1965. His task was to study new trajectories for planet exploration through the solar system inasmuch as the performance of spacecrafts were strictly related to thrust, energy consumption and s/c weight.
Orbital maneuver require a perfectly-defined Δv: it's limited, and the farther you want to fly, the higher it turns out.
Crucial was his innovative discovery, that he personally defined "A Once-in-a-Lifetime Alignment": it consists in a in-depth study based on both the minimization of the energy required for flight, achieved through close flybys, based on the slingshot effect, which leverages the gravitational field of a specific planet to gain velocity and momentum, and on the alignment (launch window) of the target planets, which occurs every 175 years.
Fly by maneuver provides time reduction in relation to the distances between planets: so average mission time is scaled down and scientists can reach data faster.
These conditions led NASA to formulate a new mission proposal, named "Planetary Grand

Tour".
The most successful projects were Pioneer 10,11 probes and Voyager 1,2 probes.

Figure 1.1: Grand Tour poster.

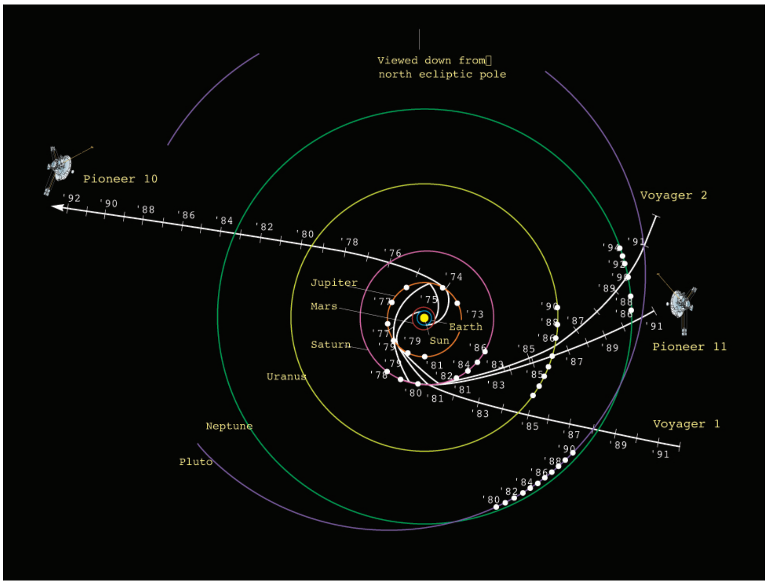

Figure 1.2: All probes trajectory.

1.1.2 Fly-by

Before delving into the specific evolution and subsequent space missions, we need a brief digression to explain what a fly-by is and how it works.
A classic interplanetary mission is divided into three phases according to the "patched-conics" model: planetocentric (subject to the gravitational influence of the departure planet) where an hyperbolic escape maneuver is often chosen , heliocentric (subject to the sphere of influence of the Sun) where ad efficient Hohmann maneuver performed, and final planetocentric (where the probe is subject to the sphere of influence of the target planet).
It's in this final phase that the fly-by maneuver is executed. This occurs when a spacecraft enters the sphere of influence of a planet and neither impacts the planet nor goes into orbit around it, but continues its hyperbolic trajectory until periapsis and exits the sphere of influence. When the periapsis is in the direction of the planet's motion, it's called a leading-side flyby, otherwise, it's a trailing-side flyby.

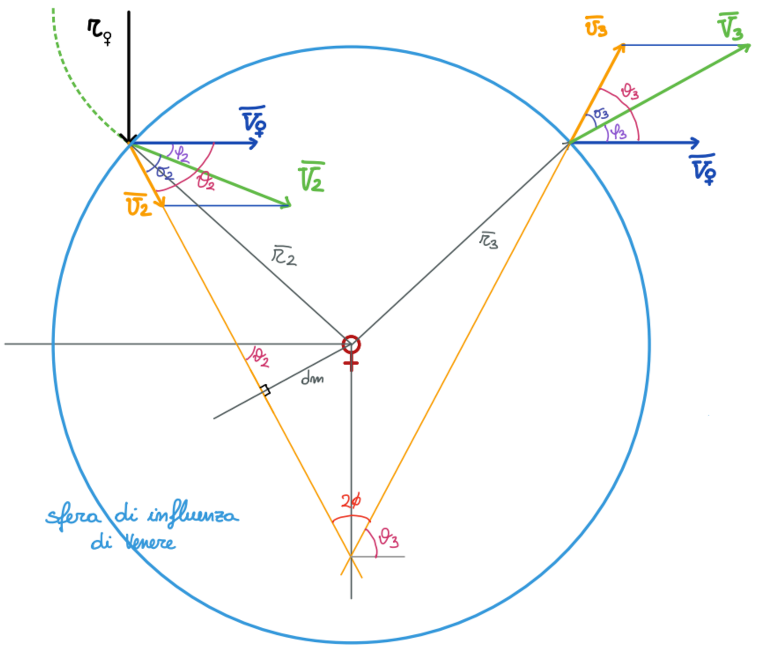

Figure 1.3: Trailing-side flyby.

Specifically, to reach greater distances and move as far away as possible from the Sun , the spacecraft needs an increase in energy in its exit trajectory from the planet without using engines (minimizing energy consumption). This is achieved through a trailing-side flyby.
Assuming that all planet orbits are circular and the planetocentric sphere of influence is smaller than the distance to the Sun, it's clear that the enter radius is equal to the exit radius.

$$|\bar{r_3}| = |\bar{r_2}| \tag{1.1}$$

Subsequently trigonometric relationships provide speed magnitude, knowing planets circular velocity.

$$|\bar{V_3}| = |\bar{v_3}| + |\bar{V}_{planet}| \tag{1.2}$$

$$V_3 = \sqrt{{v_3}^2 + {V_{planet}}^2 - 2 v_3 V_{planet} \cos{(\pi - \theta_3)}} \tag{1.3}$$

Once the direction is defined by angular inclination, as $\sigma_3 = \arcsin{(\frac{V_{planet}}{V_3} \sin{\theta_3})}$ and $\phi_3 = \theta_3 - \sigma_3$; momentum increase is demonstrated: $\cos{\phi_3} > \cos{\phi_2}$ so $h_3 > h_2$.

1.1.3 Pioneer Program

The Pioneer probes were some of the first to be produced for the aforementioned space program and were developed by NASA's Ames Research Center. Multiple Pioneer probes were designed, but the only ones that actually completed their mission were Pioneer 10 and 11, single-spin spacecraft launched in 1972 and 1973. They were each equipped with a golden record, which contains various information about Earth and humanity.

The success of the mission was primarily due to experimentation with previous probe models which helped in selecting the right modules and meeting the space requirements. These probes were intended to be capable of:

- photographing Jupiter and its moons, including polar-metric imaging;
- providing observations in the infrared and ultraviolet spectra;
- detecting asteroids and meteoroids and cataloguing data;
- stabilizing the composition of charged particles;
- measuring magnetic fields, plasma streams, galactic cosmic rays, and zodiacal light during their operational phase.

These measurements aimed to improve our understanding of planetary masses and distances.
Pioneer probes observed Jupiter and multiple asteroid on their path; however Pioneer 11 transmitted its last signal in September 1995, while Pioneer 10 one was in January 2003: it's believed that both Pioneer 10 and Pioneer 11 are currently drifting through space.

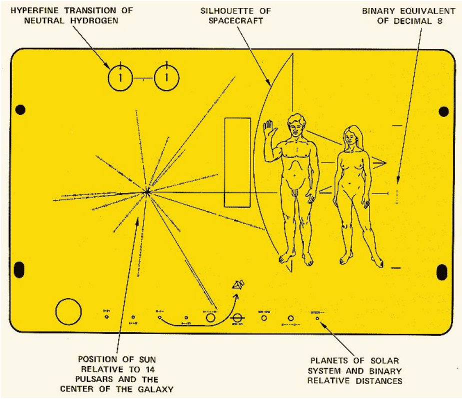

Figure 1.4: Pioneer 10/11 Golden Record.

1.1.4 Voyager Interstellar Mission (VIM)

The main mission of Planetary Grand Tour was VM: Voyager Mission.
The Mariner program was the very first project conducted by NASA to explore solar system planets at the beginning of 60s. Several probes were launched and many other program started between 1962 and late 1973, such as Pioneer ones and Mariner 4, a Mars flyby mission brought in 1964: in late 70s NASA engineers were able to develop such engineered spacecraft that two twins probes were added to The Mariner program. Firstly named Mariner 11 and Mariner 12, than Voyager 1 and Voyager 2, due to their huge structural efficiency, in comparison to previous mariner probes. Suddenly as Marine-based probes, Galileo and Magellan were designed, while the evolution of the Mariner probes series culminated into the Cassini–Huygens probe.

Voyager 1 and Voyager 2 were respectively launched on 5th September 1977 and on 20th August 1977 from Cape Canaveral. Designed to explore the edge of the solar system by performing flyby maneuvers over gas giants and ice giant, they has visited as many planets, rings, and satellites, nor has provided as many new insights into the planets.
Especially Voyager 1, the furthest, completed flyby around Jupiter and Saturn, while Voyager 2, the slower, completed flyby around all four giants.
In 1990s the Voyager program became the "Voyager Interstellar Mission" (VIM): after crossing Neptune orbit, both probes continued their cruise to the Outer Heliosphere, Interstellar Medium and the unknown.

1.2 Mission objective

The mission objective of the extended Voyager Mission is deep-explore beyond Our Solar System edges. The purpose is examine particulates matter properties as emissions, density, speed and frequency, compare magnetic field components to magnitude, measure gravitational flow to ensure solar winds effects: these measurements should help to comprehend how the universe is layered, if similar environment to our solar system exists or the opportunity to meet extraterrestrial organisms.
Although the primary task remain to find out how physics behaves outside the Heliosphere: indeed Galactic Cosmic Rays have great influence outside the heliopause, while their behaviour is anomalous through it and their effect is almost completely shielded outside the Solar System.

1.3 Solar system structure

A general overview is required to analyses and describe Voyager mission asset: we will give a deeper look on both Our Solar System and the Outer Heliosphere zone to the Interstellar Medium.

1.3.1 Our Solar System

The Sun is located in the origin of the Solar System, while the planets orbit on elliptic trajectories.
Between 1608 - 1619, Johannes Kepler formulated planetary motion laws, which describe how planets and their satellites and moons move around the primary star. The First law states that the Sun is fixed in a focus, while the Second and the Third respectively state that planets cover equal areas in equal times and planets revolution time is proportional to the semi-axis magnitude, indeed the bigger the orbit is, the longer the revolution time is. Following the second law, at the apogee, revolution speed decreases in order to the short sector path, otherwise at perigee.

Planets are listed from the nearest to the furthest: Mercury, Venus, Earth, Mars, Jupiter, Saturn, Uranus and Neptune; Pluto was downgraded to draft-planet.

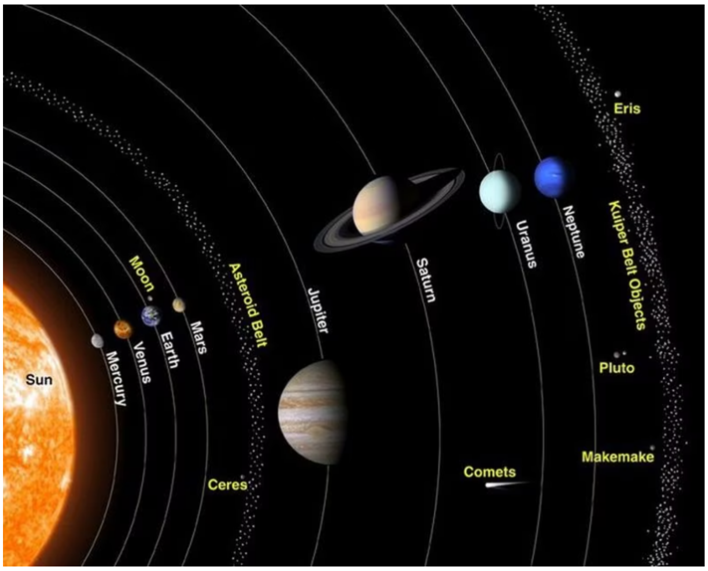

Figure 1.5: Solar system.

Revolution time was the key to define the alignment of the planets: relative position and launch window to Earth have given essential information to determinate when the probes had to be launched.
The following are the values of the planets parameter.

Planets orbital parameters						
Target planet	n (rad/s)	a (AU)	e	T_{Sid} (y)	T_{Syn} (y)	$D_{toEarth}$(AU)
Mercury	0.387	0.6935	0.4419	0.289	0.317	0.981
Venus	0.723	0.8617	0.1605	0.400	1.599	0.594
Earth	0.942	1	0.0167	-	1	-
Mars	1.524	1.2618	0.2075	0.709	2.135	1.594
Jupiter	5.202	3.1012	0.6775	2.731	1.092	5.177
Saturn	9.548	5.2741	0.8104	6.056	1.035	10.492
Uranus	19.135	10.0674	0.9007	15.972	1.012	20.120
Neptune	30.011	15.5055	0.9355	30.529	1.006	29.027
Pluto	39.289	20.1446	0.9504	45.208	1.004	39.565

Table 1.1: Solar System planets: parameters and Sidereal and Synodic period

1.3.2 Outer Heliosphere and Interstellar Medium

Between Solar System and external universe, [18] some terminal layers occur. The thickness of each layer is not univocal: the probes discovered that each zone starts with a rapid variation of measured data and its is extended into different range, depending on which direction the probe is measuring.

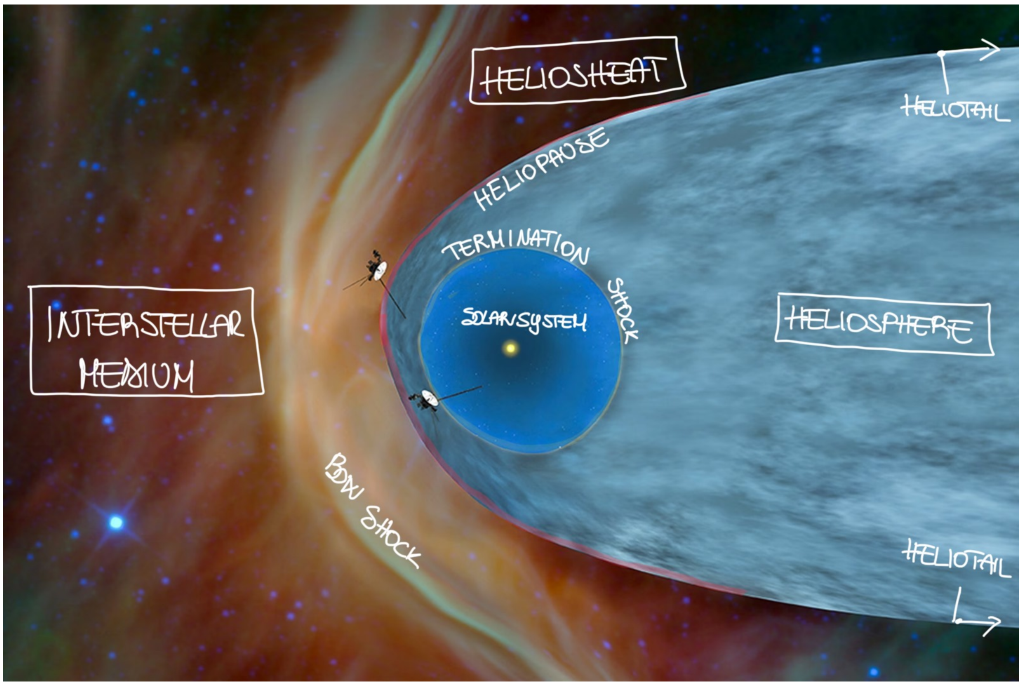

Figure 1.6: Outer Heliosphere layering.

Firstly the Termination Shock occurs [6]: it is where solar wind particles start to slow down, producing a subsonic stream. Than, Outer Heliosphere continues up to Heliopause, here solar wind pressure is weaker than the stellar one.
Please note: the Solar System motion through the universe origins an Heliosphere trail, called Heliotail; the pressure flux variation leads to weak shocks.
Crossed Heliopause, the probes are located in the Heliosheath in which the solar wind continues to slow down and to compress. At the end, there's the Bow Shock, a strong shock due to solar wind particles pushing against the stellar wind stream.
As I'm explaining in the next chapter, it's seems that Voyager 1 entered the beginning of these zone, while Voyager 2 not yet.

Beyond Bow Shock, the Interstellar Medium stretches.

1.4 Mission characteristic

The Voyager primary mission began in 1977 with the launch of Voyager 2 probe and ended in 1989 with the Voyager 2 fly-by of Neptune: the probes accomplished their close fly-bys of the designed planets in around 12 years and gained several firsts. Voyager 1 and Voyager 2 were respectively at a distance from the Sun of about 41 AU and 32 AU.
Subsequently The VIM (Voyager Interstellar Mission) started [26]: it can be divided into three main phases, the first began after Voyager 2 fly-by of Neptune, and the last is ongoing.

- the Termination Shock phase;
- the Heliosheath exploration phase;
- the Interstellar exploration phase.

Each zone is characterized by properties mentioned above: however the crucial is the Termination Shock phase, which decrees the escape of the Solar System. Going into more detail, Voyager 1 escaped the Solar System at a speed of 3.59 AU/year, in the direction of Solar Apex, 35.1° out of the ecliptic plane to the north; whereas Voyager 2 escaped at 3.31 AU/year, 47.98° out of the ecliptic plane to the south.

Considering current probes condition, their instruments will have enough power until 2025; then, the probes won't transmit anymore and drift through the Oort cloud for many long time.

1.4.1 Mission timeline: Voyager 1

Voyager 1 was launched after its twin, but it undertook a shorter and faster way to Jupiter, so in 1989 it has exited the asteroid belt earlier than Voyager 2 [15]. Its firsts and main accomplishments are reported below:

- The probe started photo-shooting Jovian planets in April 1978: it took spectacular images of Jupiter and its moons, Amalthea, Io, Europa, Ganymede and Callisto and discovered a thin ring around Jupiter and two new moons, later named Thebe and Metis.

- On 5th March 1979, once an attitude and position re-arrangement was set, the Jupiter flyby were made.

- As a result, the spacecraft reached Saturn and discovered a new G-ring and five more moons : Mimas, Enceladus, Tethys, Dione and Rhea, since the largest, Titan, was already known.

  Titan was found to have a pretty similar environment to Earth: mostly of the atmosphere is composed by nitrogen and pressure and temperature are only 1.6 times Earth's ones. Therefore multiple chemical reaction may be possible and it was found that life could grow on it.

- Through the exploitation of Saturn gravitational field, on 12th November 1980 the probe took Saturn fly-by: Despite its twin probe, Voyager 1 approached only two outer planets. It only crossed Uranus and Neptune' orbits and flew over the asteroids belt to escape the Solar System.

- On 1st January 1990 Voyager Interstellar Mission officially started: the probe began collecting data about local environment, as magnetic field data, matter particulates properties, speed and pressure of the solar wind and gravitational field effect on it.

- On 17th February 1998 Voyager 1 had broken the record to be the most distant spacecraft, launched by the mankind (and NASA).

- On 16th December 2004, Voyager 1 gained the first to be the first spacecraft to cross the Heliosphere, at a distance of 94 AU: it started exploring Heliosheat.

- On 16th August 2006: it reached 100 AU.
- On 1st August 2012: it entered in the VLIM (very local interstellar medium), becoming the very first human-made vehicle to lead into interstellar medium.
- In the future, the probe will face to Oort cloud, which is a theorized truly extended spherical shell, made of comets, between 2000 - 200000 AU.

1.4.2 Mission timeline: Voyager 2

Voyager 2 is the first to be launched through the space in August 1977: despite that, its trajectory was the less efficient and it reached Jovian planets after its twin. Moreover Voyager 2 was the first and only probe to observe all four outer planets, indeed it sent close images of nor Jupiter and Saturn, but also about Uranus and Neptune and their moons [30].
The greatest benefits of a second space exploration, after Voyager 1, was the more accurate pictures collected by Voyager 2, related to giant planets, their moons, asteroids and the tracking of changing atmospheric conditions on each planets.
Most relevant accomplishments are listed below:

- On 24th April 1979, Voyager 2 began its imaging mission, taking closely photos around Jupiter and mapping its moons, Europa and Io.
- Thus it discovered a 14th moon: Iapetus, and a third component to the planet's rings.
- On 9th July 1979, it made the Jupiter fly-by, transmitting new data about few atmospheric changes, as a drift in the Great Red Sport.
- After two years, Voyager 2 reached Saturn and it took deeper images of its rings (particularly interesting were A and F rings).
- On 26th August 1981 it made its Saturn fly-by, with a large degree trajectory, due to fly to Uranus. Its speed was 13 km/s. It needed an huge attitude control because of friction effect of dust grains.
- On 4th November 1985 long-range observations of Uranus began: during fly-by the probe will have only 5.5 hours to observe at short range.
- On 24th January 1986, Voyager 2 led to Uranus fly-by: it discovered 10 new moons (called Puck, Portia, Juliet, Cressida, Rosalind, Belinda, Desdemona, Cordelia, Ophelia, and Bianca)and two new ring in addition to the "previous" nine, which was found to be highly different in shape and color . Then, it collected data about Uranus' environment, which was primarily composed by boiling oceans, whereas magnetic field component is a bit swerved. It also returned images of five Uranus' larger moons : Miranda, Oberon, Ariel, Umbriel, and Titania.

  In general, Uranus seems featureless and harsh.

- On 14th February 1986, Voyager 2 performed the largest asset correction, to fly to Neptune.
- On 25th August 1989, during Neptune fly-by, the probe recorded six new moons, Proteus, Larissa, Despina, Galatea, Thalassa, and Naiad, carefully scanned the three features in the planetary clouds (the Lesser Dark Spot, the Great Dark Spot, and Scooter), discovered four rings and reported images of Triton, Neptune's largest moon.
- In conclusion, the "Grand Tour" was concluded and it started its voyage over the Outer Heliosphere.
- During early 00s, Voyager 2 provided important LECPs data and continued transmitting UV and particle fields data.
- On 30th August 2007, Voyager 2 passed the Termination Shock and entered the next phase.
- On 10th December 2018, it officially entered the Interstellar Medium, after passing over the Heliosheat.
- On 8th July 2019, the probe fired up its thrusters, to correctly point antennas to Earth.
- On 20th August 2022: Voyager 2 reached 45 years in space.
- In summer 2023, due to incorrect signal command, the probe lost its pointing to Earth. The spacecraft was still operating , due to signal carrier detection, but JPL team sent instructions to lead its pointing-Earth antennas to retake on the correct position anyway: in early August the trial was successful and the probe started over to transmit telemetry and science data.

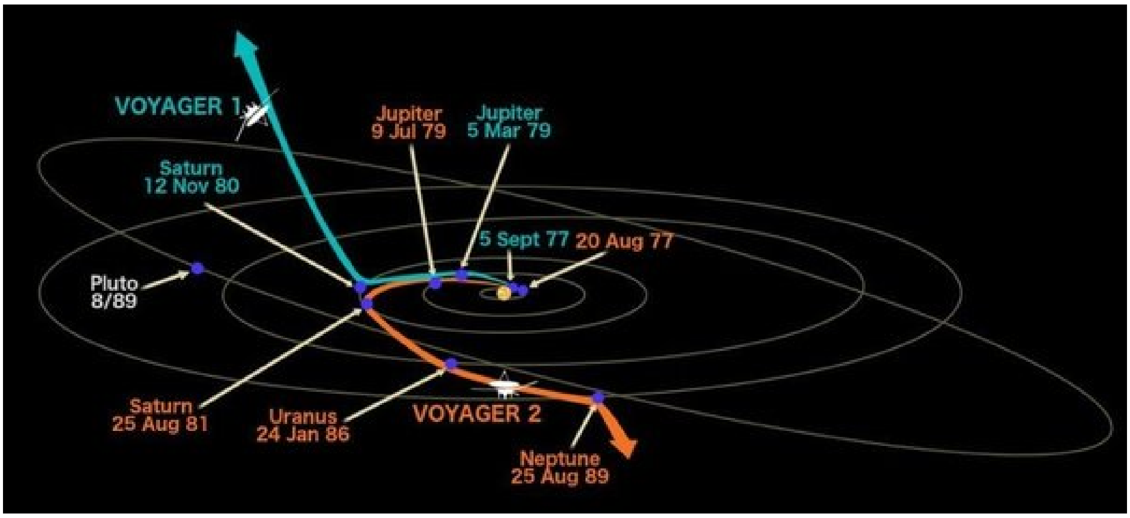

Figure 1.7: Voyager 1 and 2 "Grand Tour".

Chapter 2

Voyager Probes

2.1 Probe characteristics

After the previous mission description, we will analyze the structure and on-board instruments that permitted Voyager probes work for more than 45 years.
The 1A phase mission analysis identified three possible configurations (A, B, C): the final design became the combination of the different approaches; particularly, configuration B properly defined the mechanical probes design.

2.1.1 Spacecraft design

Both Voyager probes weight 773 kg, carry a 105 kg payload of science instruments and are composed by all the necessary subsystems to perform the mission .

Computer and processing subsystem

Voyager 1 and Voyager 2 have identical computer systems: there are three different computer types on, two of each used for redundancy. Computers were built from CMOS and TTL (medium-scale CMOS integrated circuits) and discrete components, mostly from Texas Instruments.
The central controller of the spacecraft, has two 18-bit and processors equipped with non-volatile "plated-wire" memory; during most of the Voyager mission the two CCS computers on each spacecraft were used non-redundantly to increase the command and processing capability of the spacecraft.
The Flight Data System is two 16-bit machines with modular memories.

Attitude and position control subsystem

Probes are three-axis-stabilized spacecraft, based on real-time and close loop algorithms: very similar to Mariner C's subsystem. It provides reorientation, orbit acquisition, inertial control and retro-propulsion, once mode control requires.

Each control mode needs several sensors and actuators switched on, respectively aimed to collect data and follow the control system command . Primary components are:
SENSORS:

- Coarse Sun Sensors;
- Fine Sun Sensors;
- Star Sensors;
- Rate Mode Gyro;
- Attitude Mode Gyro;
- Earth Sensors;

ACTUATORS:

- Gas Jets;
- Jet Vanes;
- LITVC;

Propulsion subsystem

Propulsion subsystem main function is generate thrust and required couples: for space operations, like orbit injection or attitude and position control or in-orbit operations, mono-propellant nitrogen gas (hydrazine) thrusters are fired up, that produce the primary control couples; whereas retro-propulsion is obtained with solid propellant and liquid injection.

Characteristics of the engines	
Specific impulse	230 sec
Initial thrust	50 lb
Minimum velocity	increment 0.1 m/sec
Pressurant gas	He
Pressured gas	N2H4 (Hydrazine)

Table 2.1: Midcourse propulsion parameters

Spherical storage tanks are provided for mono-propellant, they are linked to valves and pressure regulators and transducers, before entering thrust nozzles. the advantage of Voyager system is producing twice the required impulse due its sizing.

Power subsystem

The power subsystem consists of:

- the solar array: installed on six identical panels, each panel having 39 two parallel-connected sections. There's a total of 38,976 solar cells for the array.
- the solar array shunt voltage limiter;
- the secondary batteries;
- the battery regulators;
- the power conditioning equipment;
- the power control unit.

Checkout procedures was found simpler with the identical spacecraft bus configuration on the Saturn-Centaur launch vehicle.

Thermal subsystem

The main purpose of these subsystem is make thermally insulated all electronic on-board component and payload instruments.
Moreover thermal regulators and heaters were used to control heat and energy flux through propulsion system.

Communication subsystem

The uplink communications [30] are executed via S-band microwave communications while the downlink communications are performed by an X-band microwave transmitter on board the spacecraft, with an S-band transmitter as a back-up. Communications between ground station and probes has carried out using a 3.7-meter high-gain antenna: it has a beamwidth of 0.501° for X-band, and 2.301° for S-band. The high-gain antenna dish is attached to the hollow decagonal electronics container, on spacecraft low electronic box..
Because of the inverse-square law in radio communications, the digital data rates used in the downlinks from the Voyagers have been continually decreasing the farther that they get from the Earth: some measures were taken on the ground along the way to reduce the effects of the inverse-square law. In between 1982 and 1985, the diameters of the three main parabolic dish antennas of the Deep Space Network were increased from 64 to 70 m for gathering weak microwave signals. As reported on NASA website [15].

Data Handling subsystem

The subsystem lend large data storage: telemetry data and payload data are collected faster than other spacecrafts designed before. Primary structure has spacecraft DAE, signal conditioner, PCM encoder, several storage and DAE, modulator, receiver and transmitter related to the capsule.

Figure 2.1: Voyager probe.

More information about configuration choice can be found in "Voyager spacecraft, Summary - phase 1A study report, JPL: Pasadena CA, Vol. 1, 30/06/1965"

2.1.2 Payload: Scientific Instruments

The major portion of the science instruments were mounted on a science boom extending out some 2.5 m from the spacecraft [14]. At the end of the science boom was a steerable scan platform on which were mounted the imaging and spectroscopic remote sensing instruments. Mounted at various distances along the science boom were the plasma and charged particle detectors. The magnetometers were located along a separate boom extending 13 m on the side opposite the science boom. A third boom, extending down and away from the science instruments, held the spacecraft's radioisotope thermo-electric generators.
The following initial science instruments are listed:

- Imaging Science System (ISS): provide imagery along the trajectory, via narrow and wide-angle camera;
- Radio Science System (RSS): determine the physical properties of planets and satellites;
- Infrared Interferometer Spectrometer (IRIS): investigate on energy balance and atmospheric composition;
- Ultraviolet Spectrometer (UVS): measure radiation and atmospheric composition;

- Triaxial Fluxgate Magnetometer (MAG): investigate the magnetic field and solar wind stream;
- Plasma Spectrometer (PLS): measure particles as ions and electrons;
- Low Energy Charged Particle Instrument (LECP): measure particles distribution of ions and electrons;
- Cosmic Ray System (CRS): measure CRs properties;
- Planetary Radio Astronomy Investigation (PRA): investigate the radio emission from atmosphere of the planets;
- Photopolarimeter System (PPS): investigate on atmospheric scattering and composition of planets;
- Plasma Wave Subsystem (PWS): measure wave-particle interaction, through magnetosphere.

The instruments currently active on the probes are [14]:

Science Instruments active		
Science Instruments	Voyager 1	Voyager 2
ISS	OFF	OFF
RSS	OFF	OFF
IRIS	OFF	OFF
UVS	OFF	OFF
MAG	ON	ON
PLS	OFF	ON
LECP	ON	ON
CRS	ON	ON
PRA	OFF	OFF
PPS	OFF	OFF
PWS	ON	ON

Table 2.2: Voyager science equipment.

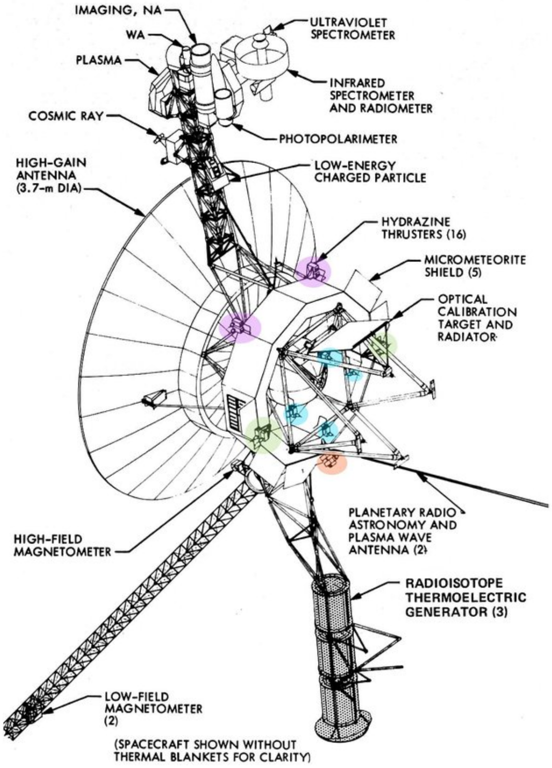

Figure 2.2: Voyager probes' science instruments.

2.2 Spacecraft status

Currently, both probes are flying through the nearest zone of Interstellar Medium, named Very Local Interstellar Medium (VLIM).
In November 2023 the mission status is:

Status data		
	Voyager 1	Voyager 2
Launch date (UTC)	Mon, 05/09/1977	Sat, 20/08/1977
Mission elapsed time (yy:mm:dd)	46:01:30	46:02:15
Distance from Earth (AU)	162.29	135.14
Distance from Sun (AU)	161.63	134.86
Direction from elliptic plane	35° North	45° South
Velocity with respect to the Sun (kps)	16.9995	15.3741
One-Way Light time (hh:mm:ss)	22:29:45	18:43:55

Table 2.3: Voyager 1 and Voyager 2 mission status.

2.2.1 Drift to the unknown

The Voyagers have enough electrical power and thruster fuel to be completely operative until at least 2025. By that time, Voyager 1 will be 22.1 billion kilometers from the Sun and Voyager 2 will be 18.4 billion kilometers. In thousand years, Voyager 1 will drift within 1.6 light-years whereas, Voyager 2 will pass 1.7 light-years from the star Ross 248. In more than 200.000 years, they will pass 4.3 light-years from Sirius (the brightest star in the sky). At the end, the probes will drift and wander the Milky Way, until they disruption.

2.3 The Golden Record

The Golden Record is a small metal plague in which Cornell University and NASA encoded multiple images (few more than 100), musical selections from several cultures and eras, sounds and greetings in more than 50 different languages and printed messages from President Carter and U.N. Secretary General Waldheim.
Indeed, they recorded where Earth is and how life developed. The goal is explain our homeland to possible clever extra-terrestrials.

Figure 2.3: The Voyagers' Golden Record.

2.4 Available Data

On OMNIWeb Plus by NASA, several types of deep-space data are placed: we can find raw data or preliminary plotting or distributions; resident at Goddard's Space Physics Data Facility.
Variables to select are:
POSITION IN HGI [30]:

- Heliocentric Distance (start of data interval), AU
- HelioGraphic Inertial (HGI) Latitude, deg
- HGI Longitude, deg

MAGNETIC FIELD IN RTN [30]:

- IMF BR in RTN(Radial-Tangential-Normal) coordinate system, nT
- IMF BT, nT (RTN)

- IMF BN, nT (RTN)
- IMF Magnitude (average of fine scale magnitudes), nT

PLASMA IN RTN [30]:

- Proton Flow Speed, km/sec
- Proton Flow Elevation Angle/Latitude, (RTN), deg
- Proton Flow Azimuth Angle/Longitude (RTN), deg
- Proton Density, n/cc
- Proton Temperature, K

Please note: Plasma instruments had failure in functioning from June 2018.
LECP PROTON FLUXES (1/(sec-cm**2-ster-MeV)) [15]:

- 0.57-1.78 MeV
- 3.40-17.6 MeV
- 22.0-31.0 Me

CRS(6-hr) PROTON FLUXES (1/(sec-cm**2-ster-MeV)) [30]:

- 3.000-4.600 MeV
- 4.600-6.200 MeV
- 6.200-7.700 MeV
- 7.700-12.800 MeV
- 12.800-17.900 MeV
- 17.900-30.000 MeV
- 30.000-48.000 MeV
- 48.000-56.000 MeV
- 74.471-83.661 MeV
- 132.834-154.911 MeV
- 154.911-174.866 MeV
- 174.866-187.713 MeV
- 187.713-220.475 MeV

- 220.475-270.050 MeV
- 270.050-346.034 MeV

Considering that Voyager 1 entered the Interstellar Medium in 2012, while Voyager 2 entered in 2018, to conduct the analysis data has been selected between 1st January 2016 to 31Th December 2020.
For our investigation, Magnetic field and plasma data have been chosen: position data were used to precisely relate particles data to their own distance from the Sun.

Chapter 3

Analysis 1 : Fluctuation Theory

3.1 Method: introduction

Space environment is deeply different to Earth's atmosphere: following Patched-conics approximation, gravitational field effects change through the Solar System, depending on the distance to the Sun; it implies the variation of the space particle composition is strictly related to Solar Wind, whereas atmospheric composition on each planet depend on its own mass and composition of the soil. One of Voyager mission goal was measuring how and how much magnetic field components, cosmic rays streams and particle streams (such as protons) evolve on the way: in general, it means to want to analyze the kinematic and dynamic behaviour of this complex system and to comprehend how it reacts to perturbations.

Especially, the kinematic approach was essential to identify where Voyager probes crossed the Termination Shock, indeed strong shocks produced high energy dissipation, due to solar and stellar wind collision, and where they entered the Interstellar Medium.
At long timescales, the variability of these microscopic patterns can be associated to nonequilibrium fluctuation phenomena: at the edge of the Solar System, solar gravitational field has a weak effect so, magnetic interaction on particles is weak too. Therefore, magnetic field components showed an extremely low magnitude.

The theory of nonequilibrium fluctuations describes small systems, whereby constituting elements interact on scales comparable with those of the overall system resulting in observable fluctuations. In this manner, the investigation on outer heliosphere phenomena and interstellar medium phenomena is crucial to understand what is the relation between magnetic field components, which were found to constantly decrease and oscillate and the gravitational field effects, which should be approximately zero. Every crossing by termination layers implies a magnitude gap of magnetic field, while protons parameters constantly increase (up to malfunctioning in 2018): the question arises if the magnetic and gravitational field completely disappears somewhere or if gravitational field of star light years from Solar System affects Outer Heliosphere and VLIM.

A statistical point of view helps to evaluate local trends: probability distributions identify the evolution of non-linear system, by analyzing the mode and the lowest and the highest value of a dataset. Subsequently PDFs are scaled to due to overall conditions.

Distribution index are used to extrapolate future scenarios, in order to calculate critical values, that state when specific limits are reached.

In 2012 previous studies applied the energy conservation law to describe which the measured value has to be to state the Termination Shock crossing. If initial total pressure value is circa 25.855 K/cc whereas final one is 5.565 k/cc, that implies that gravitational field pressure required is 8 μG, while measured is only 3 μG. It indicated that Heliosheat zone was not completely crossed over [10].

Guided by the theory of nonequilibrium fluctuations [7], in this thesis we consider magnetic field components and parameters of protons data, mediated on different time scale and data anomaly to the mediated data. We will see that the bigger the time range is, the more narrow the probability distribution is, because the majority of values oscillates around a well-defined value. Ideally, if time range could go to infinite, the values would start to fluctuate asymptotically around the mode.

In conclusion, despite the relative position to ecliptic plane, both probes have collected similar data, even if at different distance to the Sun and time.

Below, the fundamental steps for implementing the above-mentioned method are discussed, and for a more comprehensive understanding, references to the theory of statistical analysis are included.

3.1.1 Probability Function and PDF

Probability distribution [11] is a mathematical model that links the value of a variable of interest to the possibility to be observed; considering a set of random variables in a space of events, it is used to model the behaviour in relation to its target population.

If variable has a discrete distribution, probability function p(x) is the mathematical law used to describe the events, otherwise probability density function f(x) is the one used to describe continuous distributions.

Any probability distribution P(x) is defined probability function if[28]:

- for any $x_i : 0 \leq P(x_i) \leq 1$
- $\sum_{i=1}^{N} P(x_i) = 1$: Closure Property

It is also useful to define the infinitesimal probability that X assumes a value between x and x+dx: dp(x) = f(x) dx. Graphically, the probability that X will assume a particular value within a range is only the area enclosed below the probability density in that range. Then, PDF is defined as:

- $\int f(x)dx =$ P(x) = 1 : Closure Property
- $P(x_1 \leq X \leq x_2) = \int_{x_1n}^{x_2} f(x)dx$

In our analysis, all measures are discrete distributions, so we start analyse probability function, in order to obtain PDFs, through histogram elaborations.

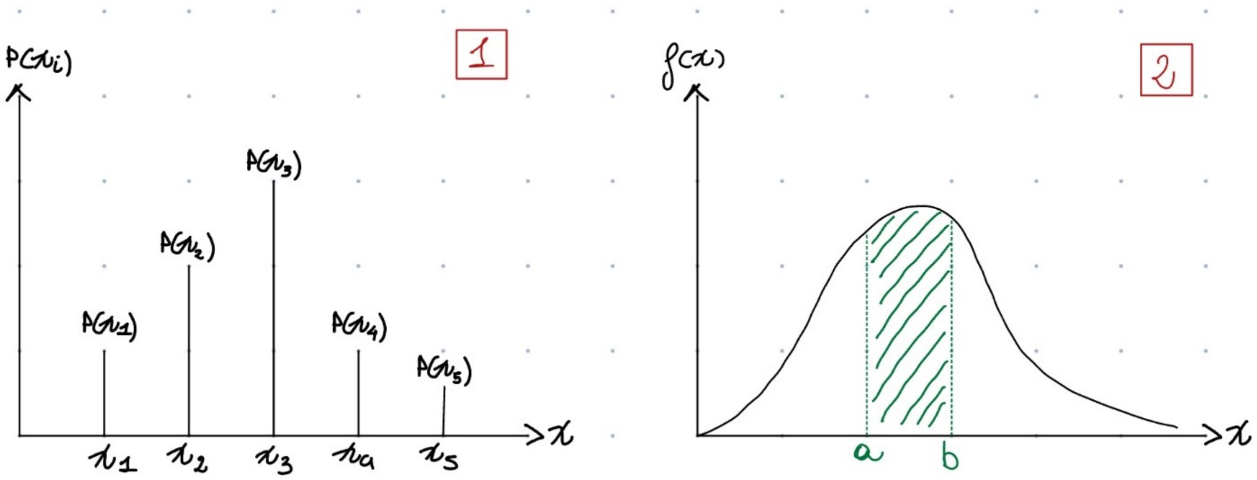

Figure 3.1: Probability distribution: discrete case (1); continuous case (2).

3.1.2 Histograms

An histogram is a powerful mathematical tool, used in statistical analysis, that helps to clarify the redundancy of a measure of interest from a dataset and to show probability distributions. The complete sample of data is given as input, whereas the output is a bar graph, within x-axis indicates all the possible values and y-axis indicates how many measures has a defined value.

Basically, the highest bar is related to the most redundant value, otherwise the lowest bar shows the less frequent value. The highness of the bar indicates the probability that the variable of interest occurs, in a defined range.

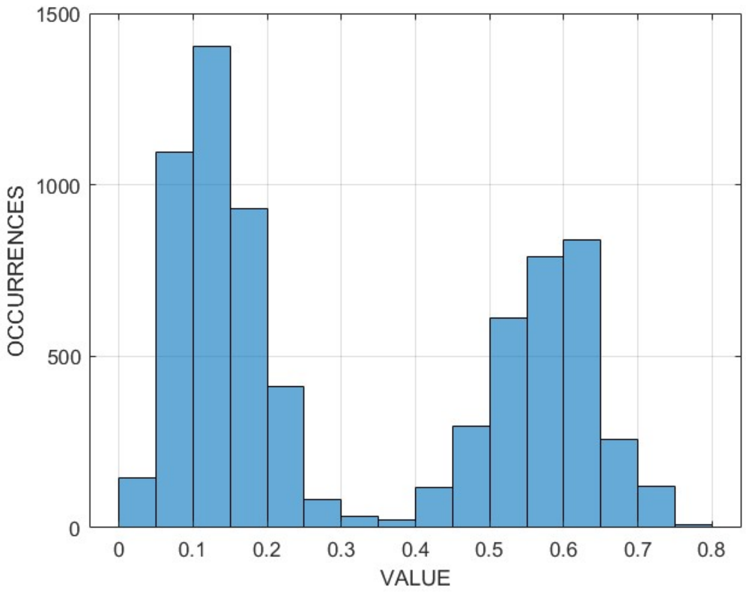

Figure 3.2: Generic histogram.

Therefore, a method to properly compare histograms and PDFs, is normalize according to central bin probability, that counts Np(x)Δx events: to achieve a correct normalization, PDF p(x) must be multiplied by a factor of NΔx.

Binning

On this thesis, solution algorithms are provided by MATLab software: so, bin edge setting was fundamental to histogram function to work properly. Consequently on x-axis, not raw sample value, but mean of bin width is displayed.

3.1.3 Asymmetric Laplace distribution

Effective is the comparison between PDFs, created from histograms, and asymmetric double exponential distributions (or asymmetric Laplace distributions), with probability density function (PDF):

$$f(x; m, \beta_1, \beta_2) = \begin{cases} \beta_0 e^{\frac{-(x-m)}{\beta_1}} & x > m \\ \beta_0 e^{\frac{(x-m)}{\beta_2}} & x \leq m \end{cases} \tag{3.1}$$

where the random variable x may refer to either averaged data or anomaly averaged data, m is the mode, and β_1 and β_2 are the exponents for the right and left tails. The multiplier constant is:

$$\beta_0 = \frac{1}{\beta_1 + \beta_2} \tag{3.2}$$

The difference of the two exponents describes the symmetry of the distribution and hence is referred to as the symmetry index:

$$\Delta\beta = \beta_1 - \beta_2 \tag{3.3}$$

which is also closely related to the skewness of the distribution. The exponents are estimated by linearly fitting the logarithm of each tail of the weighted histogram; then mean and variance are evaluated as the weighted statistics.

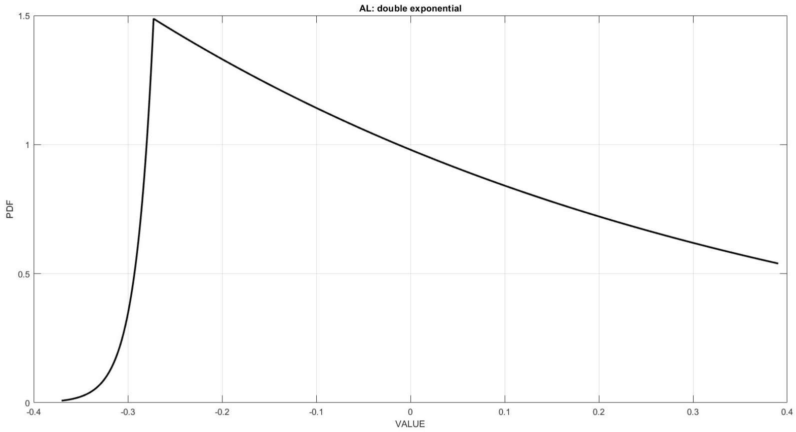

Figure 3.3: Asymmetric Laplace distribution: example

However in this thesis, this distribution type is derived by weighted histogram slopes, hence PDF equations are quite different:

$$f(x; m, sR, sL) = \begin{cases} N \cdot e^{-sR\cdot(x-m)} & x > m \\ N \cdot e^{sL\cdot(x-m)} & x \leq m \end{cases} \tag{3.4}$$

where x could be any variable, m is the mode, sL and sR are respectively left and right slope of the weighted histogram. Then,

$$N = \frac{sR \cdot sL}{(sR + sL)} \tag{3.5}$$

Symmetry index will be calculate by discrete formulations.

3.1.4 Distribution index

For our study, most interesting distribution index are moments (and cumulants), skewness and kurtosis. Each index describes different distribution properties, but are all based on central moments.

Moments and Cumulants

According to the definition of Characteristic Function $\phi(t)$, which is the Fourier function of the probability function, central moments are coefficients of the Taylor's expansion of $\phi(t)$, whereas cumulants are coefficients of the Taylor's expansion of $\log(\phi(t))$. The generating function for the moments is [**moment**]:

$$M(x) = E(e^{xx}) = \int_{-\inf}^{\inf} e^{xx} f(x) dx \tag{3.6}$$

While any coefficient has the following form:

$$\mu_n = \frac{1}{N} \cdot \sum_{i=2..n}^{n} (x_i - \mu_1)^n \tag{3.7}$$

where, μ_1 is the mean, μ_2 is the variance and $\sqrt{\mu_2}$ is the standard deviation.
The generating function for the cumulants is [22]:

$$K(x) = \log(M(x)) = \sum_R K_R \cdot \frac{X^R}{r!} \tag{3.8}$$

Once we consider 5 order Taylor expansion, cumulants and central moments are linked as below:

$$\mu_1 = K_1 \tag{3.9}$$

$$\mu_2 = K_2 \tag{3.10}$$

$$\mu_3 = K_3 \tag{3.11}$$

$$\mu_4 = 3 \cdot K_2^2 + K_4 \tag{3.12}$$

$$\mu_5 = 10 \cdot K_2 \cdot K_3 + K_5 \tag{3.13}$$

These are the parameters of interest.

Skewness

Skewness indicates the distribution symmetry (or, asymmetry). If skewness index is zero, the symmetry of the distribution is confirmed. Otherwise there is just asymmetry: right distributions get a positive skewness value while, left ones get a negative value.

Skewness index depends on both central moments and cumulants [23]:

$$\gamma_1 = \sqrt{\beta_1} = \frac{\mu_3}{\mu_2^{\frac{3}{2}}} \tag{3.14}$$

$$g_1 = \frac{K_3}{K_2^{\frac{3}{2}}} \tag{3.15}$$

General formulation is therefore:

$$Sw = \frac{E(X - \mu_1)^3}{\sigma^3} \tag{3.16}$$

where E(...) means scalar mean and σ is deviation.

Kurtosis

Kurtosis index quantifies how many variables sit in a particular side of the distribution: tailedness is how often outliers occur. Narrow and high PDFs are defined Leptokurtic Distributions, Normal PDFs are defined Mesokurtic Distributions and low and wide PDFs are defined Platykurtic Distributions.

Kurtosis formula is central moments based:

$$\beta_2 = \frac{\mu_4}{\mu_2^2} = \frac{E(X - \mu_1)^4}{(E(X - \mu_1)^2)^2} \tag{3.17}$$

3.1.5 Scaling of variables

Then, to make explicit the link between random variables and overall system, we rescaled both sides of the distributions by the corresponding exponents (in our analysis, right and left slopes) to find the scaling factor. The rescaled variables become:

$$\overline{X} = \begin{cases} sR \cdot (x - m), \ x > m \\ sL \cdot (x - m), \ x \leq m \end{cases} \tag{3.18}$$

After this scaling, once histogram trend and new x-axis variables are plotted, we can obtain scaled PDF, which has a unit exponent for both tails. In addiction, tails collapsed into one group of curves on each side.

Subsequently, to quantify the symmetry implied by the fluctuation theorem, we consider the ratio of the logarithm of scaled PDFs, away from the mode in a distance of α

$$\log\left[\frac{f(\alpha + m)}{f(-\alpha + m)}\right] = \frac{\alpha\Delta\beta}{\beta_1\beta_2} = \alpha(\frac{1}{sL} - \frac{1}{sR})sL \cdot sR \tag{3.19}$$

which is proportional to the asymmetry index.

The method [17] concerned the interpolation of the re-scaled PDFs in (α + m) and ($-\alpha$+ m) query points; moreover, in the current elaboration, we reported both PDF reanalysis: histogram one and Laplace's asymmetric one.

3.1.6 Extrapolation of data

Starting from magnetic field data, measured after entering the Interstellar Medium, to project future temperature fluctuation from historical records, we extrapolated the mean, variance, and symmetry index of the random variables set with smoothing window $\tau = 45$ hours for Voyager 2, and $\tau = 35$ hours for Voyager 1.
To simplify the extrapolation, a linear function was first chosen to fit the curve but a cubic function was used to capture the nonlinear behaviors of the variance. This by no means covers all possible extrapolations, but provides a first glimpse into future conditions. With the projected mean, variance, and asymmetry index, we can obtain all parameters for the asymmetric double exponential distribution.

Need to focus on shape parameter λ, which is related to variance (that quantifies dispersion), and on simmetry parameter k, related to skewness,

$$variance = \frac{1+k^4}{\lambda^2+k^2} \tag{3.20}$$

$$skewness = \frac{2\cdot(1-k^6)}{(k^4+1)^{\frac{3}{2}}} \tag{3.21}$$

and provide distributions of future scenarios, up to 2029.

Due to malfunctioning, we only own parameter protons data up to 2019, so future projection are obtained starting from complete data before 2019, collected by Voyager 2, however following the same method.

3.2 Elaborations: guide

Two elaborations will be provided:

- ELABORATION 1: where magnetic field components data and proton parameters are evaluated and mediated by implementing the aforementioned method on several time window τ. For both probes, any components will be studied, especially scalar magnetic field magnitude and density of protons, in order to extrapolate data to analyse future scenarios.

  Magnetic field components are in RTN (Radial-Tangential-Normal) unit:

  - BR : Magnetic field radial component;
  - BT : Magnetic field tangential component;
  - BN : Magnetic field normal component;
  - BS : Magnetic field scalar magnitude;

  For greater clarity, the reference system is shown below:

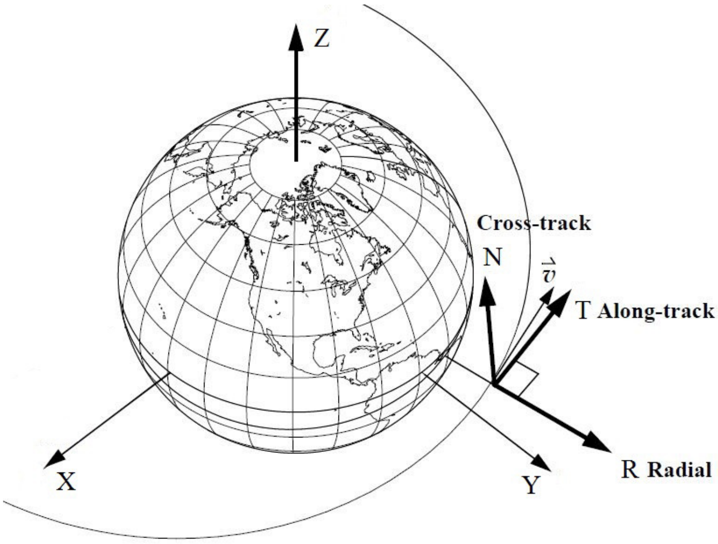

Figure 3.4: RTN system of reference.

While, the following are proton parameters:

  - ρ = density;
  - T = temperature;
  - S = speed;

- ELABORATION 2: where mediated anomaly of magnetic field components and proton parameters is evaluated. In addiction: just scalar magnitude and density is respectively considered, because they are the most relevant variables.

Both are applied on a time range of 5 years (from January, 1st 2016 to December, 31th 2020), where it's possible to observe different behaviours.

In conclusion, to provide extrapolation, just post-critical measurement are kept: we will see more deeply during the analysis.

3.3 Elaboration 1: Voyager 1

Once Voyager 1 completely crossed the Heliosheat in 2012, data collected were entirely about Interstellar Medium environment [14]; magnetometers measured several strong signal jumps with respect to the local trend: changing conditions should identifies Bow shock layer, where strong shocks occur due to sizable and high density hydrogen wall.

3.3.1 Magnetic field components

At the beginning, the link between relative position to the Sun of the probe and time is displayed to show the probe motion and path gained: remember that its speed is around 3.5 AU per year.

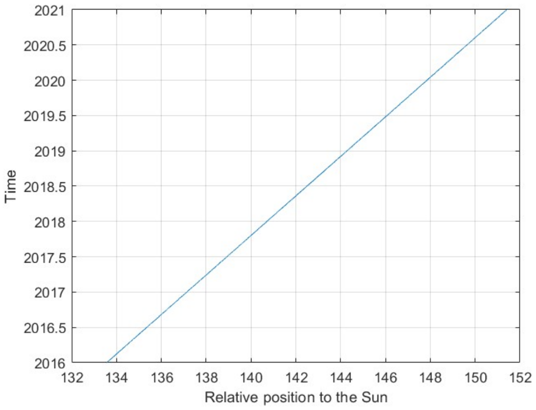

Figure 3.5: Time and position relation: Voyager 1 probe

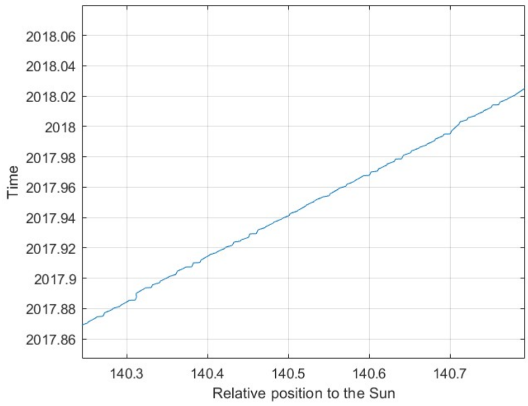

Figure 3.6: Time and position relation: trajectory shape.

Then, magnetic field behaviour and evolution are analysed.

Raw data

Raw data are measured data, without any elaboration: they are therefore contaminated by full scale data, which have to be eliminated to understand the correct trend of data.

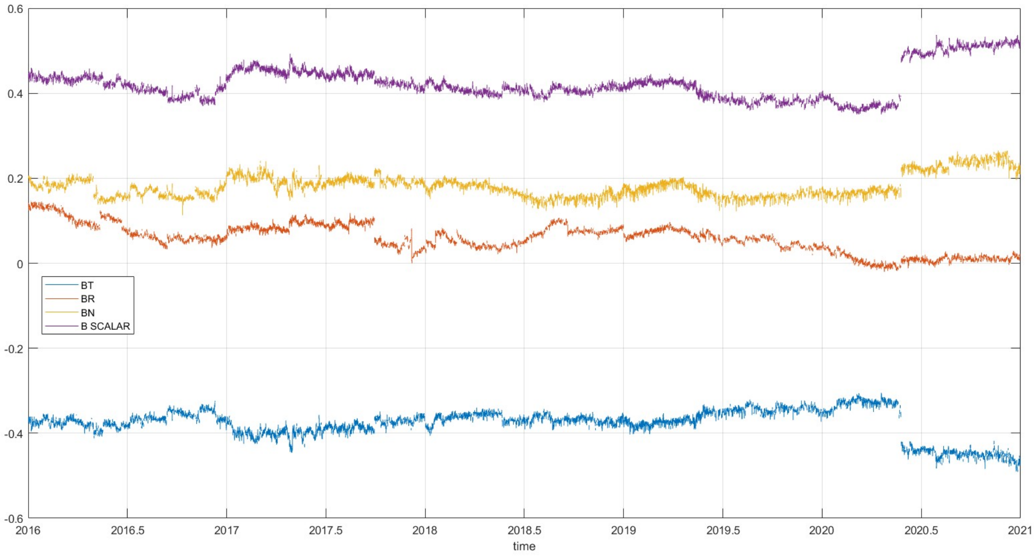

Figure 3.7: Trends without full scale data.

As shown all values sit in a range of [-0.6 +0.6], where magnitude gets the highest amplitude, meanwhile, the only negative component is tangential one, according to sensor position on the spacecraft. Every function shows jumps: normal and radial components remain quite smooth, but in June 2020 the other ones had a great jump, which could state the entrance in Bow shock region.

Probability function

After data were filtered, and averaged data have been evaluated on six different time windows $\tau = [2\ 4\ 8\ 15\ 35\ 80]$, histograms have been normalized and trends have been extracted to obtain probability density functions.

All variables involved a varying behaviour:

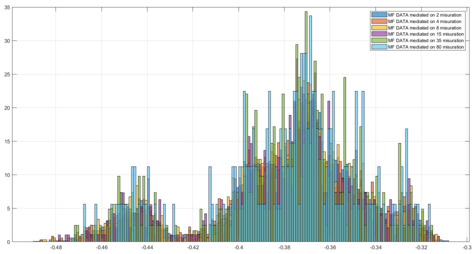

Figure 3.8: Histogram of magnetic field TANGENTIAL component.

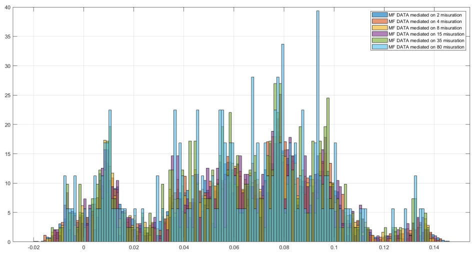

Figure 3.9: Histogram of magnetic field RADIAL component.

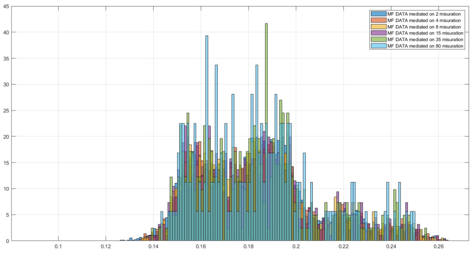

Figure 3.10: Histogram of magnetic field NORMAL component.

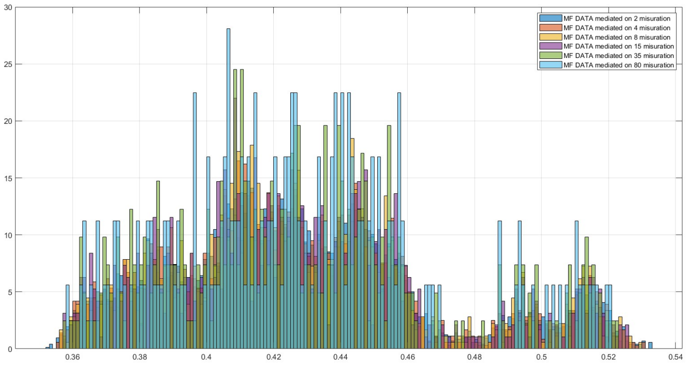

Figure 3.11: Histogram of magnetic field MAGNITUDE.

All components have multiple peaks, but to make the comprehension easier, just the biggest one will be considered to scaling and extrapolate indexes. Moreover tangential component presents thicker shape, otherwise radial component and magnitude seems to have more spreaded data.

Then, once histogram values are extracted and normalized, x-axis values (mediated data) are scaled of average mean to obtain probability density function.
The following are listed: tangential, radial and normal component and magnitude.

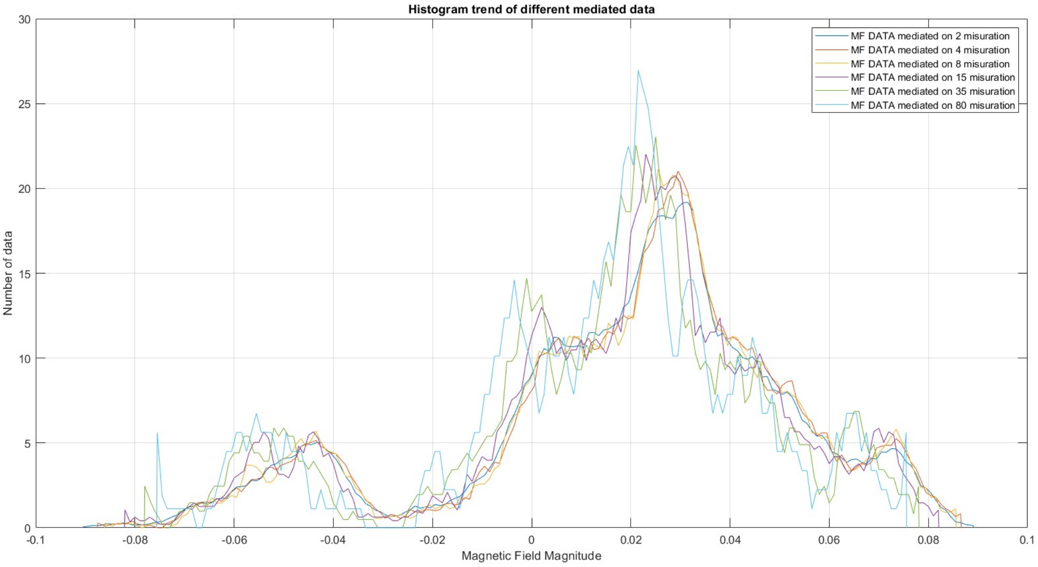

Figure 3.12: PDF trend of magnetic field TANGENTIAL component.

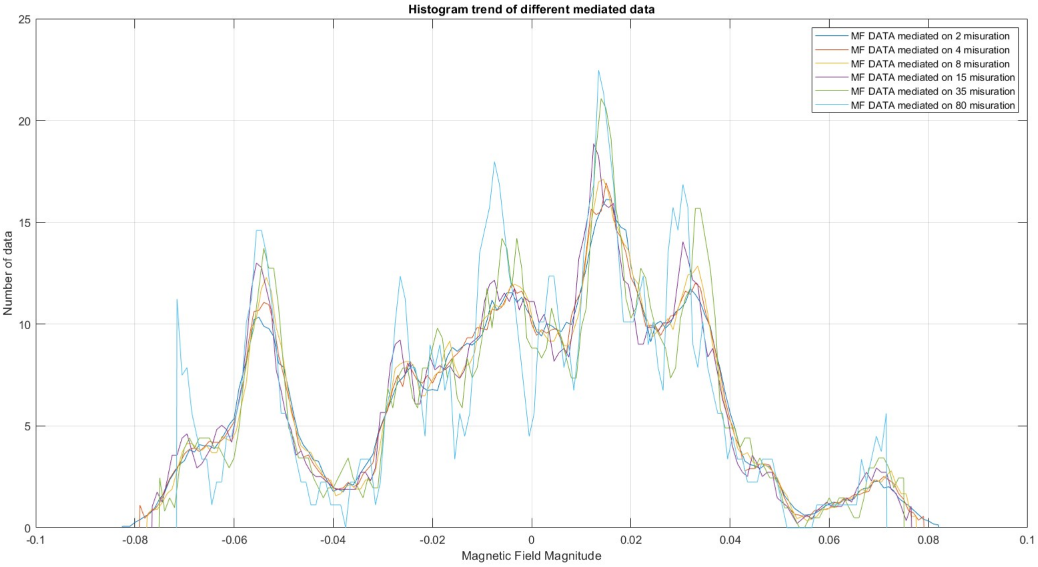

Figure 3.13: PDF trend of magnetic field RADIAL component.

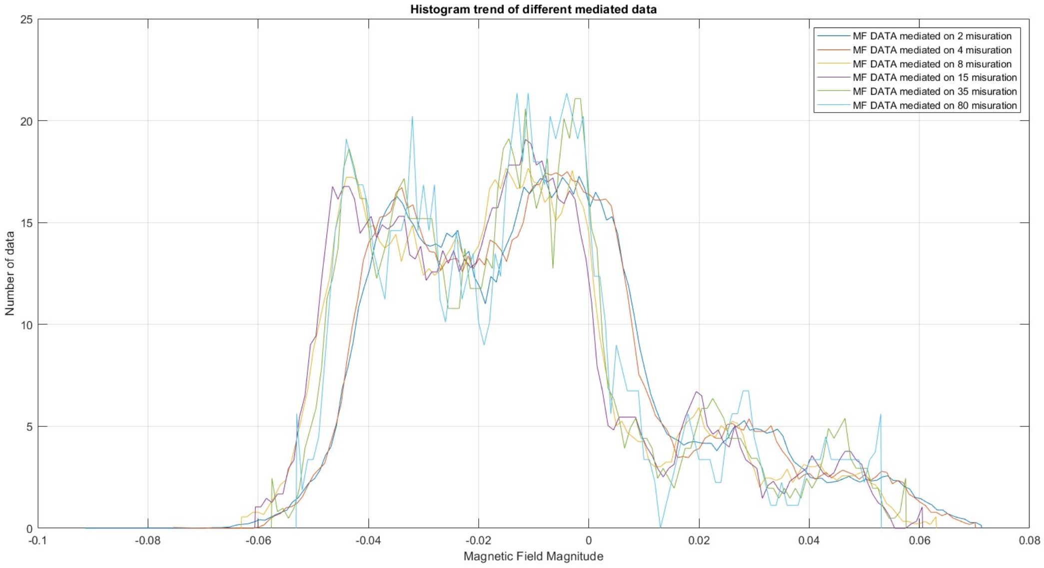

Figure 3.14: PDF trend of magnetic field NORMAL component.

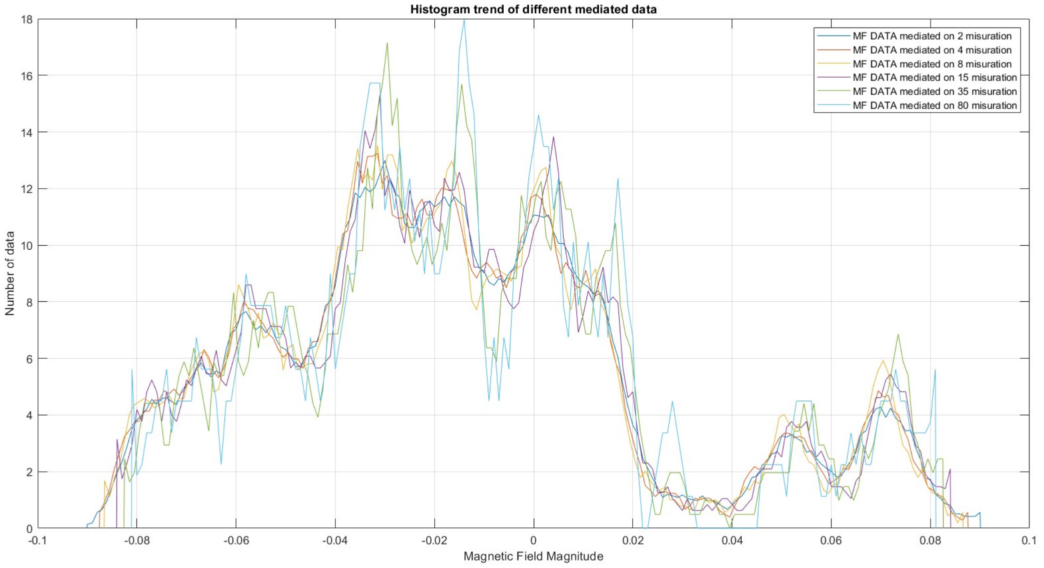

Figure 3.15: PDF trend of magnetic field MAGNITUDE.

The wider the time window become (number of measures increases in a range), the higher and more narrow the curve become, because more and more measures accumulate in mode boundary position.

We need to linearize both side of each PDF to implement Asymmetric Laplace distribution (Asymmetric PDF), so right and left slopes are obtained by first order polynomial interpolation; by this approximation, trends have same shape, so we could give a clearer look on component behaviours, on different τ. Moreover, ALDs show (a)symmetry trends: despite same component, different τ can carry out opposite mode position, in respect with averaged mean.

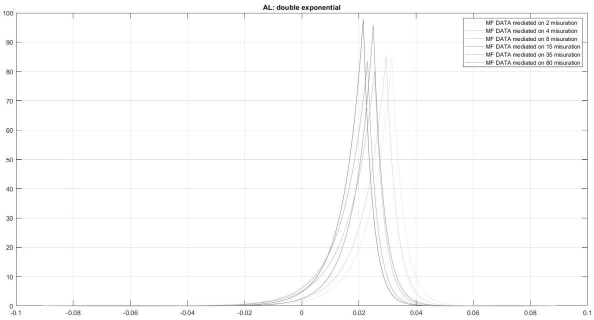

Figure 3.16: BT: Asymmetric Laplace distribution

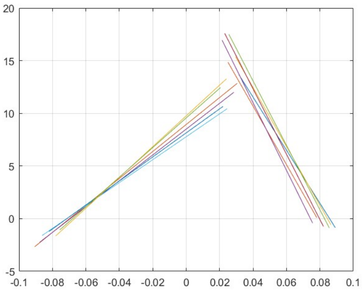

Figure 3.17: BT: slope linerization

As expected, lighter ALDs are related to smaller τ: they are lower and wider, otherwise, darker ones are related to amplier averaged data range. The shapes are confirmed by linearization that states that curves make a anti-clockwise arise, starting from first one at $\tau = 2$, to the last one at $\tau = 80$.

Other components make evident same behaviours.

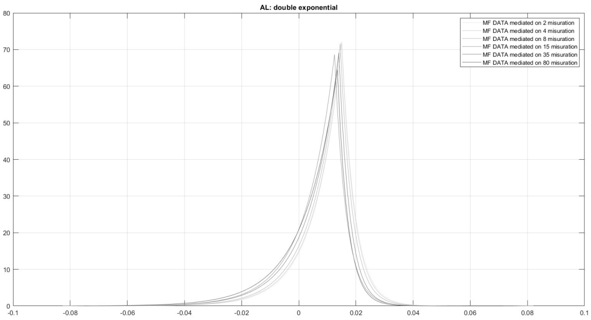

Figure 3.18: BR: Asymmetric Laplace distribution

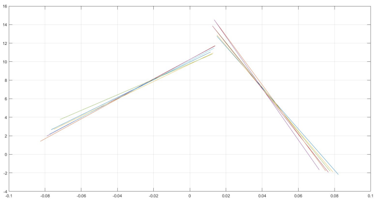

Figure 3.19: BR: slope linerization

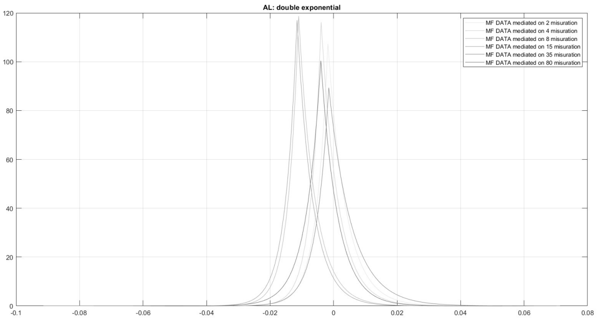

Figure 3.20: BN: Asymmetric Laplace distribution

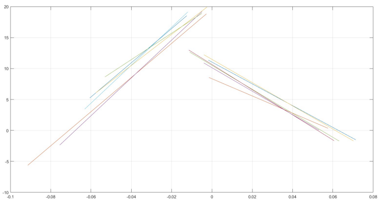

Figure 3.21: BN: slope linerization

Normal component shows a slight dual asymmetrical behaviour: $\tau = 15$ was found to be a critical division choice, because initial and final τ values have same asymmetry trends, whereas this case developed negative asymmetry distribution.

These must be a notable value in reason of the measure jumps: it highlight a rare trend that occurs for a few parameters, for example $\tau = 44$.

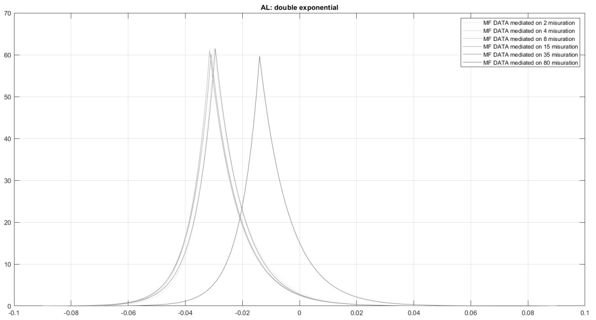

Figure 3.22: BS: Asymmetric Laplace distribution

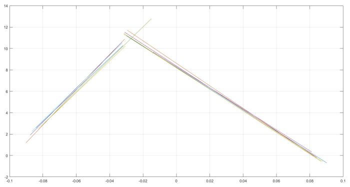

Figure 3.23: BS: slope linerization

The most remarkable trend is magnitude one: all curves have same asymmetry, but peaks don't show with increasing evolution, but the latter mode is substantially shifted to negative values.

Scaling

Next steps require probability function to be scaled with against raw mean μ, with the purpose of comparing all trend to the overall system. As we anticipated, scaling is pursued by multiplying by a factor, such as right and left slopes.
We'll demonstrate how each side of PDFs will collapse on a well-defined bundle of strings. Linear graphs display histogram PDF scaling, besides logarithmic ones are more precise.

Please note that, sometimes tails scaling doesn't properly work.
LINEAR SCALING:

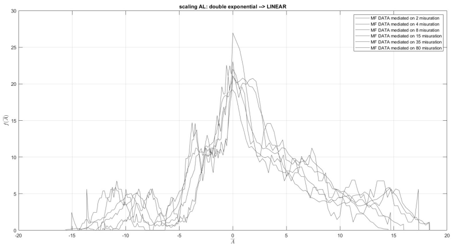

Figure 3.24: BT: Linear scaled trends

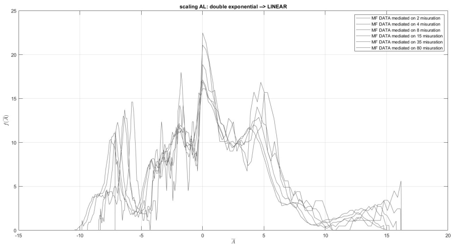

Figure 3.25: BR: Linear scaled trends

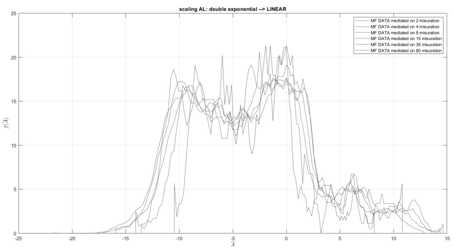

Figure 3.26: BN: Linear scaled trends

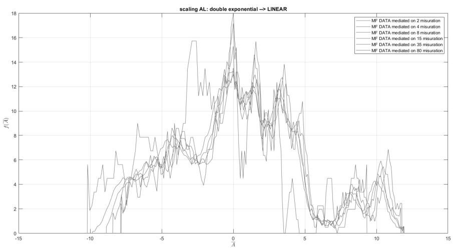

Figure 3.27: BS: Linear scaled trends

LOGARITHMIC SCALING

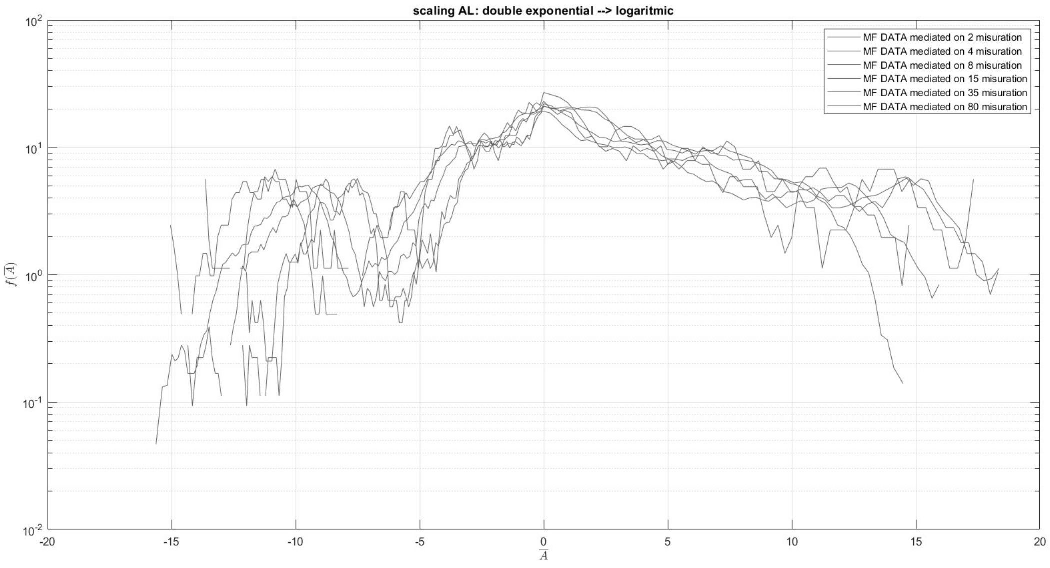

Figure 3.28: TANGENTIAL magnetic field component: LOGARITHMIC scaled trends.

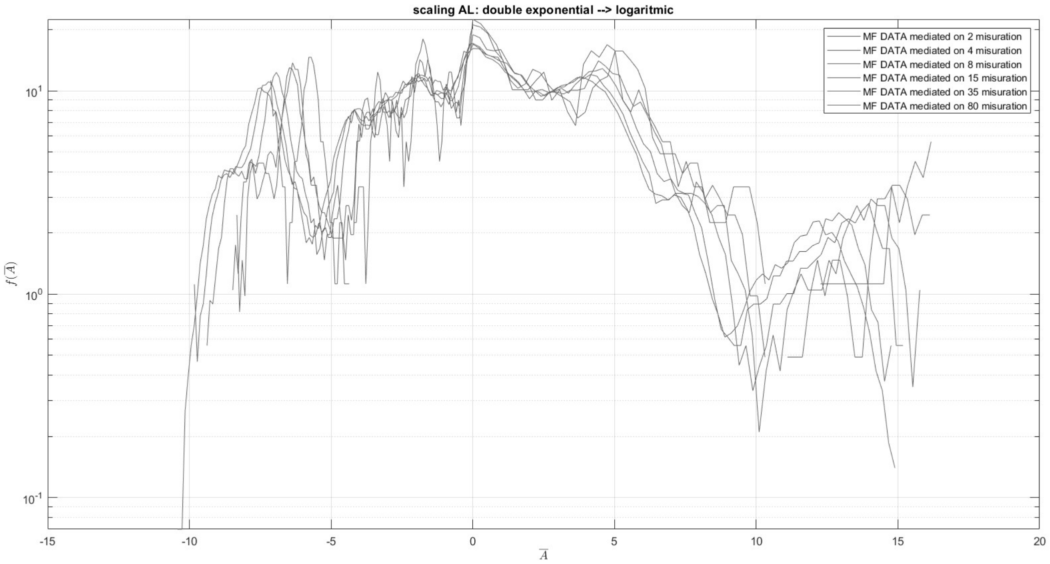

Figure 3.29: RADIAL magnetic field component: LOGARITHMIC scaled trends.

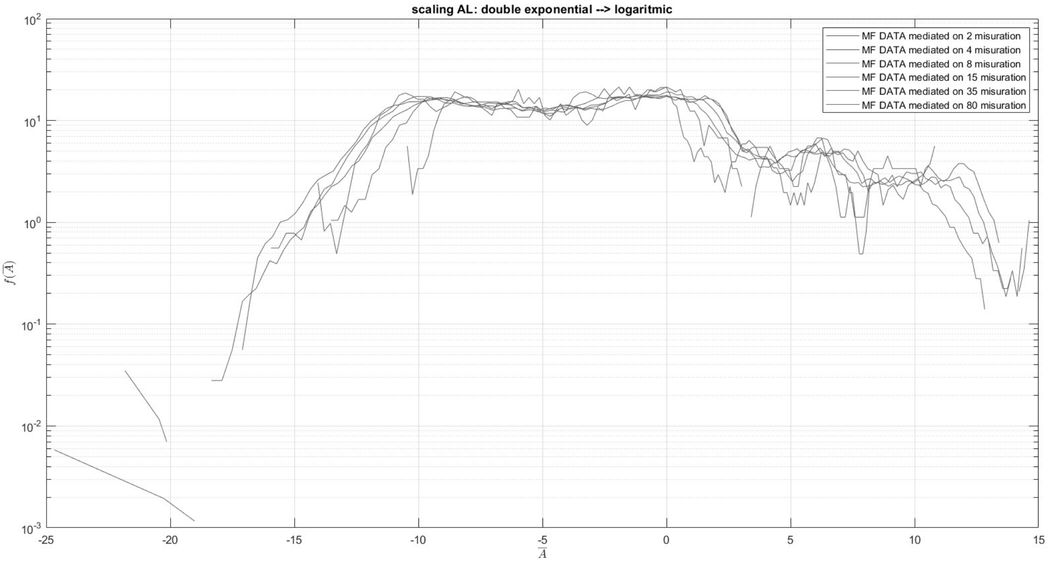

Figure 3.30: NORMAL magnetic field component: LOGARITHMIC scaled trends.

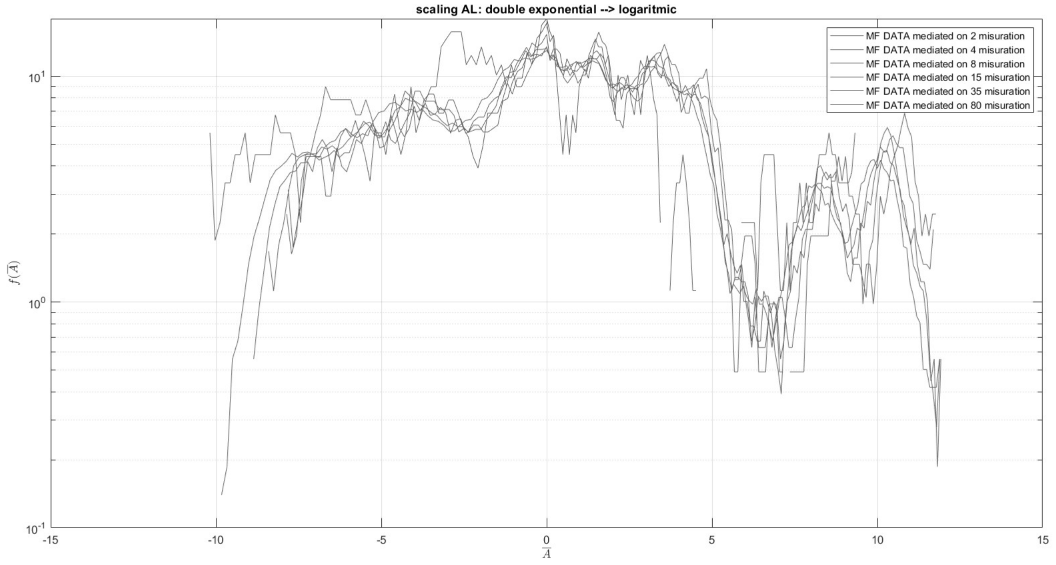

Figure 3.31: MAGNITUDE of magnetic field: LOGARITHMIC scaled trends.

Symmetry factor

Then, to define simmetry factor due to scaled functions, PDFs are interpolated in query points, in a distance α from the mode. ALDs reveal a quite linear trend, given by bundle of string collapsed on one line; otherwise, histogram PDFs show a constant and continuous behaviour, which begins to oscillate with a broken and irregular pattern.

For every components, on any τ, factors are compared, especially tangential component ALD factor is showed, without limitation:

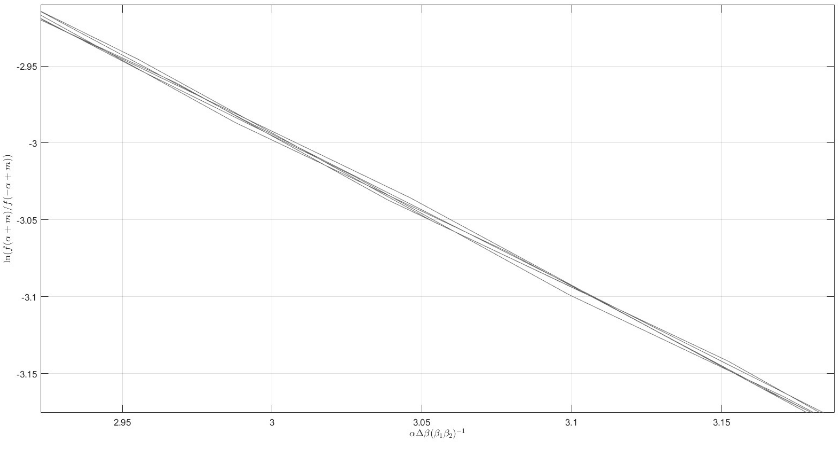

Figure 3.32: BT: ALD scaling factor –> bundle collapse example.

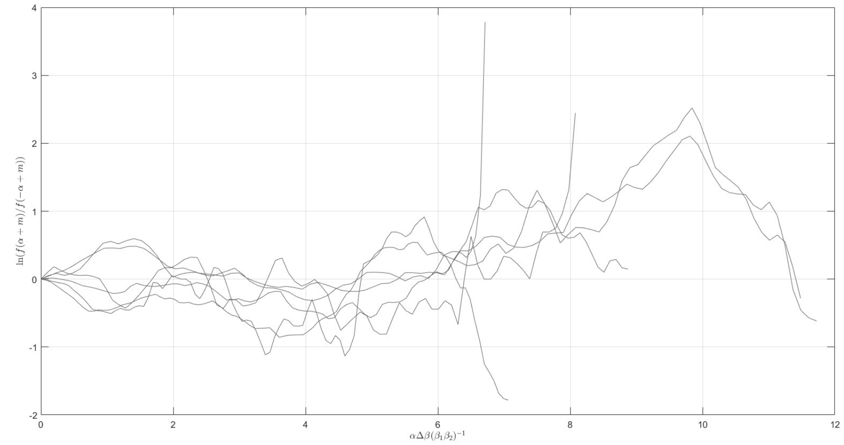

Figure 3.33: BT: histogram PDF scaling factor.

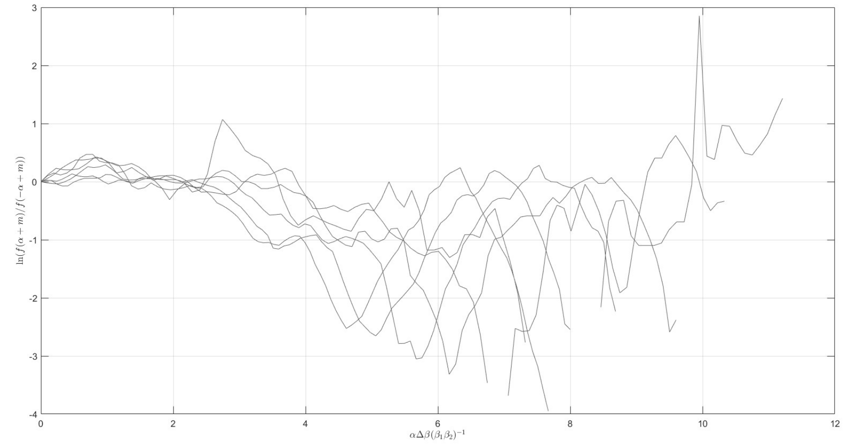

Figure 3.34: BR: histogram PDF scaling factor.

The symmetry factor, concerning the radial component, exhibits an initial nearly linear trend, but subsequently continues oscillating sinusoidally. For each τ, the trend is approximately similar but shifted, based on the mode value in the specific case under consideration.

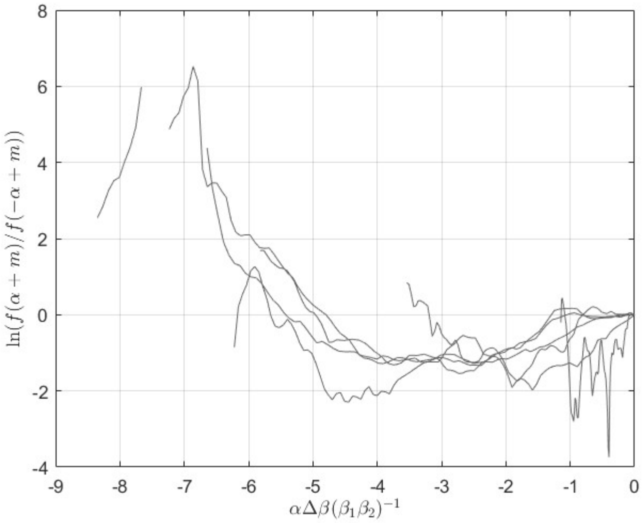

Figure 3.35: BN: histogram PDF scaling factor.

The symmetry factor, concerning the normal component, starts with a quadratic trend, to continues quite linearly. Wider τ generates amplest curve.

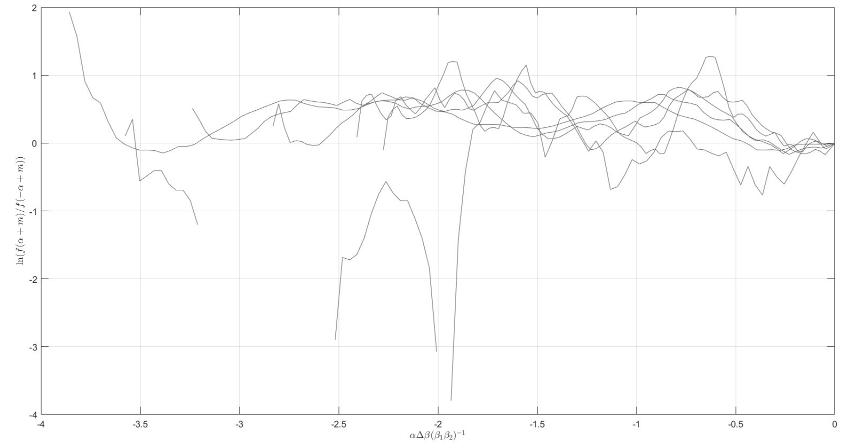

Figure 3.36: BS: histogram PDF scaling factor.

The scalar behaviour summarizes all components: we can observe oscillations, but trend is linear, in reason of PDFs of reference (histogram ones, despite of ALDs ones).

Distribution indexes

We calculated distribution indexes, following two distinct ways: non only related to mediated data by the factor τ, in order to see trend of the index according to the variation of τ, but also by choosing an average τ and valuating them on every interval obtained.

In this section indexes are evaluated by the second method: it's interesting to compare the same index (et. Variance, Skewness and Kurtosis) for all components.

- Variance: it quantifies the dispersion of the distribution.

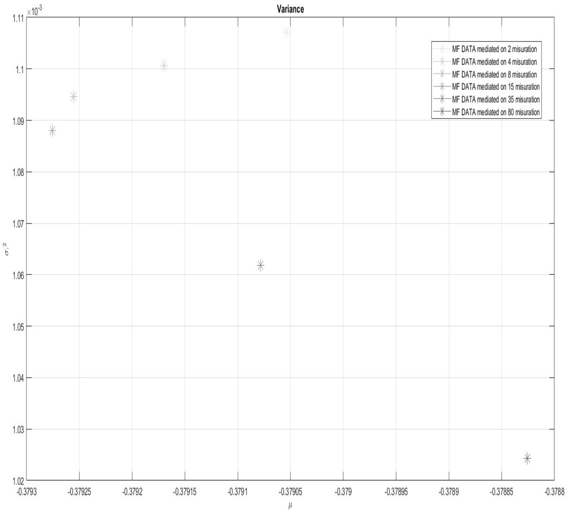

Figure 3.37: BT: VARIANCE σ^2

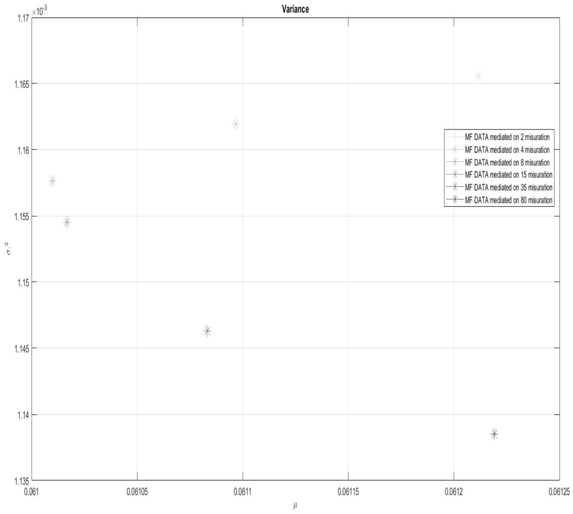

Figure 3.38: BR: VARIANCE σ^2

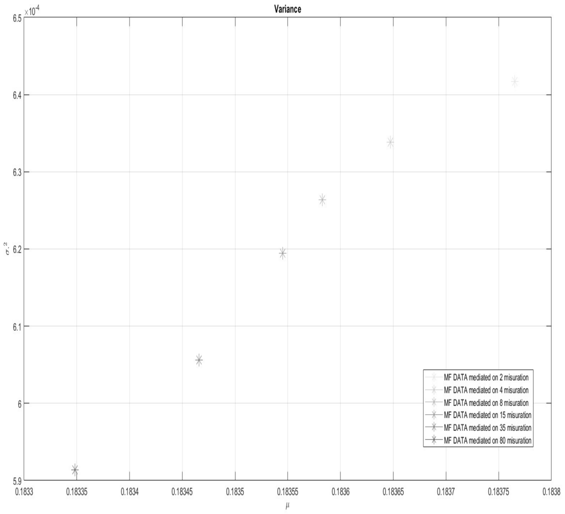

Figure 3.39: BN: VARIANCE σ^2

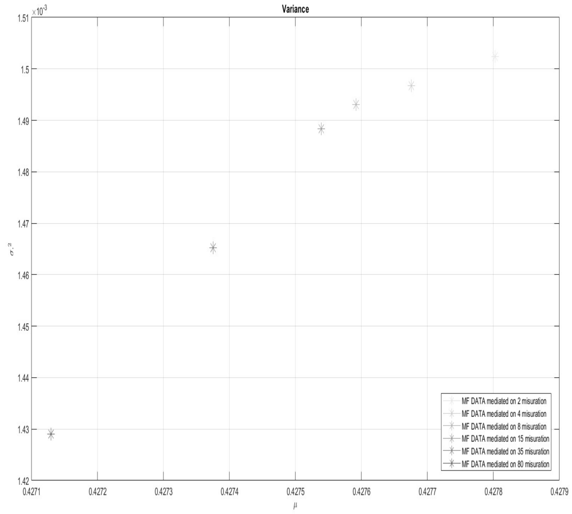

Figure 3.40: BS: VARIANCE σ^2

Darker index is related to $\tau = 80$, while lighter one to $\tau = 2$.

On x-axis, mediated measurements are displayed, on y-axis, there is the corresponding idex value. Anywhere the dispersion is greater for spread measure, in other words, for $\tau = 2$, otherwise for $\tau = 80$. However, it's evident that tangential and radial components exhibit same trends: average measure is bigger for extreme τ values, whereas a minimum is reached for a mean value. Alternatively, normal component and magnitude have decreasing trends: higher variance is linked to an higher average mean and $\tau = 2$, as lower variance is linked to lower average mean and $\tau = 80$.

- Skewness: it quantifies, by central moments ratio, how asymmetry is strong.

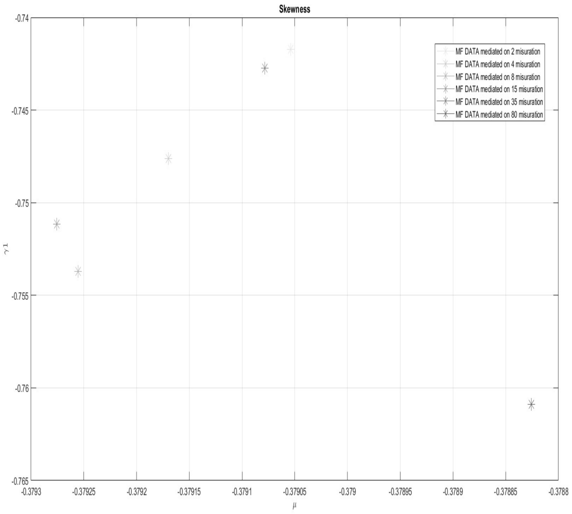

Figure 3.41: BT: SKEWNESS γ_1

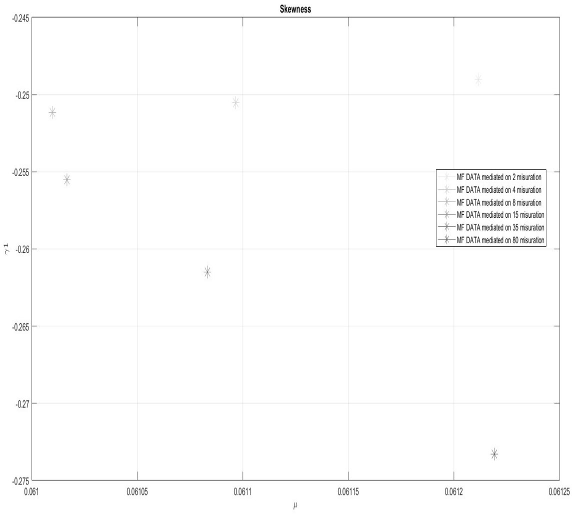

Figure 3.42: BR: SKEWNESS γ_1

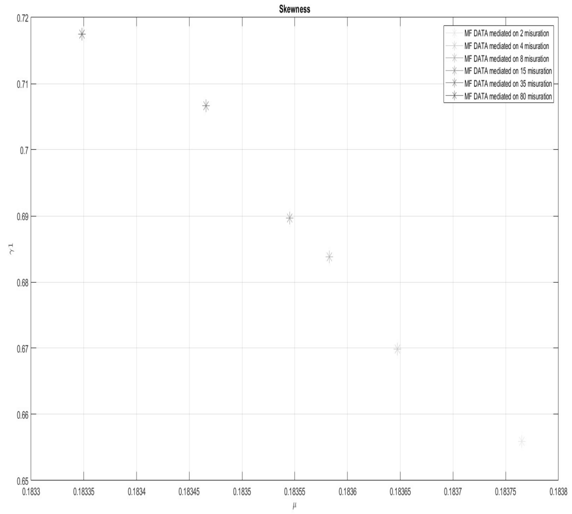

Figure 3.43: BN: SKEWNESS γ_1

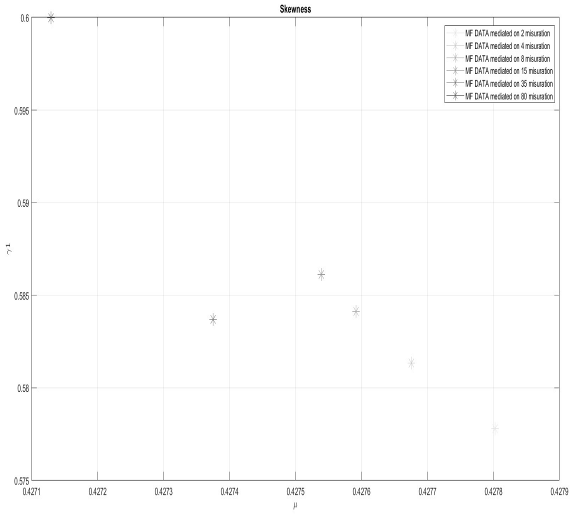

Figure 3.44: BS: SKEWNESS γ_1

Skewness trends are almost the same for tangential and radial components, but in normal component and magnitude case, trends are completely opposite to variance ones. We can observe an increasing trend: the more measurements concentrate around the mode value (in the case of a larger tau), the more the dispersion decreases, and the tendency towards symmetry is more pronounced.

Extremely significant and, of course, deducible is that the magnitude (the "component" summarizing the behavior of the RTN components) exhibits this particular trend.

- Kurtosis: it quantifies how many measurements sit in a determinate tail.

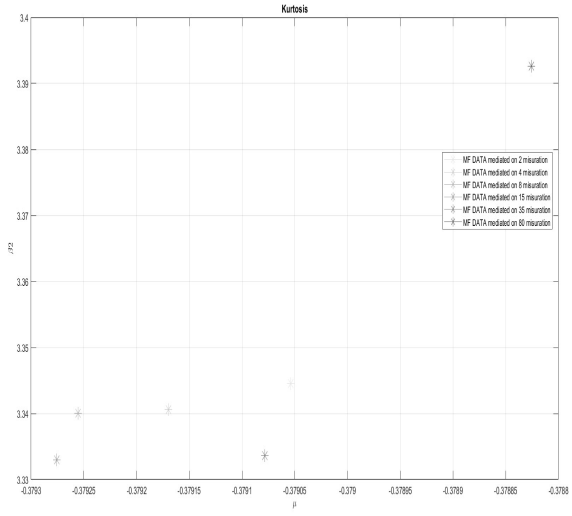

Figure 3.45: BT: KURTOSIS β_2

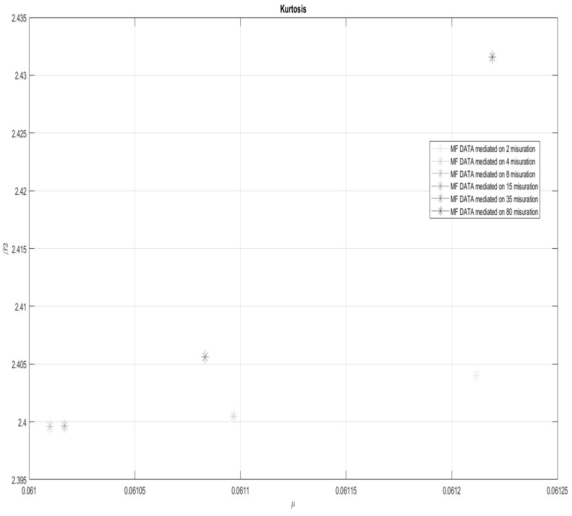

Figure 3.46: BR: KURTOSIS β_2

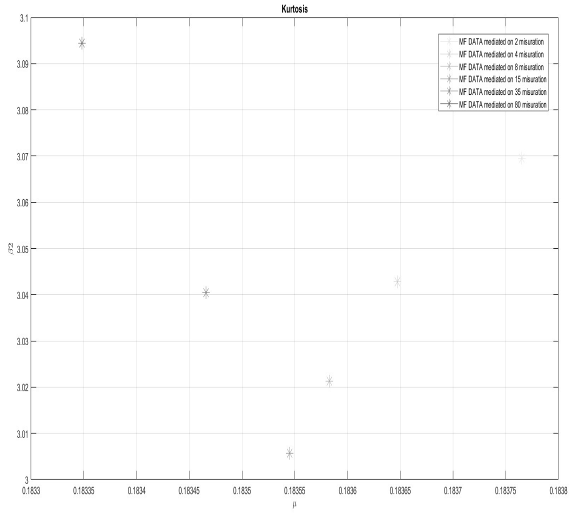

Figure 3.47: BN: KURTOSIS β_2

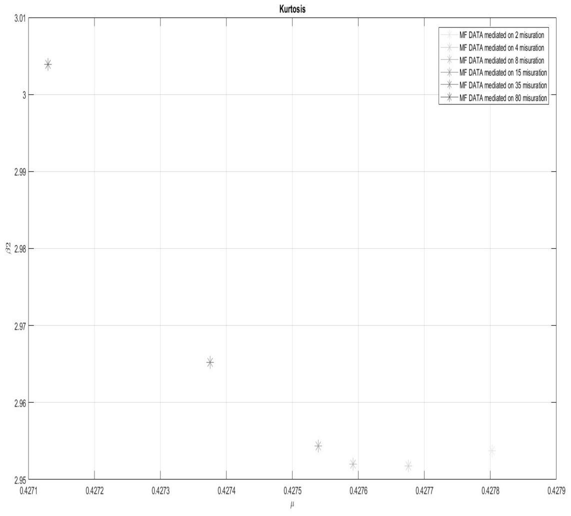

Figure 3.48: BS: KURTOSIS β_2

Kurtosis is an index that encompasses all four scenarios: tailness is stronger for higher τ, although, BS and BR show kurtosis < 3 and a thickening of the bell, whereas BT and BN show kutosis > 3, indeed they have thiner peaks.

Extrapolation

According to Fluctuation Theory [7], to extrapolate data and evaluate projections to future scenarios, magnetic field magnitude data will be used after March 2020 (last jump), because data should signify the exit from Bow shock layer and the beginning of the journey through the authentic unknown universe.

By the way, as explained in the previous paragraph, a mean time windows was chosen ($\tau = 35$), in order to evaluate distribution indexes (all aforementioned in the previous section) in all intervals obtained; then, by a linear function interpolation, mean and skewness trends were extrapolated, whereas variance was by a quadratic function.

Given the anticipation that the probes are expected to cease functioning and sending signals to ground stations by 2025, a decision has been made to conduct an assessment of future scenarios until 2028, thus necessitating a tripling of the time frame.

The following are the indexes interpolations, even if Kurtosis graph is not fundamental to extrapolation data: please note, x-axis in all picture are the number of intervals.

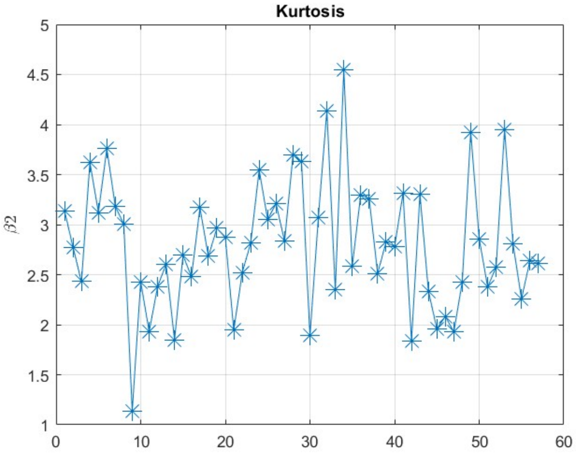

Figure 3.49: Kurtosis of magnetic field magnitude, mediated on $\tau = 35$.

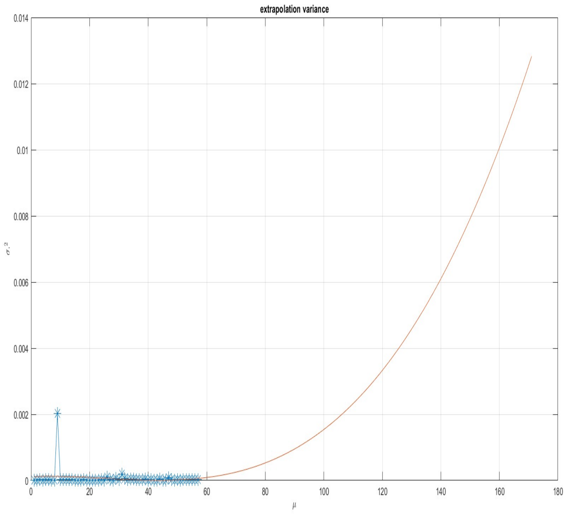

Figure 3.50: Variance of magnetic field magnitude, extrapolated.

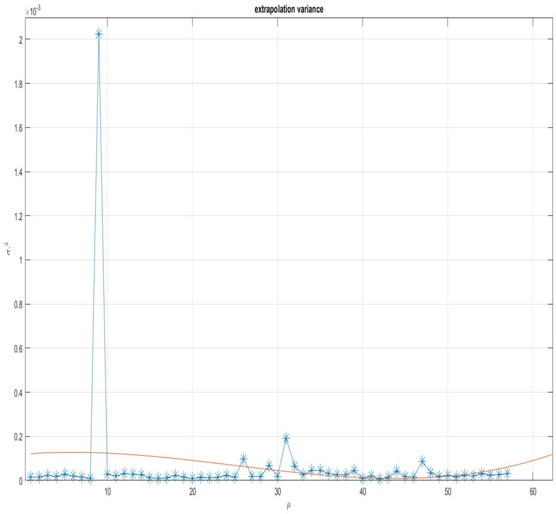

Figure 3.51: Variance of magnetic field magnitude, mediated on $\tau = 35$.

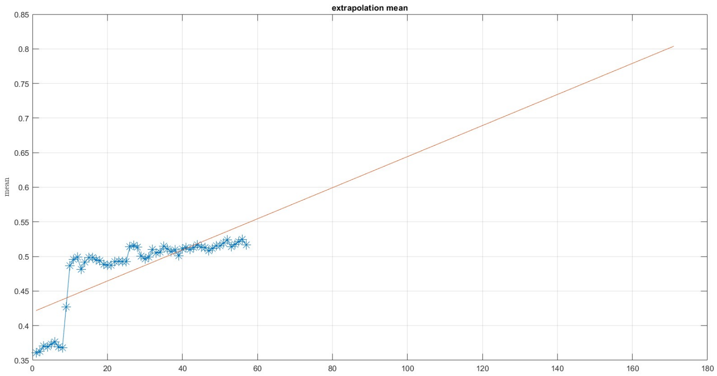

Figure 3.52: Mean of magnetic field magnitude, mediated on $\tau = 35$.

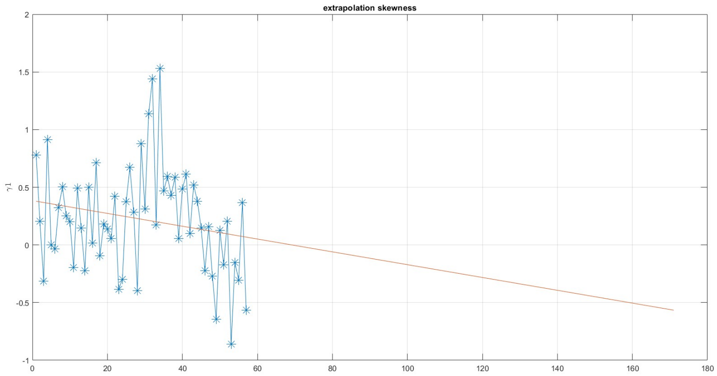

Figure 3.53: Skewness of magnetic field magnitude, mediated on $\tau = 35$.

Subsequently, once shape λ and symmetry κ factor are specified, according to projected mean values and related mode, asymmetric double exponential distribution is obtained and plotted as below:

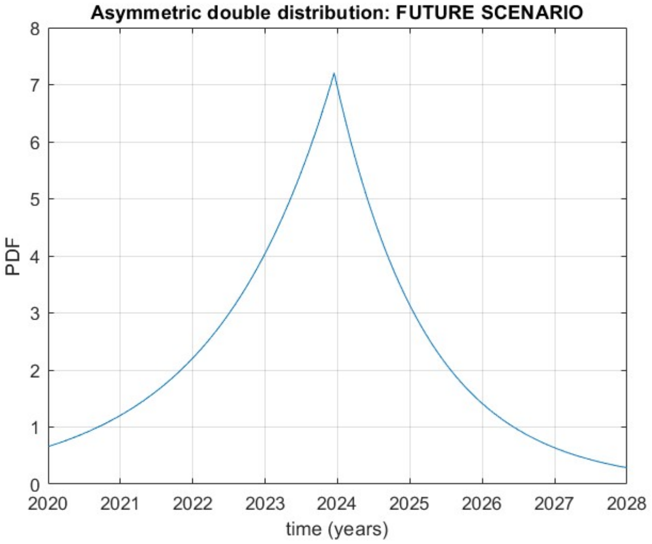

Figure 3.54: Asymmetric probability distribution function of future scenario.

As inferred from the graph, according to the probability density function (PDF), it is assumed that the magnetic values to be measured by Voyager 1 will exhibit a significantly less intense magnitude, specifically around 50% less. This implies that the values will oscillate within a range of approximately [-0.3 +0.3], and following a linear decreasing trend, may converge or possibly cancel out in approximately 54 years, at a distance of $3.5 \cdot 54 =$ approximately 190 AU.

3.4 Elaboration 1: Voyager 2

The same algorithm was implemented to evaluate data of Voyager 2 probe: here is shown the time as a function of the distance covered.

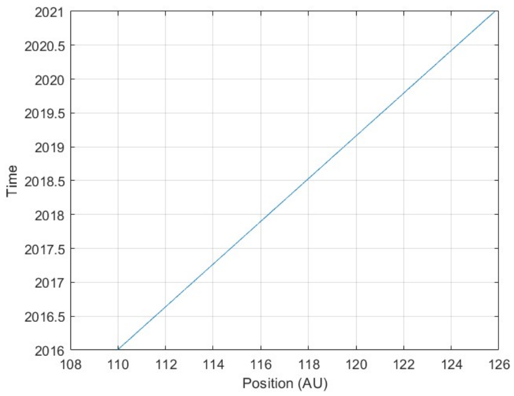

Figure 3.55: Voyager 2: path gained.

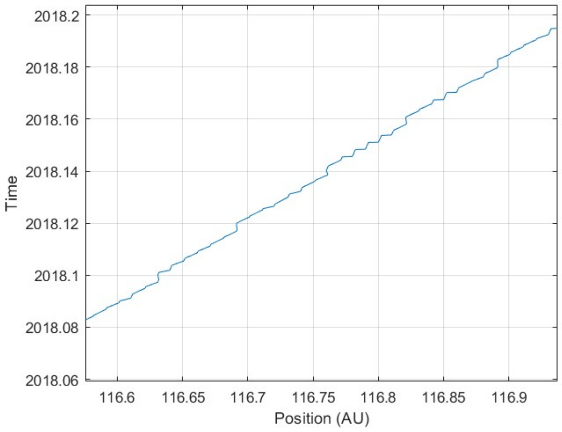

Figure 3.56: Voyager 2: path gained(zoom).

Crucial is to highlight that Voyager 2 entered in Interstellar Medium zone in 2018, so analysed data cover from the end of Outer Heliosphere to early Interstellar Medium: trends and data distributions will be significant, especially considering a pronounced excursion in the magnitude of measurements.

At the same evaluation time frame, in Voyager 2 case, it's possible to observe the environment when probe was officially escaping the Heliosphere, whereas in Voyager 1 case, data are only related to Interstellar Medium.

3.4.1 Magnetic field components

Raw data

Also Voyager 2 data are affected to full scale data, then filtered data result:

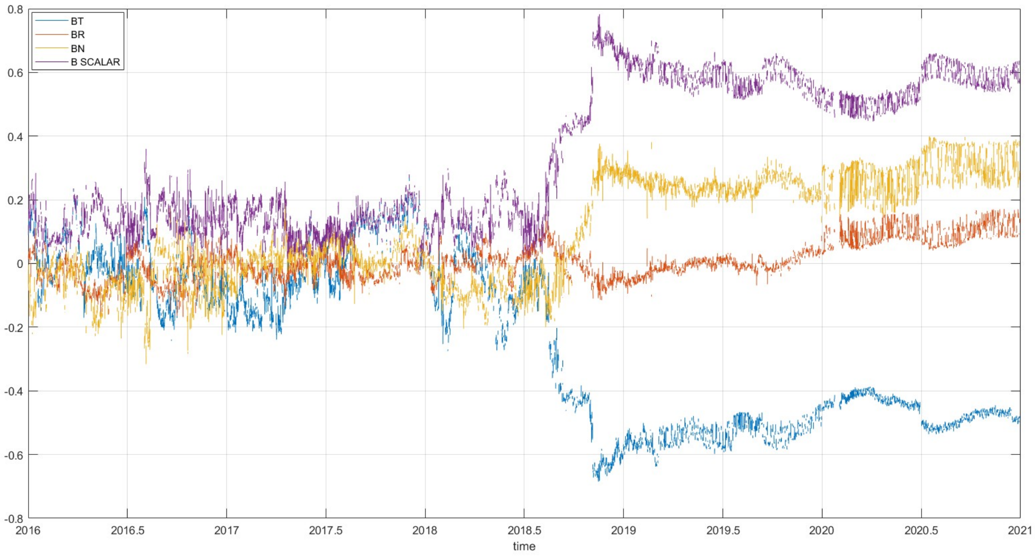

Figure 3.57: Voyager 2: complete data.

Before June 2018, when the probe was already under Solar gravitational field influence, all components exhibit almost the same behaviour, besides after crossing Heliosheat just radial component continued to show the previous trend, while normal component slightly increased. Tangential component had a strong decreasing to negative values, otherwise magnitude substantially increased by quadrupling its amplitude.

Probability function

It has been chosen to select as time window amplitude : $\tau = [2\ 4\ 8\ 15\ 22\ 100]$.

As in previous chapter, firstly all components normalized histograms are plotted by comparing all τ values, then probability density functions are calculated by extracting data by histogram trends. On x-axis, mediated data are scaled by average mean, as before. Histograms are displayed below:

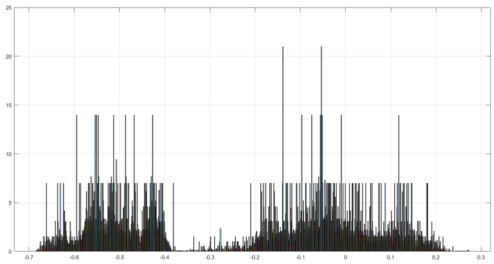

Figure 3.58: BT: histograms by several τ mediated intervals.

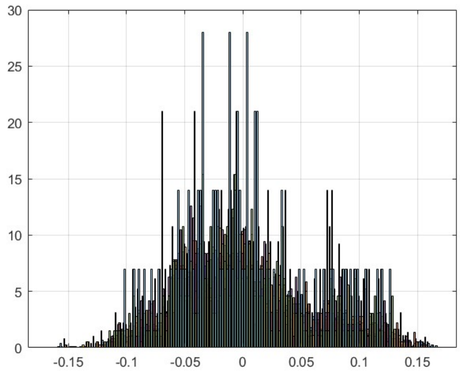

Figure 3.59: BR: histograms by several τ mediated intervals.

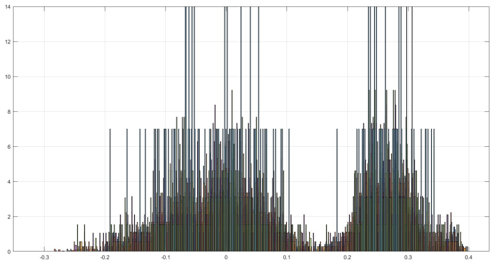

Figure 3.60: BN: histograms by several τ mediated intervals.

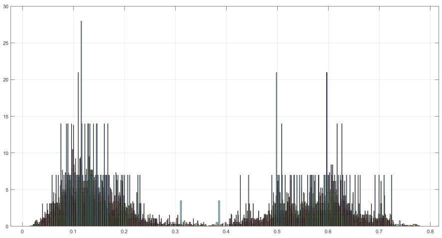

Figure 3.61: BS: histograms by several τ mediated intervals.

As mentioned earlier, in the case of the radial component, a single peak is observed, resulting from the imperceptible variation of data between the first and second zones. In contrast, for the other two components and the magnitude, this does not occur; two distinct distribution peaks emerge, corresponding to data before and after exiting the outer heliosphere.

Then, PDFs are extracted:

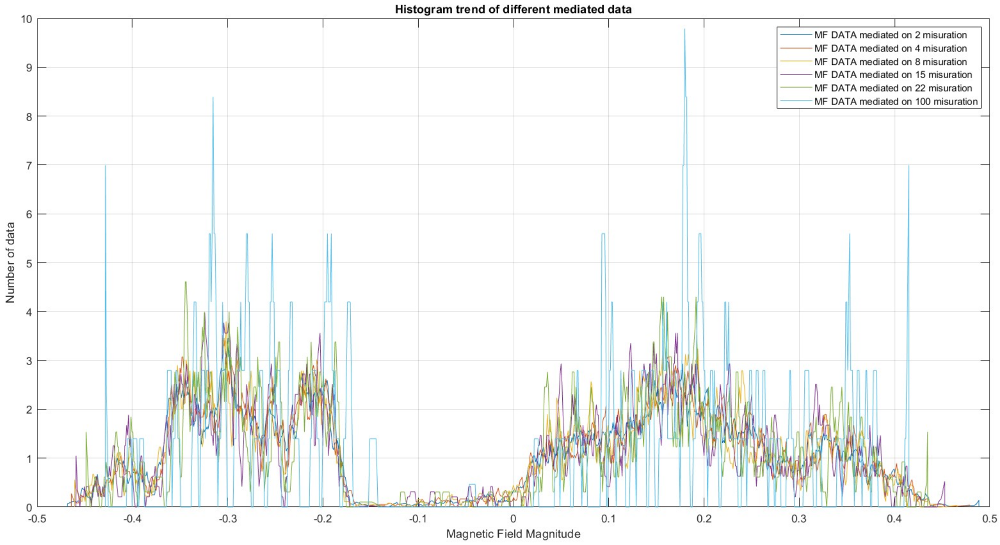

Figure 3.62: BT: PDFs by several τ mediated intervals.

Similarly, the higher is τ, the more the measure oscillates around the mode and the less the dispersion is.

Decide to assess by $\tau = 100$ is a way to evaluate an extreme behaviour.

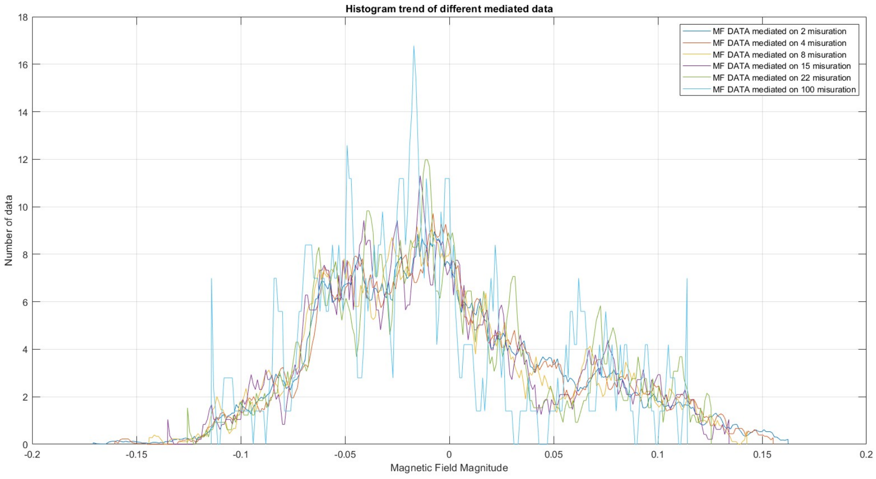

Figure 3.63: BR: PDFs by several τ mediated intervals.

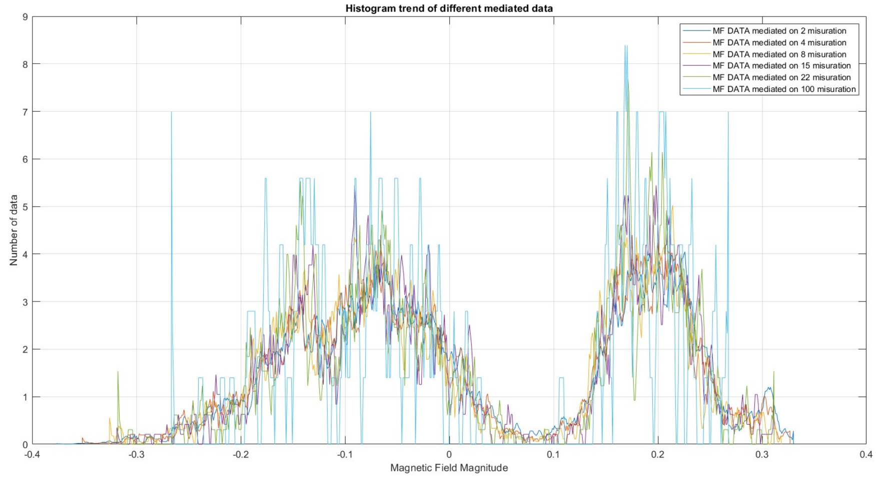

Figure 3.64: BN: PDFs by several τ mediated intervals.

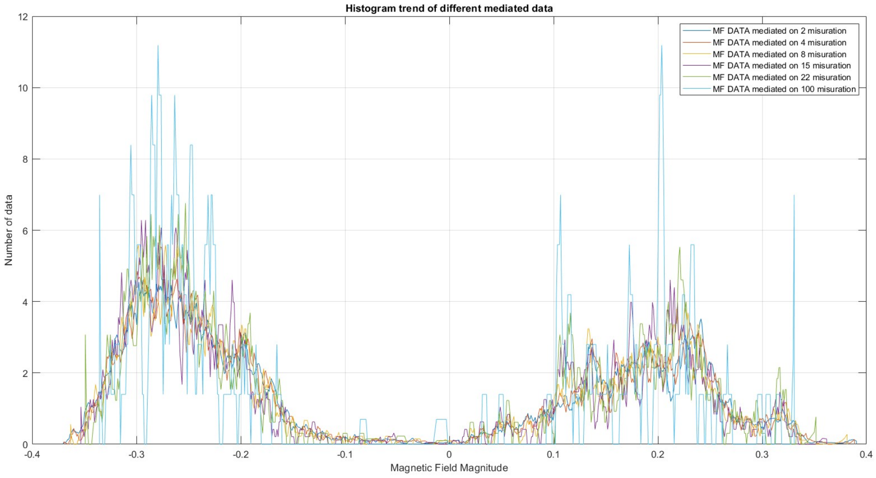

Figure 3.65: BS: PDFs by several τ mediated intervals.

Interesting is visualize Asymmetric Laplace distributions obtained by both tails linear interpolations.

Again, lighter curves mean $\tau = 2$, whereas darker ones mean increasing τ, up to $\tau = 100$.

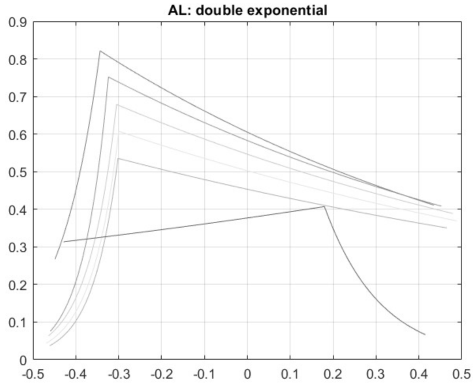

Figure 3.66: BT: ALDs by several τ mediated intervals.

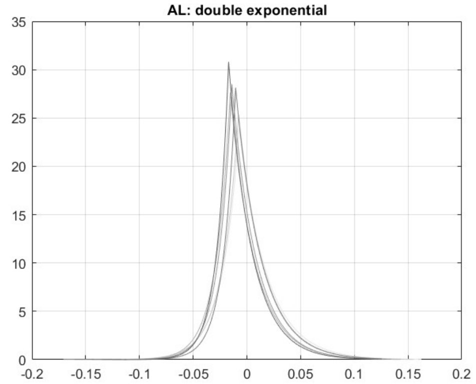

Figure 3.67: BR: ALDs by several τ mediated intervals.

According to τ, ALDs have positive or negative asymmetry: it depends on how the sampling is carried out, and consequently, the handling of data mediation.

Radial component exhibits an uniform distribution.

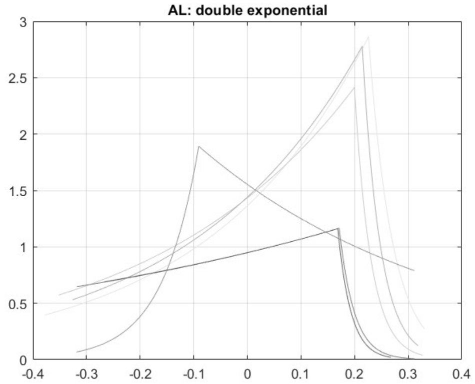

Figure 3.68: BN: ALDs by several τ mediated intervals.

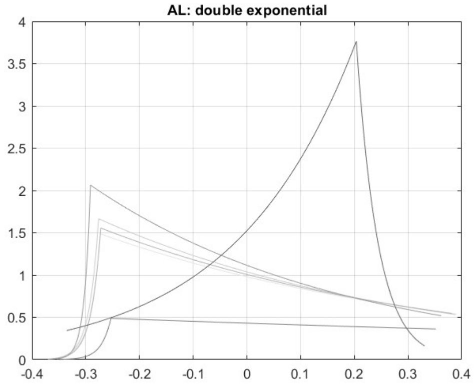

Figure 3.69: BS: ALDs by several τ mediated intervals.

In magnitude case, it was decided to show non only the overall ALDs, but also singular ones related to both first and second peaks, by selecting separately lower or higher values than 0.36 nT, which respectively correspond to first and second peak

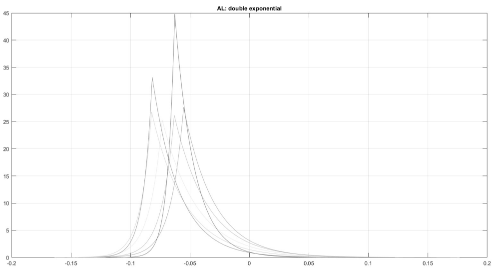

Figure 3.70: BS: ALDs by values < 0.36

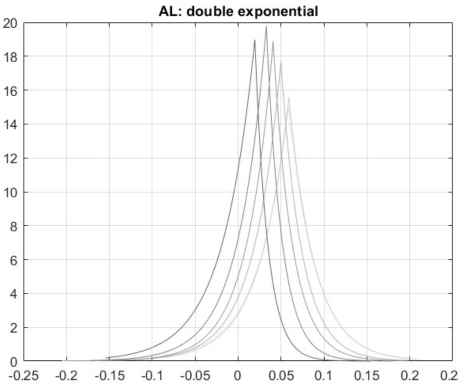

Figure 3.71: BS: ALDs by values > 0.36

Asymmetric Laplace distributions relate to Interstellar Medium data, show an linear increasing trend: if ALDs of other components of separate data were displayed, they would have the same behaviour –> maybe, are these trends might mean that the evolution of magnetic field in Interstellar Medium is more organized ?

Scaling

Then, it's needed to scale the PDFs in order to compare all ones to the overall system: so each PDF side is scaled by a factor of its corresponding slope. Given that each graph exhibits multiple peaks, and thus multiple values for right and left slopes, the overall scaled PDF graph is of little utility and challenging to interpret. Therefore, for each component (except the radial one, which has a single peak), it was chosen to assess scaling for the two peaks separately. Specifically, for the tangential component, which exclusively features negative values, the first peak's values are below -0.36 nT, while those of the second peak are higher. For the normal component, the determinant magnetic field value is +0.14 nT, whereas for the magnitude, it is +0.36 nT (as previously mentioned in the comparison of ALD graphs).

The following is the linear and logarithm scaling of radial magnetic field component:

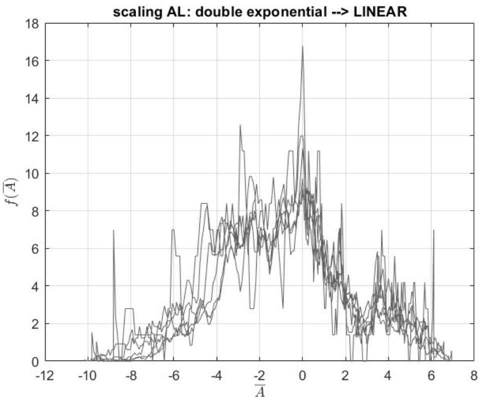

Figure 3.72: BR: PDF linear scaling

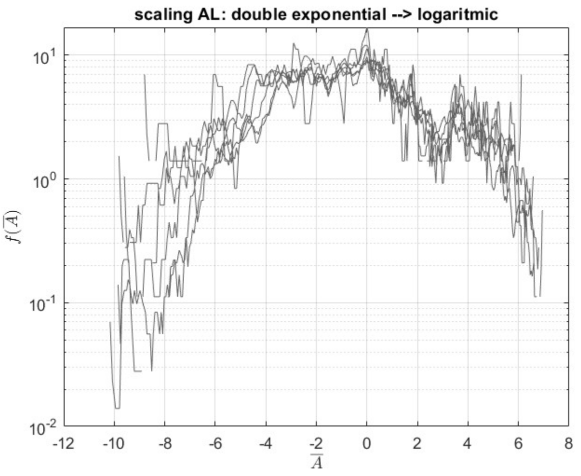

Figure 3.73: BR: PDF logarithm scaling

Then, first and second peak linear scaling of others component are displayed:

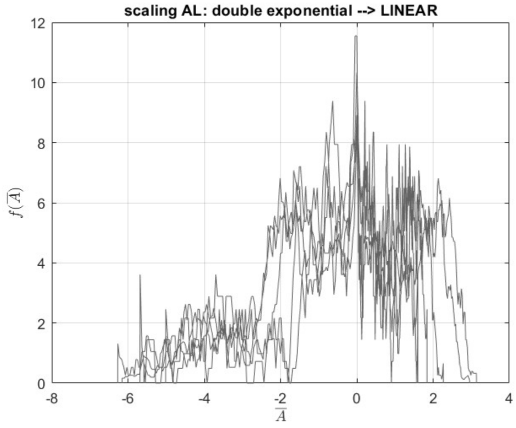

Figure 3.74: BT: PDF linear scaling (1° peak)

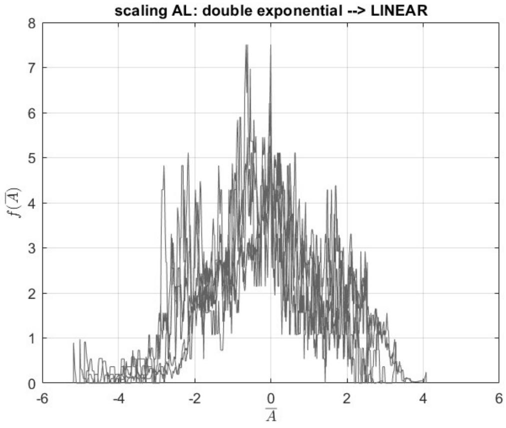

Figure 3.75: BT: PDF linear scaling (2° peak)

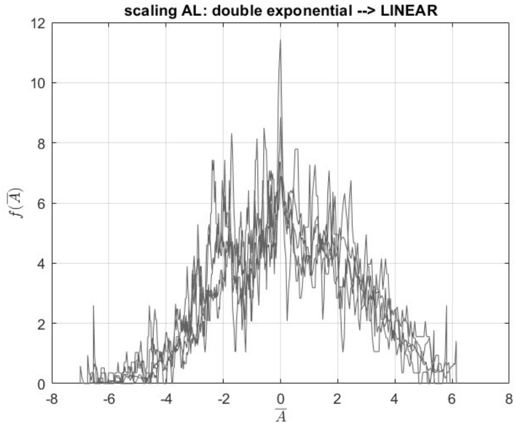

Figure 3.76: BN: PDF linear scaling (1° peak)

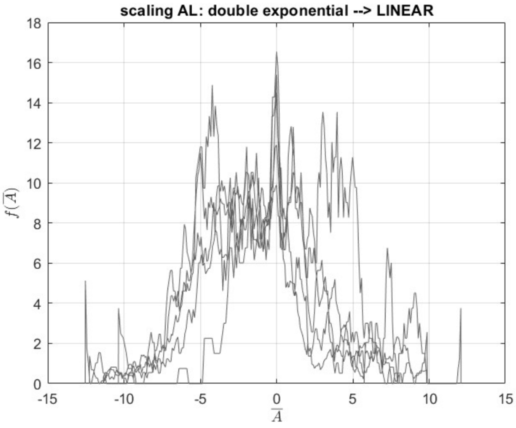

Figure 3.77: BN: PDF linear scaling (2° peak)

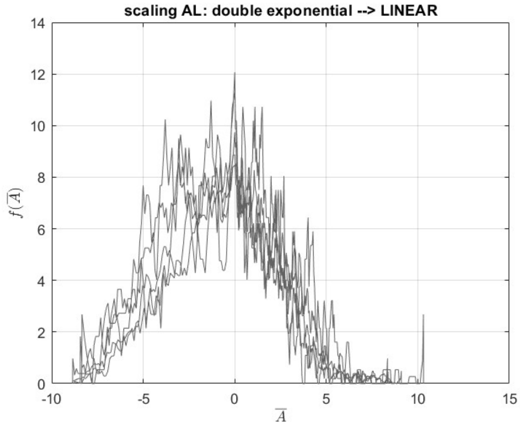

Figure 3.78: BS: PDF linear scaling (1° peak)

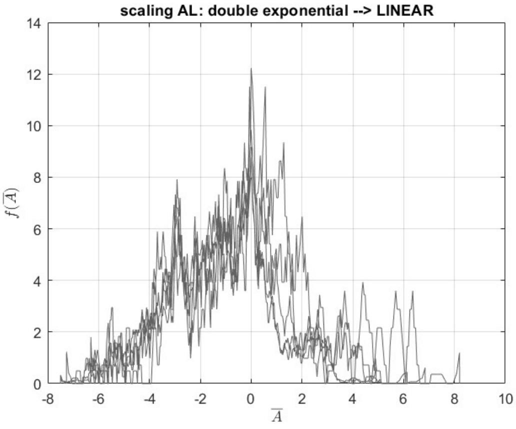

Figure 3.79: BS: PDF linear scaling (2° peak)

To give a deeper look and better visualize scaling path, also logarithm scaled PDFs are exhibit:

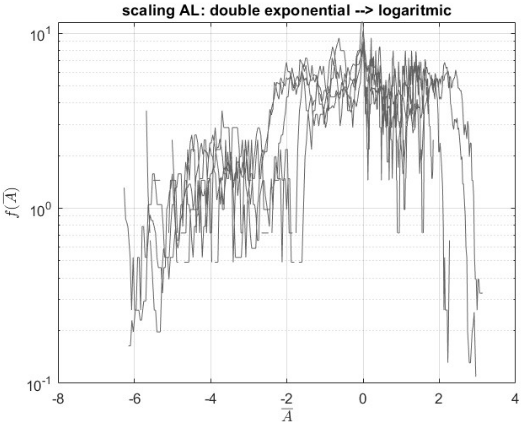

Figure 3.80: BT: PDF logarithm scaling (1° peak)

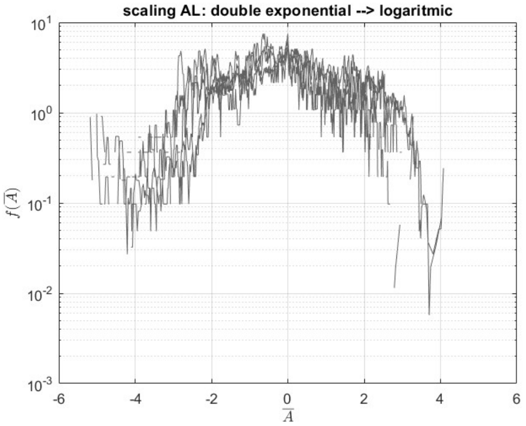

Figure 3.81: BT: PDF logarithm scaling (2° peak)

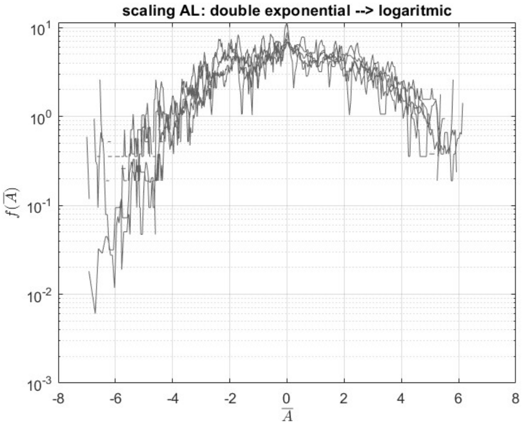

Figure 3.82: BN: PDF logarithm scaling (1° peak)

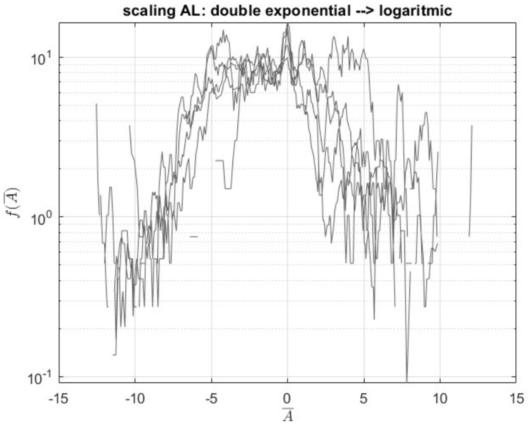

Figure 3.83: BN: PDF logarithm scaling (2° peak)

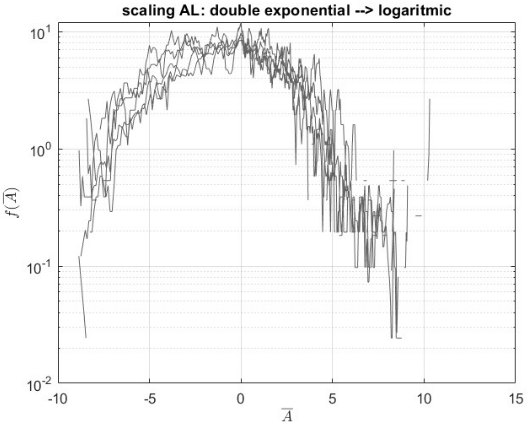

Figure 3.84: BS: PDF logarithm scaling (1° peak)

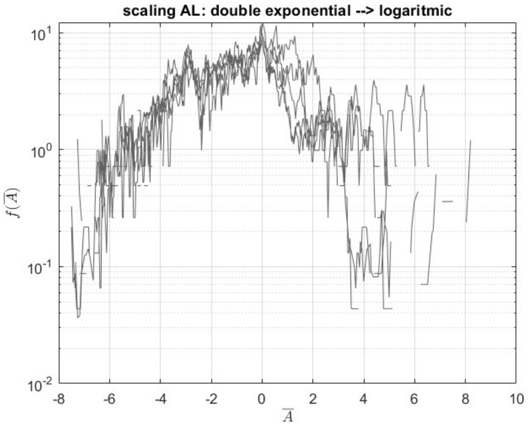

Figure 3.85: BS: PDF logarithm scaling (2° peak)

Symmetry factor

Also for symmetry factor, which is provided by the ration of the functions interpolated in query points, away from the mode m by a factor of + o -α. It's calculated on overall range of data, for every components.

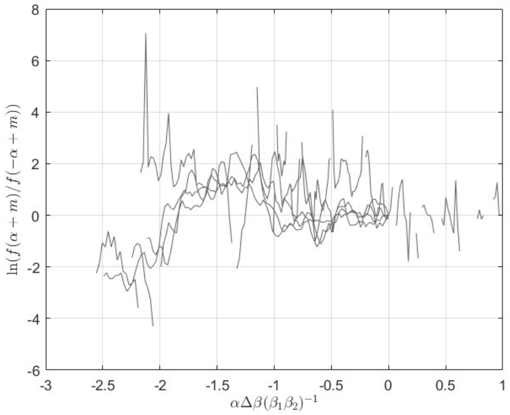

Figure 3.86: BT: symmetry factor

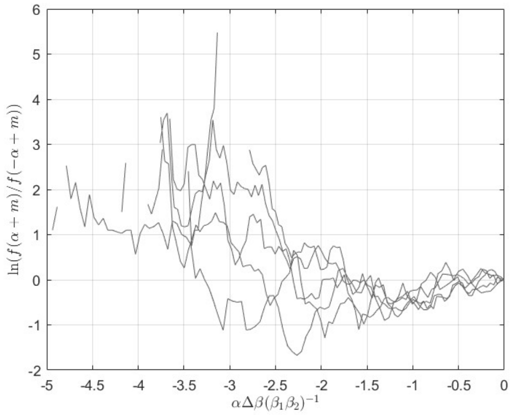

Figure 3.87: BR: symmetry factor

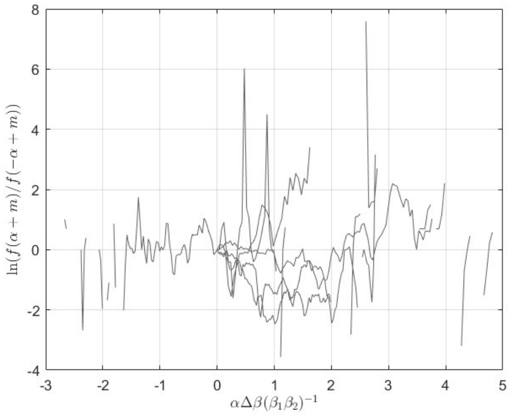

Figure 3.88: BN: symmetry factor

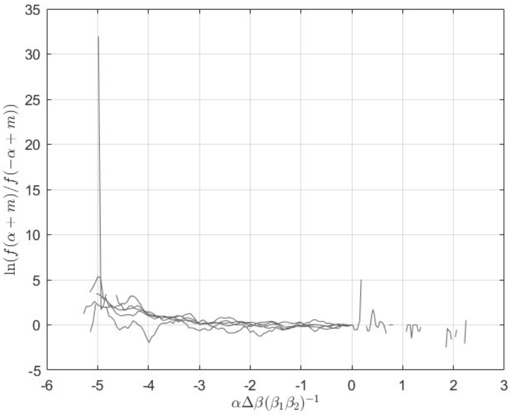

Figure 3.89: BS: symmetry factor

The symmetry factor does not exhibit a clear trend; instead, there are possibly oscillations that appear shifted as the value of τ increases. This discontinuous trend is linked to the inherently discontinuous nature of the PDFs derived from the histograms, where, in general, some PDFs are higher and narrower than others. However, the fact is that if each bar were observed locally, this is not always respected. The measured data is quite chaotic, making it impossible to obtain a constant trend. Nevertheless, the symmetry factor of the magnetic field magnitude is very interesting: even though the PDF has two peaks, the symmetry factor indicates that the first peak, corresponding to lower magnitude data, is more recurrent and, thus, manages to overpower the distribution effect of interstellar medium data, resulting in an almost constant symmetry factor.

Distribution indexes

Distribution indexes are evaluated on mediate data by all τ values: lighter * indicates the index related to the lower number of intervals, thus $\tau = 2$, otherwise $\tau = 100$ is signed by darker *.

Let's see how indexes behave, comparing to Voyager 1 magnetic field data.

- Variance:

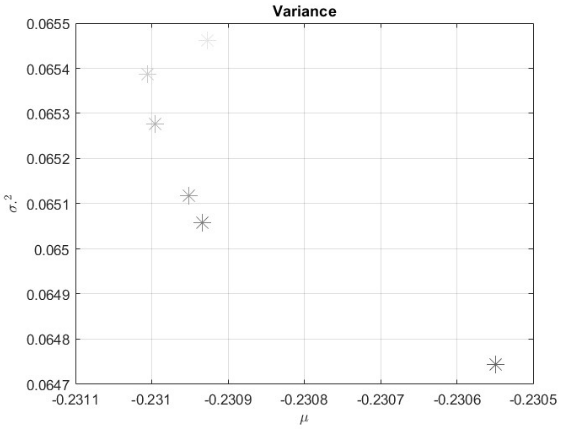

Figure 3.90: BT: Variance σ^2

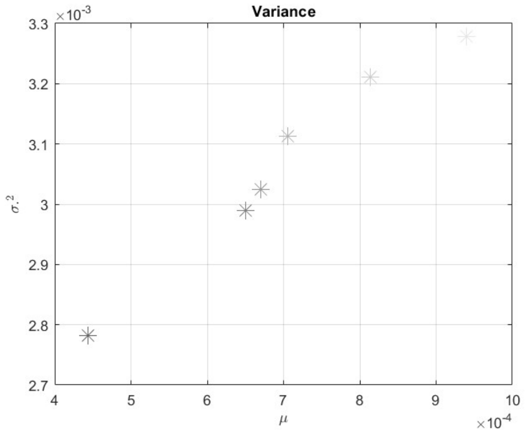

Figure 3.91: BR: Variance σ^2

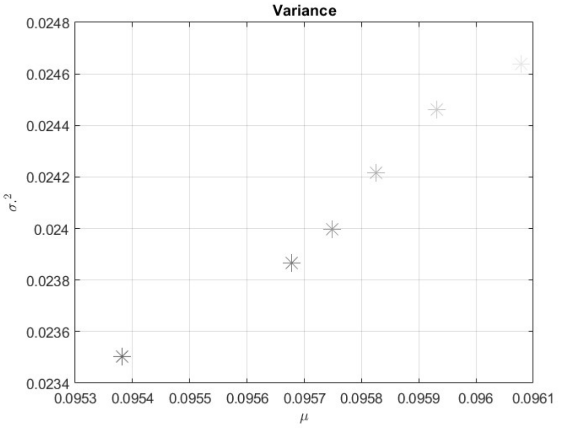

Figure 3.92: BN: Variance σ^2

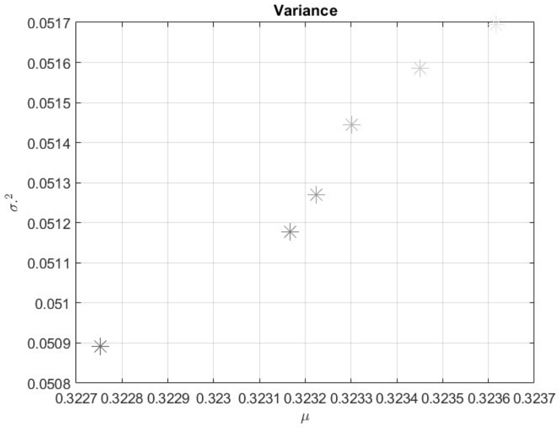

Figure 3.93: BS: Variance σ^2

The trends are completely the same; the variance (dispersion index) decreases as the precision of the distribution, given by data mediation, increases: the higher the value of τ, the lower σ^2 is. Naturally, the trend of the tangential component is specular since the measurements are negative, and the absolute values tend to be larger towards the left, as opposed to the right as in the other cases. Compared to the indices evaluated on the data from Voyager 1, the trends are mainly linear, decreasing, and regressive, whereas for Voyager 1, non-linear (quadratic) regressive trends have been observed.

- Skewness:

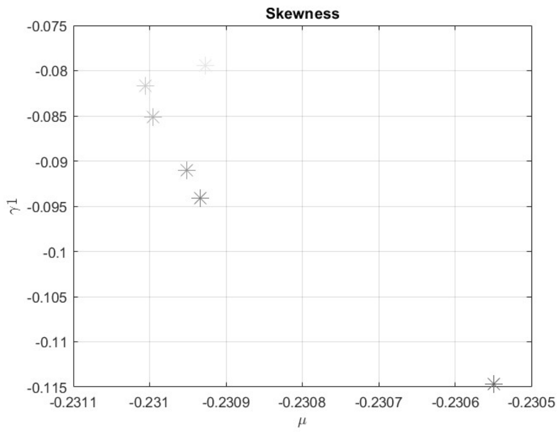

Figure 3.94: BT: Skewness γ_1

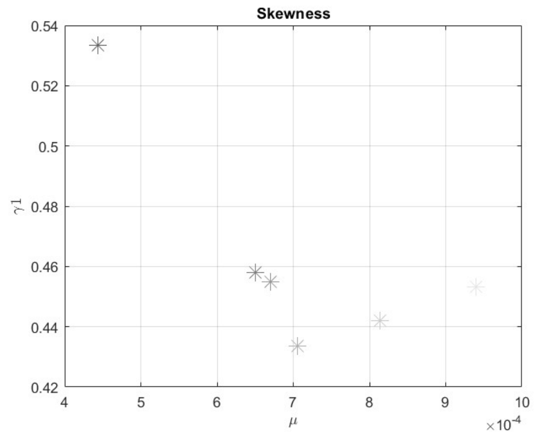

Figure 3.95: BR: Skewness γ_1

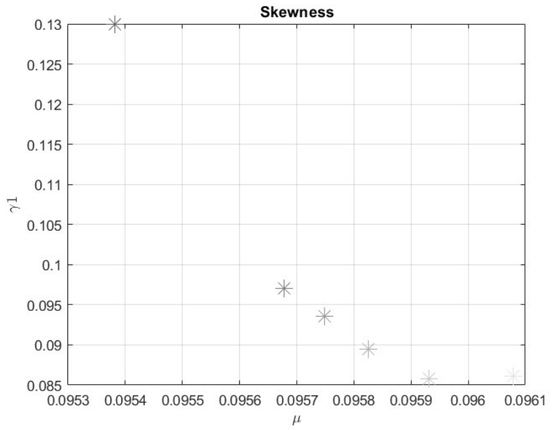

Figure 3.96: BN: Skewness γ_1

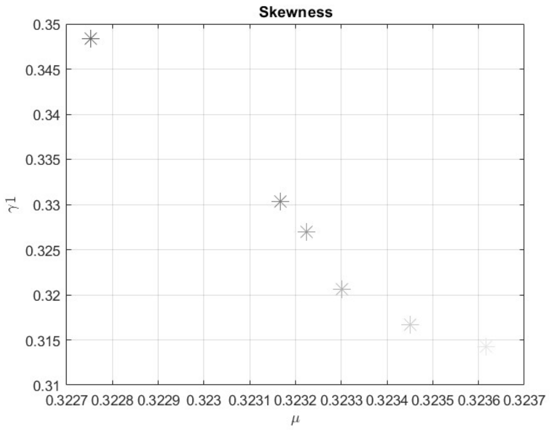

Figure 3.97: BS: Skewness γ_1

In the case of skewness, the same reasoning applies: linear decreasing trends. A larger τ indicates a higher (in magnitude) skewness index. Indeed, the tangential component once again exhibits a specular trend, as it has a negative skewness.

- Kurtosis:

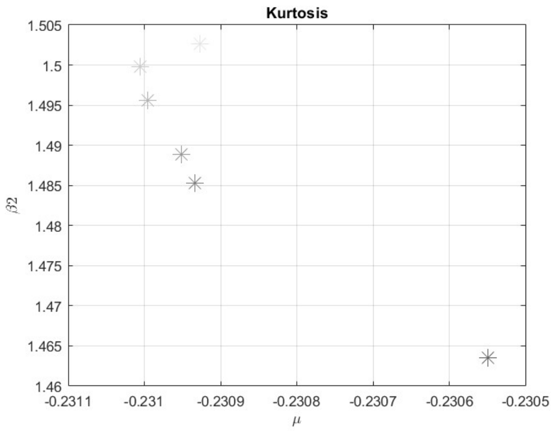

Figure 3.98: BT: Kurtosis β_2

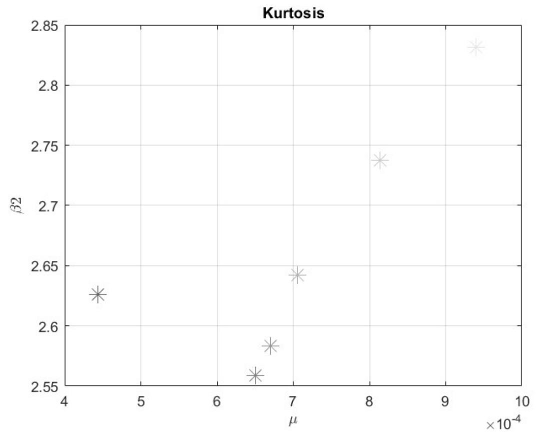

Figure 3.99: BR: Kurtosis β_2

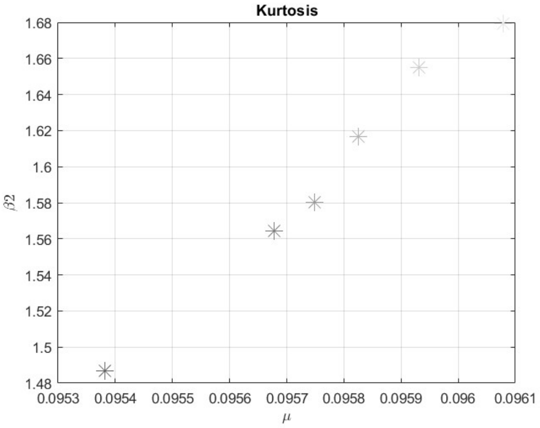

Figure 3.100: BN: Kurtosis β_2

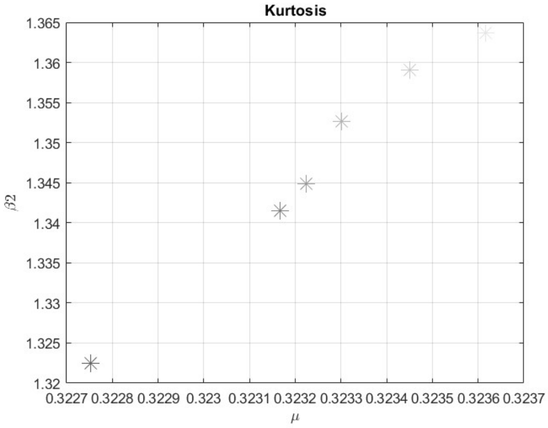

Figure 3.101: BS: Kurtosis β_2

Again, indexes trends are confirmed: tangential magnetic component has specular one.

Extrapolation

According to Fluctuation Theory, to extrapolate data and evaluate projections to future scenarios, magnetic field magnitude data will be used after June 2018 (entrance date to Interstellar Medium zone).

By the way, as applied in the previous paragraph, a mean time windows was chosen ($\tau = 45$), in order to evaluate distribution indexes (all aforementioned in the previous section) in all intervals obtained; then, by a linear function interpolation, mean and skewness trends were extrapolated, whereas variance was by a quadratic function.

Given the anticipation that the probes are expected to cease functioning and sending signals to ground stations by 2025, a decision has been made to conduct an assessment of future scenarios until end of 2028, thus necessitating a tripling of the time frame.

The following are the indexes interpolations, even if Kurtosis graph is not again fundamental to extrapolation data: please note, x-axis in all picture are the number of intervals.

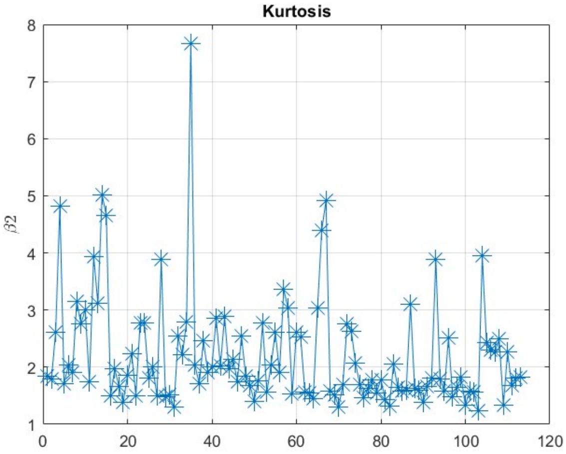

Figure 3.102: Kurtosis of magnetic field magnitude, mediated on $\tau = 45$.

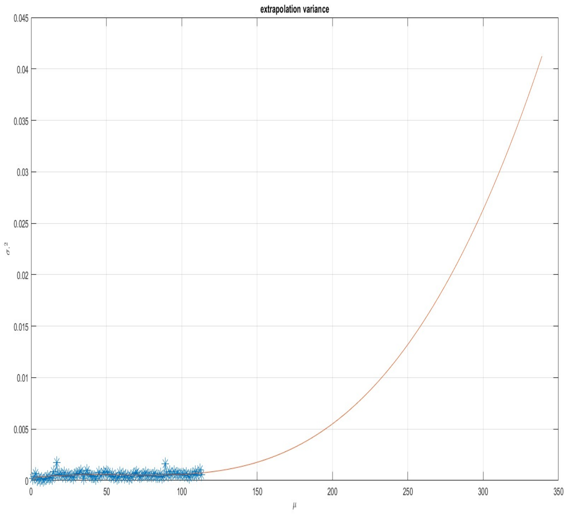

Figure 3.103: Variance of magnetic field magnitude, extrapolated.

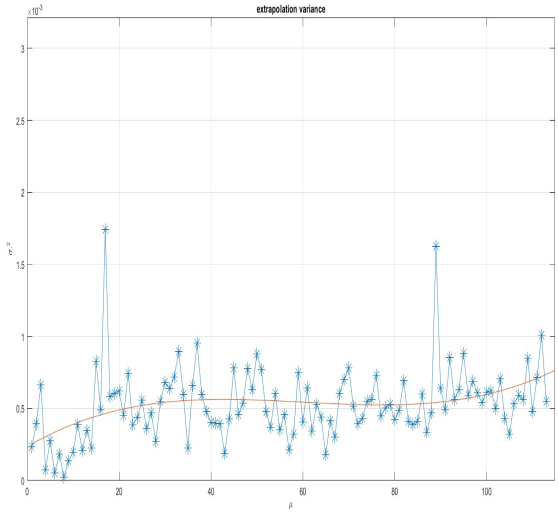

Figure 3.104: Variance of magnetic field magnitude, mediated on $\tau = 45$.

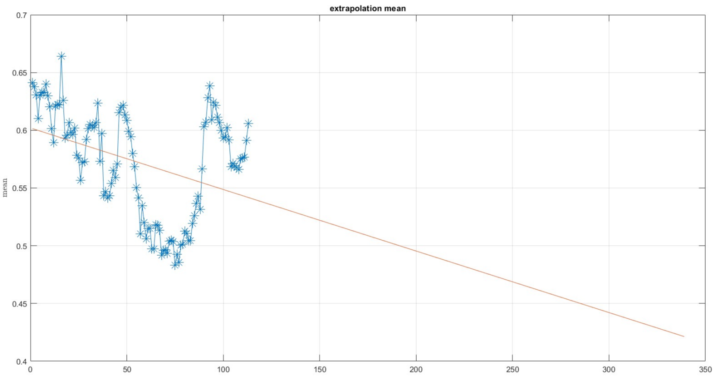

Figure 3.105: Mean of magnetic field magnitude, mediated on $\tau = 45$.

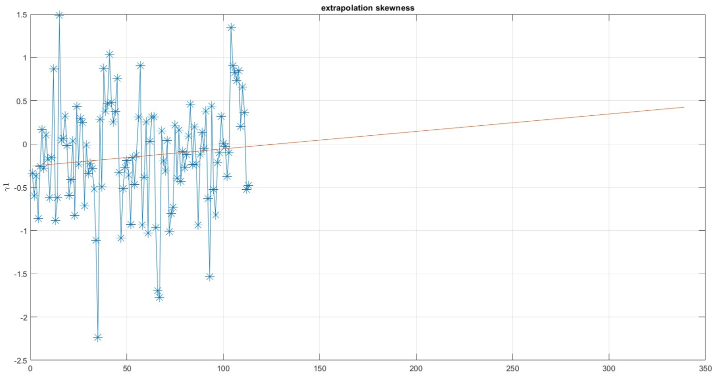

Figure 3.106: Skewness of magnetic field magnitude, mediated on $\tau = 45$.

Subsequently, once shape λ and symmetry κ factor are specified, according to projected mean values and related mode, asymmetric double exponential distribution is obtained and plotted as below:

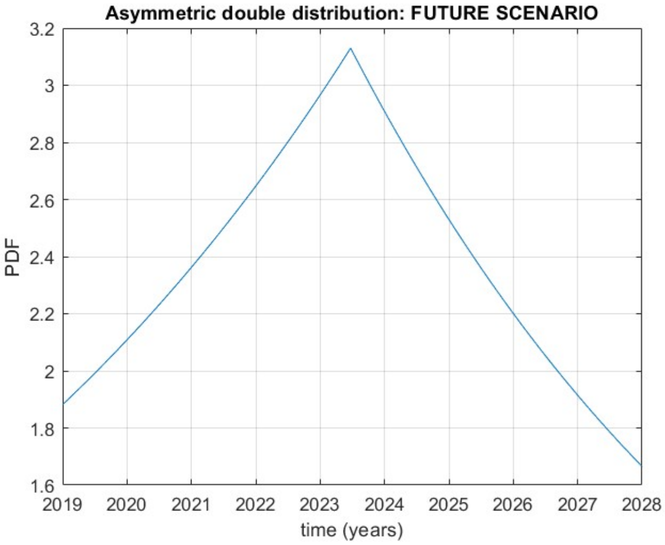

Figure 3.107: Asymmetric probability distribution function of future scenario.

As inferred from the graph, according to the probability density function (PDF), it is assumed that the magnetic values to be measured by Voyager 2 will exhibit a magnitude less, specifically around 10% less. This implies that the values will oscillate within a range of approximately [+0.5 +0.8], and following a linear decreasing trend, may converge or possibly cancel out in approximately 180 years, at a distance of $3.3 \cdot 180 =$ approximately 594 AU.

3.4.2 Proton parameters

The data related to protons has been collected in a time range from January 2016 to November 2019, due to the interruption of data collection device operation. These data are very interesting as analyzing them allows examining velocity, density, and temperature, but especially predicting density in view of reaching the bow shock. However, the present methodology requires data on the order of units to adequately generate graphs of distributions, both asymmetric and not, and indices. For this reason, each parameter will be multiplied by a certain factor as follows:

- Density: 10^2
- Temperature: 10^{-6}
- Speed: 10^{-3}

However, to perform extrapolation, it is necessary to use the original and unadjusted data. Therefore, the indices, by imposing a certain τ, will be computed based on the initial density data.

Raw data

In this case, the measurements taken by the proton detectors have always remained very limited compared to the scale value of the device. Therefore, the dataset provided by NASA is complete with all the data and does not appear scattered, even though limited, as stated before, until the end of 2018.

Here complete data, taken by OmniWeb@NASA, about density, temperature and speed.

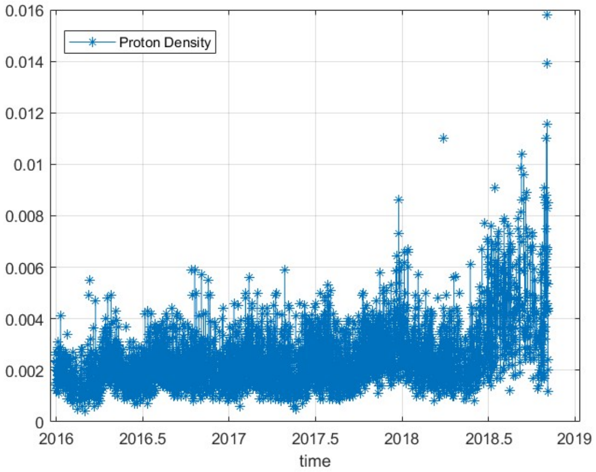

Figure 3.108: Density of protons.

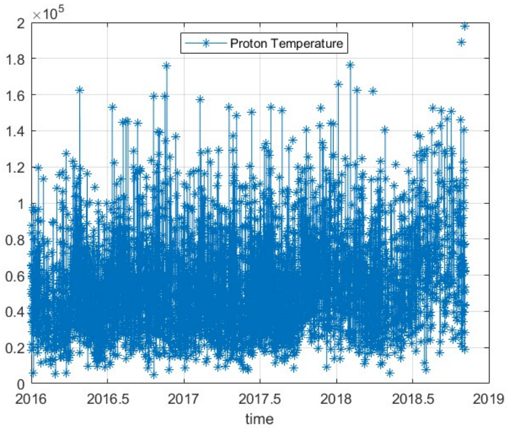

Figure 3.109: Temperature of protons.

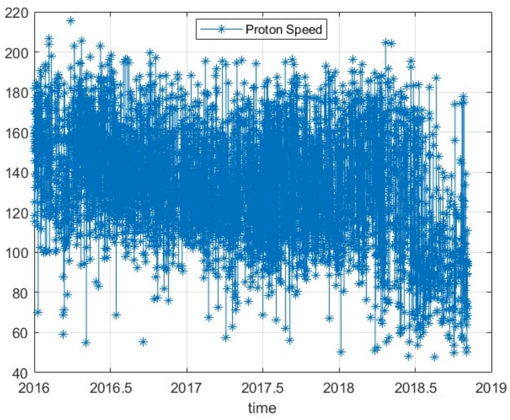

Figure 3.110: Speed of protons.

Probability function

The methodology applied is the same to magnetic field components' one: once probability histograms have been evaluated, PDFs trends have been extracted. Then, by linearizing right and left tails, respective slopes have been computed in order to obtain Asymmetric Laplace Distribution parameters. Both probability function will be displayed, compared and discussed, as previous analysis. However available proton data are much lower than the other case, thus the temporal window must be lower too : $\tau = [2\ 5\ 10\ 30]$. Where the highest value is implemented to observe extreme condition.

Here the histograms:

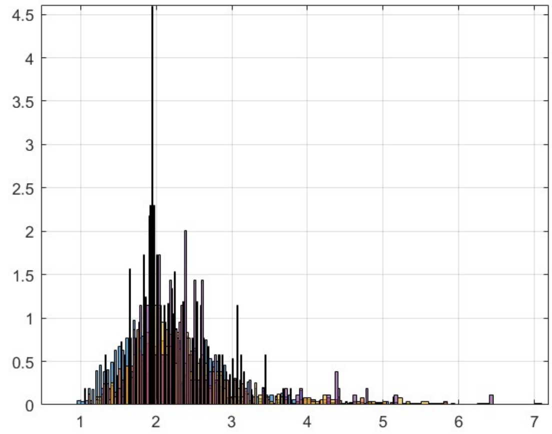

Figure 3.111: Histogram: density of protons.

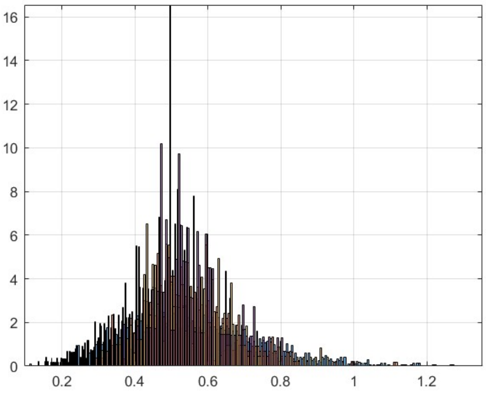

Figure 3.112: Histogram: temperature of protons.

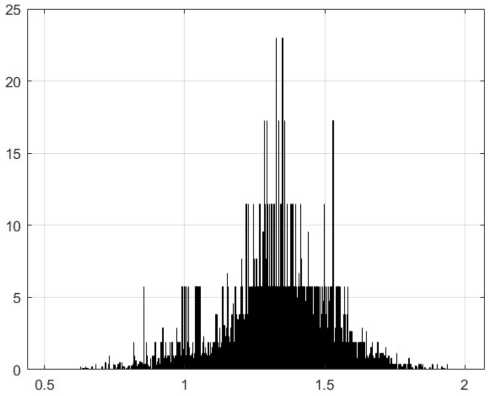

Figure 3.113: Histogram: speed of protons.

In this case, the distribution function of all variables has a single peak, so linearizing the tails to obtain quantile values will be easily applicable to the entire dataset. However, before examining the ALD (asymptotic limit distribution), histogram values are extracted to observe the trends of the PDFs at different τ.

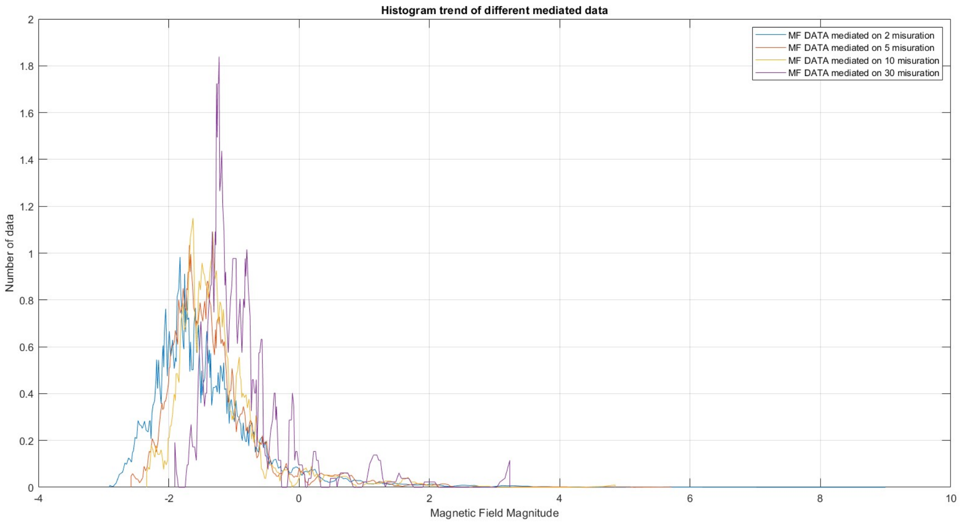

Figure 3.114: PDF at $\forall\tau$: density of protons.

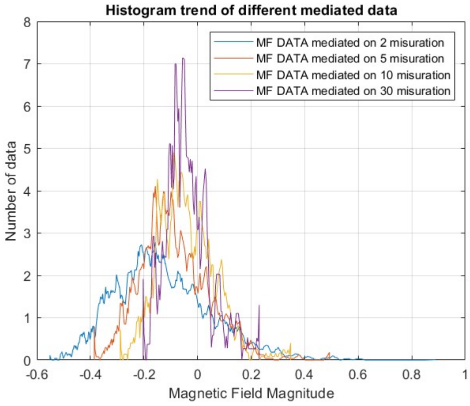

Figure 3.115: PDF at $\forall\tau$: temperature of protons.

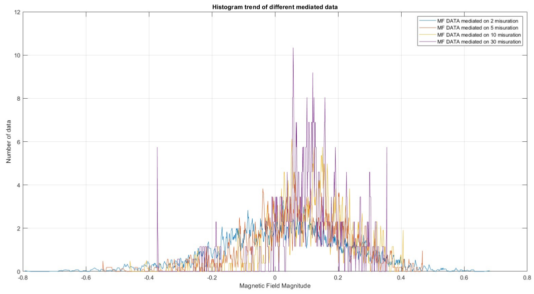

Figure 3.116: PDF at $\forall\tau$: speed of protons.

The higher τ is, the narrower and less thick is the PDF.

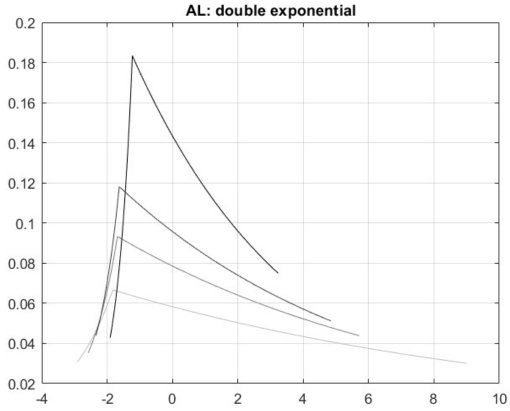

Figure 3.117: ALDs at $\forall\tau$: density of protons.

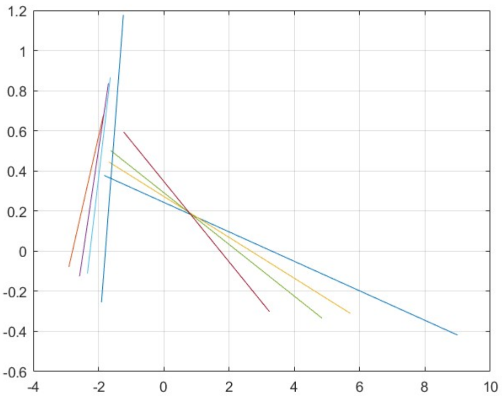

Figure 3.118: Linearizing curves: density of protons.

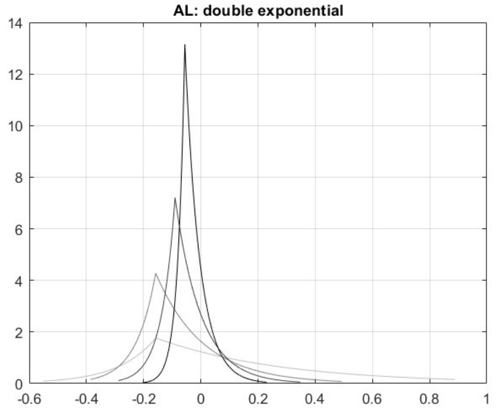

Figure 3.119: ALDs at $\forall\tau$: temperature of protons.

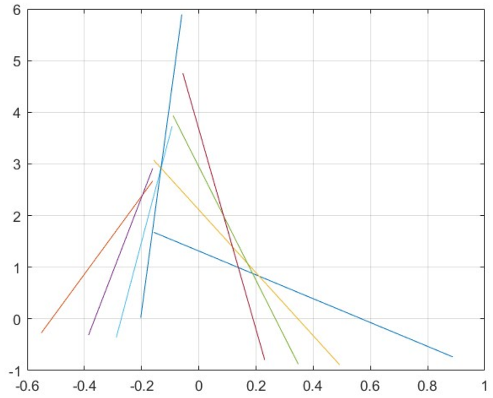

Figure 3.120: Linearizing curves: temperature of protons.

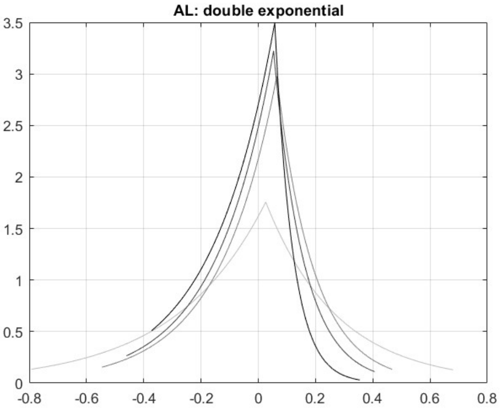

Figure 3.121: ALDs at $\forall\tau$: speed of protons.

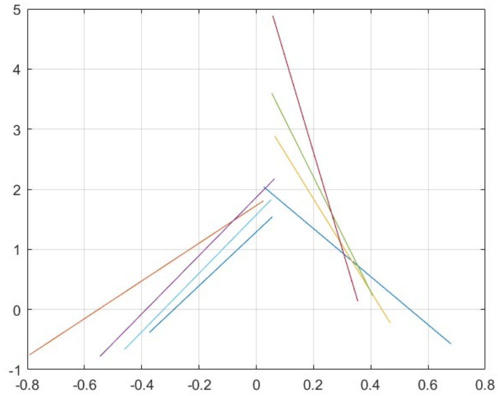

Figure 3.122: Linearizing curves: speed of protons.

Then, it's possible to compute Asymmetric Laplace Distribution. We can observe that in all plots of the double exponential distribution, the more dispersed distributions are low and wide, corresponding to lower τ values; on the contrary, the lines are higher and darker, resulting in thinner distributions for higher τ values. In all cases, there is a noticeable narrowing of the curves, along with a lowering due to the clockwise rotation of the right tail, corresponding to higher mode values. This is attributed to the high number of positive measurements compared to negative ones (scaled).

Another crucial factor to observe is symmetry: it is clear that with increasing τ, the peaks of the curves tend to shift towards the mode value, thereby reducing the asymmetry and dispersion of the examined data. Overall, the most stable and symmetric parameter is the speed of protons: one could assume that this is due to the data being collected before entering the interstellar medium, where the gravitational field effect was still predominant, capable of maintaining the kinetic energy of particles approximately constant as the radial distance increased.

Scaling

Again, we scale the variables to compare their respective PDFs to the overall system, ensuring that they have approximately the same shape. Plots are presented both in linear and logarithmic forms for better comprehension.

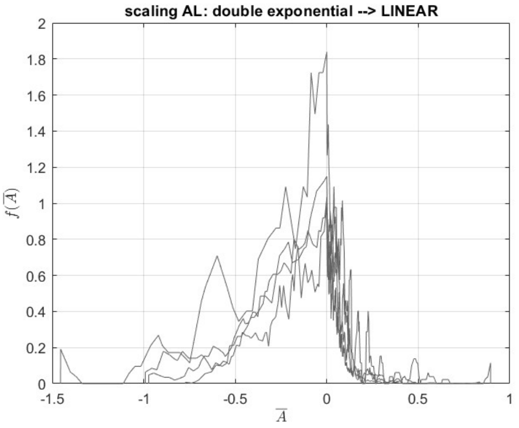

Figure 3.123: Linear scaled PDFs: density of protons.

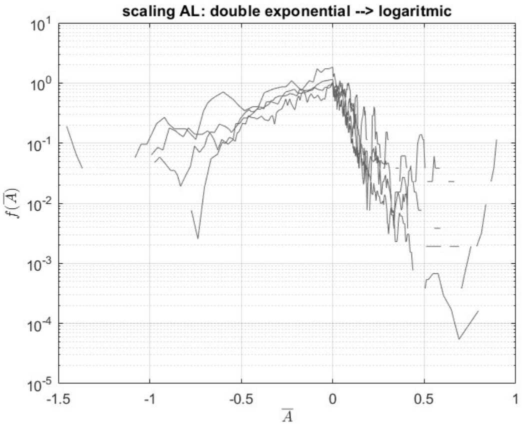

Figure 3.124: Logarithmic scaled PDFs: density of protons.

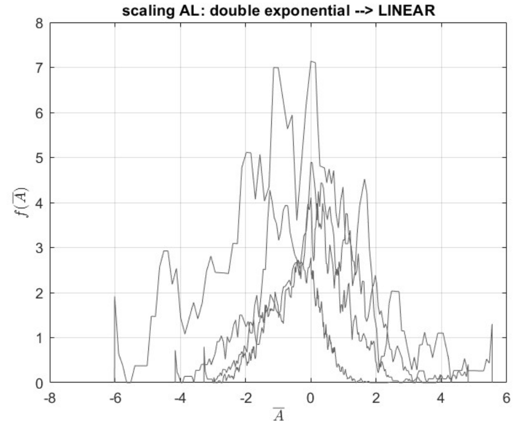

Figure 3.125: Linear scaled PDFs: temperature of protons.

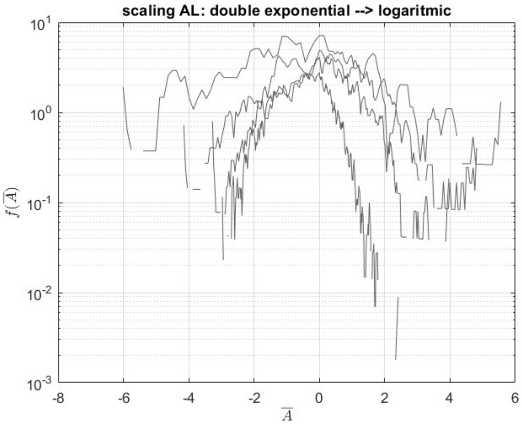

Figure 3.126: Logarithmic scaled PDFs: temperature of protons.

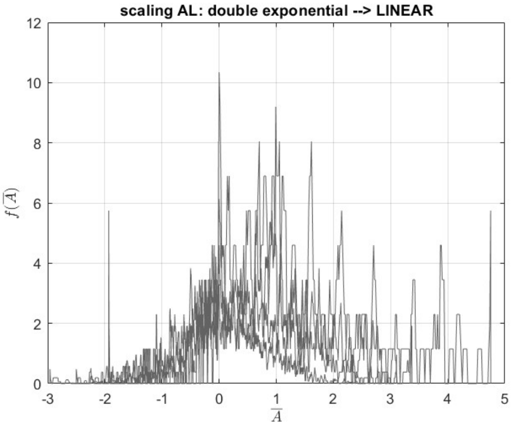

Figure 3.127: Linear scaled PDFs: speed of protons.

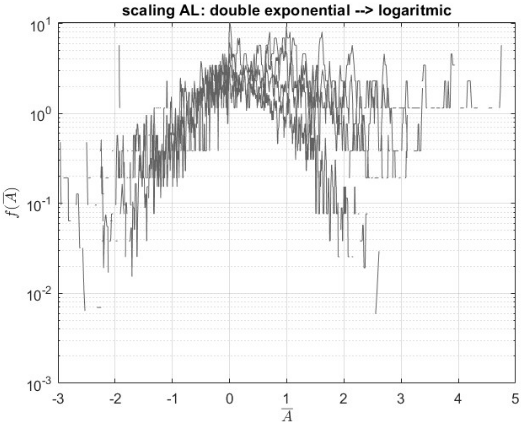

Figure 3.128: Logarithmic scaled PDFs: speed of protons.

The scaling is not extremely effective, but it can still be observed that in the plot of the same parameter, for any τ, the trend remains the same.

Symmetry factor

Subsequently, symmetry factor is computed, but it's expected to find a quite linear trend as Asymmetric Laplace Distribution's graphs have already shown PDFs symmetry.

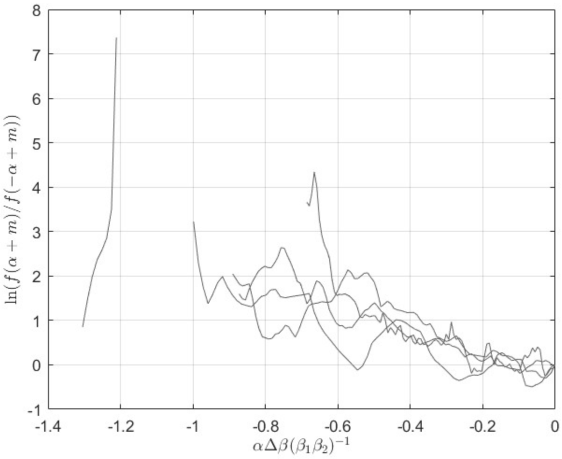

Figure 3.129: Symmetry factor: density of protons.

As anticipated, the trends for proton density and temperature are approximately linear and decreasing. However, for speed, it seems not to be the same. As already seen in the histograms, since the values are very close, the binning is not very effective, resulting in many thin bars adjacent to empty spaces. However, if one were to zoom in on the chart where the lines are not clearly visible, it would be noticed that the trend is similar to the one of the other two parameters, only composed of frequent oscillating dashed lines (for the aforementioned reasons).

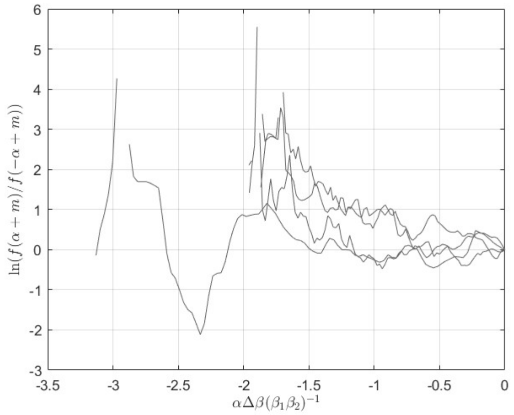

Figure 3.130: Symmetry factor: temperature of protons.

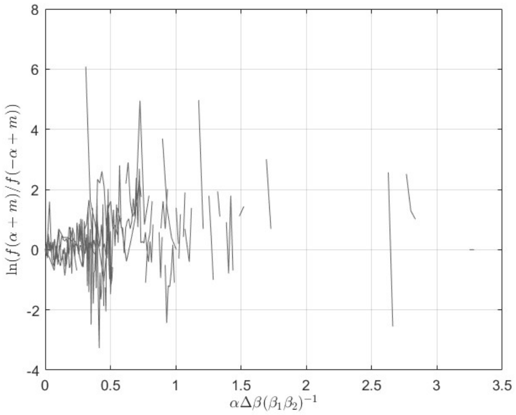

Figure 3.131: Symmetry factor: speed of protons.

Distribution indexes

Distribution indexes are comuted on data mediated on τ: again, lighter line is related to $\tau = 2$, while darker one is to $\tau = 30$.

- VARIANCE σ^2:

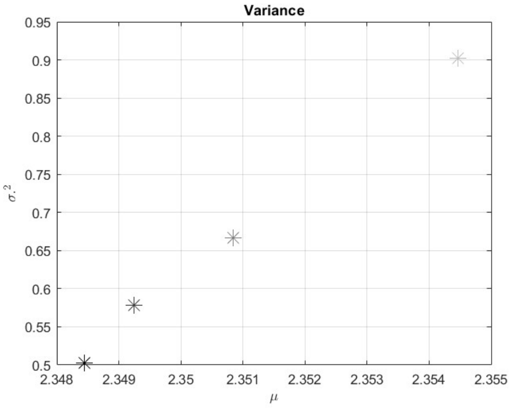

Figure 3.132: Density of protons.

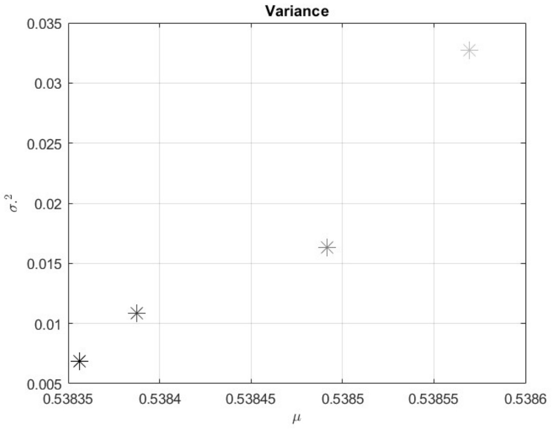

Figure 3.133: Temperature of protons.

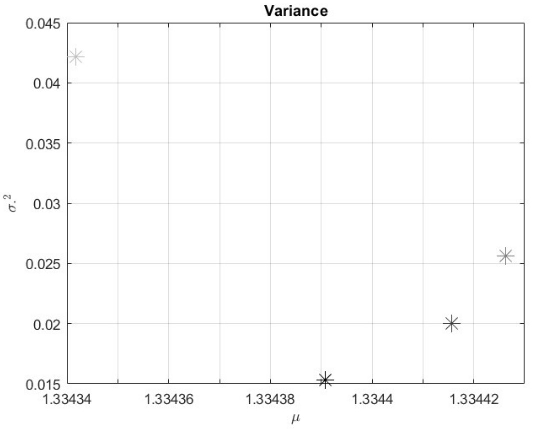

Figure 3.134: Speed of protons.

There is a decrease in variance with an increase in τ, as explained by the usual discourse on the ratio of data dispersion to the number of intervals. In the case of speed, the overall mean velocity value for $\tau = 2$ results in a variance value that is not aligned with the rest. This is due to the strong irregularity in the binning of the PDFs calculated on the speed data."

- SKEWNESS γ_1:

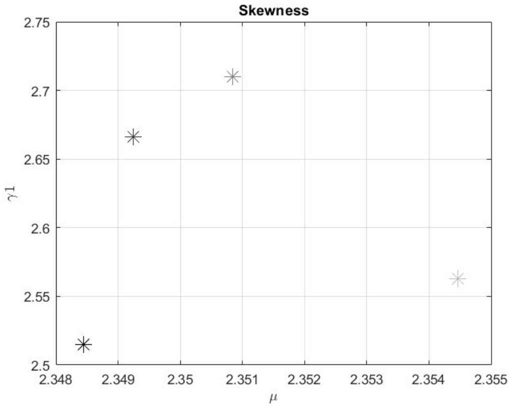

Figure 3.135: Density of protons.

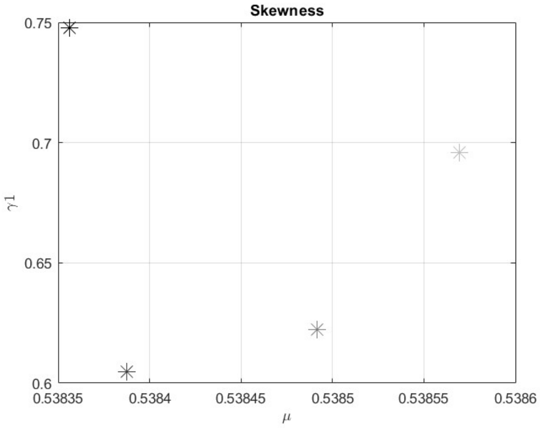

Figure 3.136: Temperature of protons.

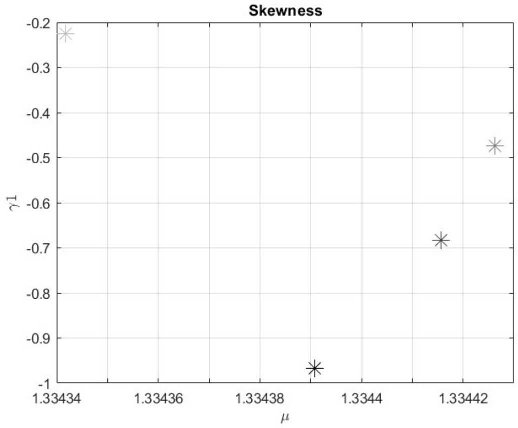

Figure 3.137: Speed of protons.

Same discussion made during double exponential distribution explanation.

- KURTOSIS β_2: The same reasoning applies to the kurtosis index: all indices depend on central moments relative to the overall mean of the data obtained through mediation based on τ. Therefore, not having obtained an effective binning, some indices may be unaffected by the linear trend of other values. In any case, regardless of the position, the decrease in values is confirmed.

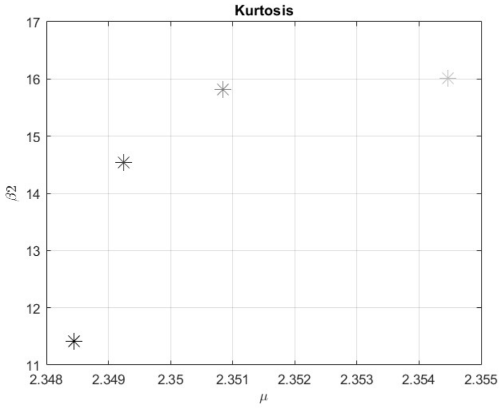

Figure 3.138: Density of protons.

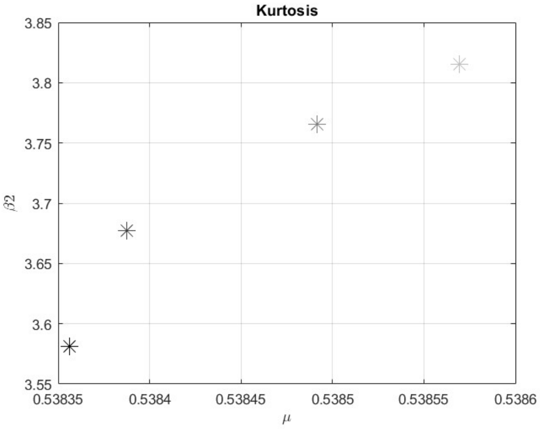

Figure 3.139: Temperature of protons.

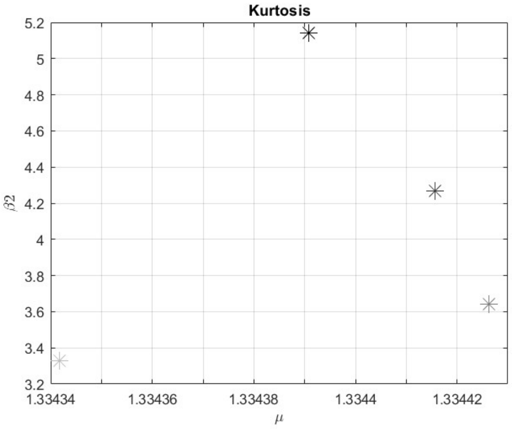

Figure 3.140: Speed of protons.

Extrapolation

According to Fluctuation Theory, to extrapolate data and evaluate projections to future scenarios, concerning where and when Hydrogen Wall (Bow Shock Layer) will be reached, proton density data will be used. As anticipated, complete data is used to make as clear as possible the projection.

By the way, as applied in the previous paragraph, a mean time windows was chosen ($\tau = 15$), in order to evaluate distribution indexes (all aforementioned in the previous section) in all intervals obtained; then, by a linear function interpolation, mean and skewness trends were extrapolated, whereas variance was by a quadratic function.

Given the anticipation that the probes are expected to cease functioning and sending signals to ground stations by 2025, a decision has been made to conduct an assessment of future scenarios until end of 2028, thus necessitating a tripling of the time frame.

The following are the indexes interpolations, even if Kurtosis graph is not again fundamental to extrapolation data: please note, x-axis in all picture are the number of intervals.

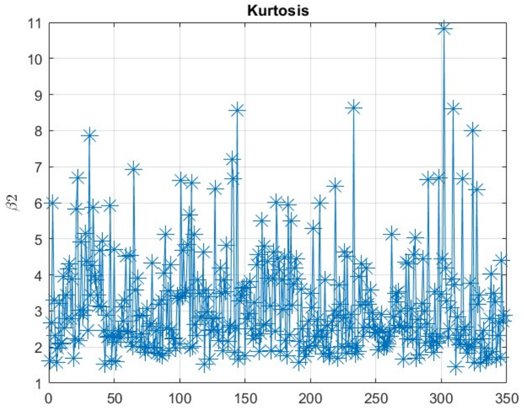

Figure 3.141: Kurtosis indexes at $\tau = 15$.

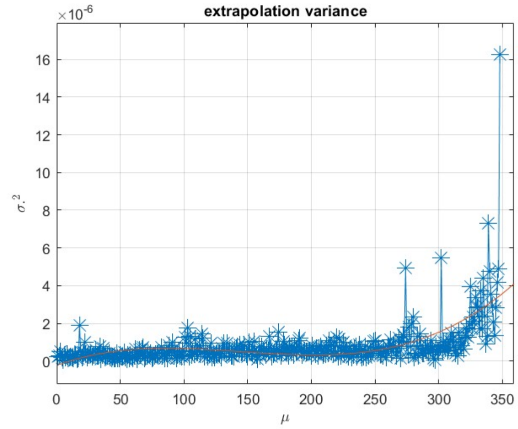

Figure 3.142: Variance indexes at $\tau = 15$.

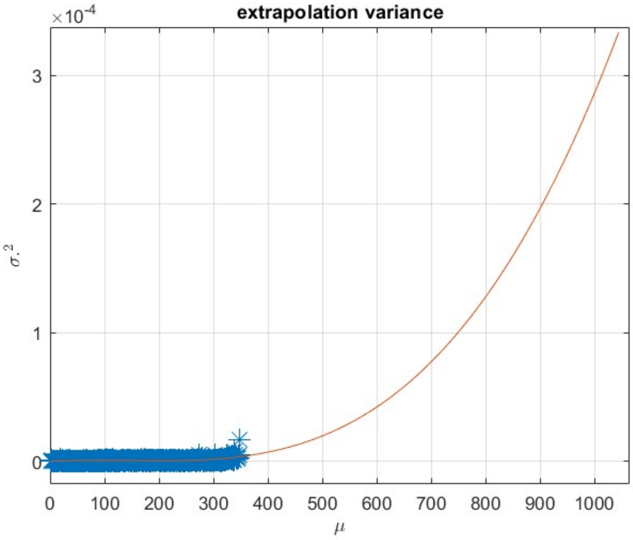

Figure 3.143: Variance extrapolated.

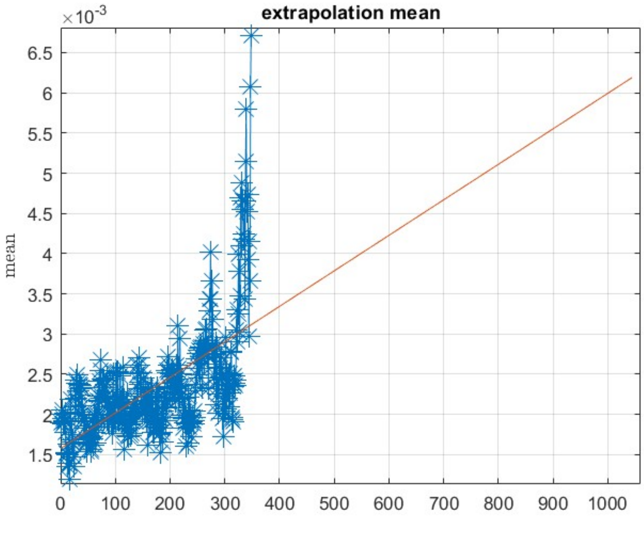

Figure 3.144: Mean extrapolated.

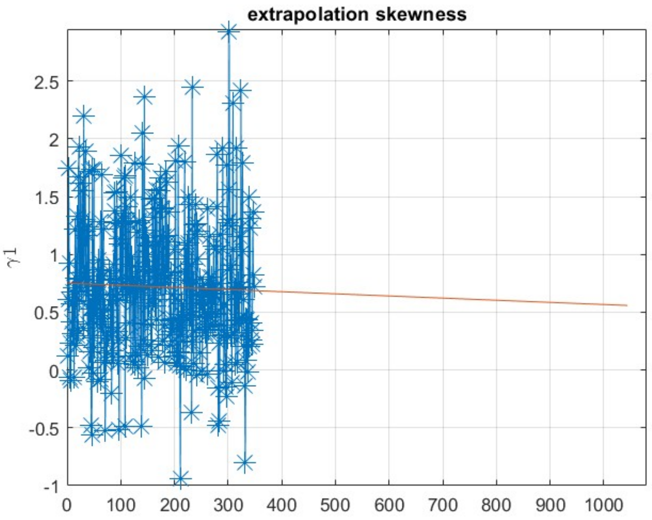

Figure 3.145: Skewness extrapolated.

Subsequently, once shape λ and symmetry κ factor are specified, according to projected mean values and related mode, asymmetric double exponential distribution is obtained and plotted as below:

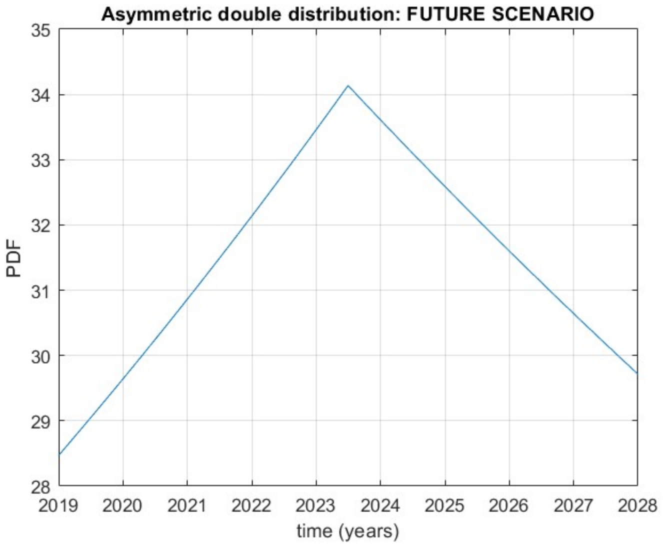

Figure 3.146: Double exponential distribution extrapolated.

According to the obtained graph, there is a doubling of the proton density modulus over a span of 9 years. Certainly, the increase is significantly higher than what has been calculated. The proton sensors ceased to function precisely during the period when the probe was crossing the last AU to officially enter the interstellar medium. Therefore, there would undoubtedly have been a steeper increase, specifically around 10-15%, as observed in the magnetic field modulus calculated by the Voyager 1 probe. The density would have remained roughly constant for about 8 years (maybe few many more, considering that Voyager 2 is slower than its twin) and would have experienced a 50% jump upon reaching the Bow Shock. Obviously, it is challenging to predict with precision with these limited data, but an initial projection of this kind confirms that the trend of properties, both magnetic field components or proton parameters, undergoes jumps with each encounter of a new layer. Therefore, in conclusion, in just over 10 years from 2019, the probe could encounter the Hydrogen Wall, precisely at the corresponding final time of our extrapolation.

3.5 Elaboration 2

In this second chapter, a new type of processing will be analyzed, based on the study of data anomalies. First of all, it is necessary to understand what anomaly means: in the following analysis, the anomaly data of the magnetic field magnitude will be examined, considering anomaly both as the variation of the data average over each broad interval τ, compared to the overall average of raw data,

$$Anomaly_1 = Mean_{local} - Mean_{global} \tag{3.22}$$

and as the deviation from the local mean within the interval defined by a certain τ, of the data within that interval

$$Anomaly_2 = Mean_{local} - Variable_{interval} \tag{3.23}$$

.

Hypothesis

The two cases of anomaly are interesting because, at the same τ, one expects completely opposite trends and conditions. In the first case (global anomaly), at a low τ, the locally calculated mean is highly dispersed, resulting in a value far from the global mean. Therefore, one expects the probability density functions (PDFs) to be low and wide. On the other hand, for a high τ, the local mean would tend towards the global mean, giving rise to narrow and tall PDFs.

Conversely, in the second case of anomaly, if a low τ is imposed, the local mean will be very similar to the values in the interval (local), thus the dispersion will be very low, and the PDFs will be tall. However, with intervals having a significant number of measurements (high τ), there tends to be a greater deviation from the local mean, resulting in low and scattered PDFs.

For this reason, it is crucial to observe the behavior of variance for any τ with the same bins. The trends in dispersion should be opposite. The analysis will help us understand and confirm what has been hypothesized.

Binning problem

In this case, it is possible to calculate the probability function by imposing binning based on a variable number of bins, with boundaries defined by edges. However, this would often lead to the non-existence of results, so for any τ, a fixed number of bins will be imposed for simplicity.

In the case of evaluating the entire dataset, for Voyager 1, the imposed τ is $= 70$, while for Voyager 2, the imposed τ is $= 75$, since the second probe presents a greater amount of data (even though slight). Meanwhile, in the case of analyzing the trends of the two peaks separately, i.e., in the study of the local mean $Mean_{local}$ and overall mean $Mean_{global}$ difference, the imposed τ for a single peak is set at 30.

The following study was found to be useful due to exhibit data oscillations between global average and local one: both anomaly are mediated on $\tau = [4\ 22\ 30\ 45\ 71\ 100]$.

As an illustrative example, the trends of the probability functions of magnetic field magnitude data are shown in the case where binning is determined by defining edges and in the case where the number of bins is fixed at 30.

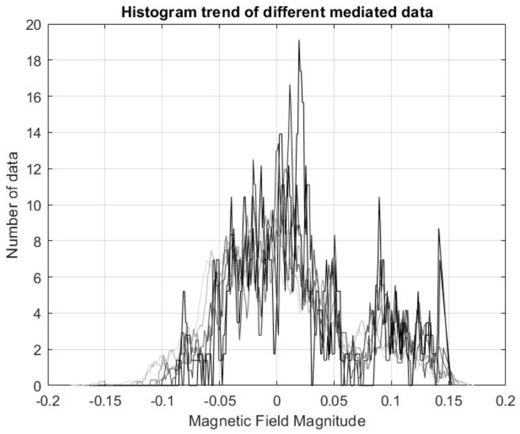

Figure 3.147: PDF trends w/ edge bin setting.

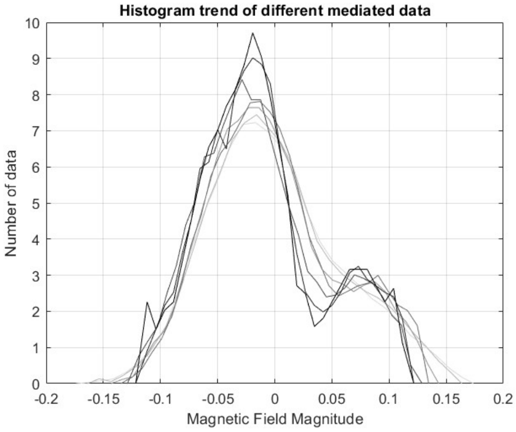

Figure 3.148: PDF trends w/ $\tau = 30$.

In all elaborations lighter curves are referred to $\tau = 4$, whereas darker ones to $\tau = 100$.

3.6 Elaboration 2: Voyager 1

3.6.1 Magnetic field data: global anomaly

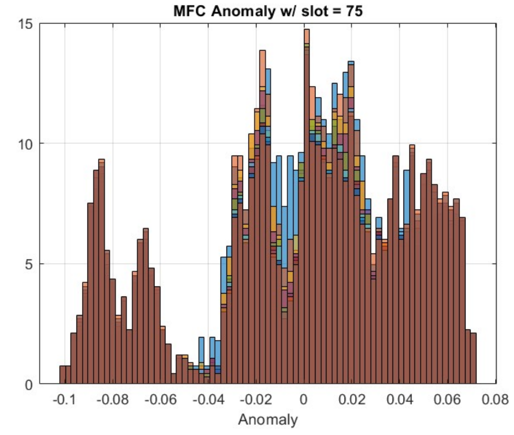

Figure 3.149: Histogram of magnetic field magnitude.

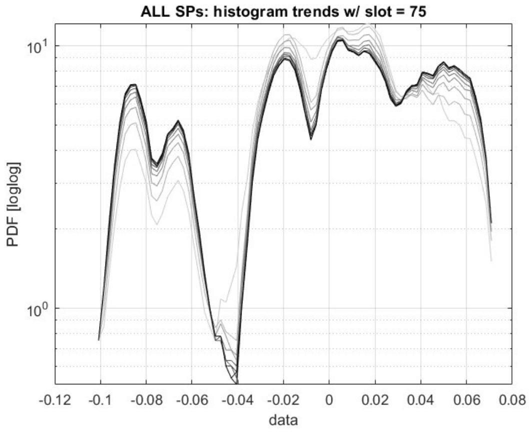

Figure 3.150: PDF of magnitude.

As can be observed from the following trend, it is not clear whether the hypotheses are being fulfilled. With an increase in τ, the dispersion both decreases and increases. In fact, the lighter curves are lower and wider at certain points, while at others, they are narrower. Upon closer observation, the lighter lines consistently remain broader. This implies that at low τ, the curves are highly dispersed and wide. We could say that, albeit in an approximate manner, the hypotheses are respected, as the lines at low τ cover a larger area in any case.

Two peaks are evident, as to variable scaling is useful analyze just the bigger one, that show its values oscillating around zero.

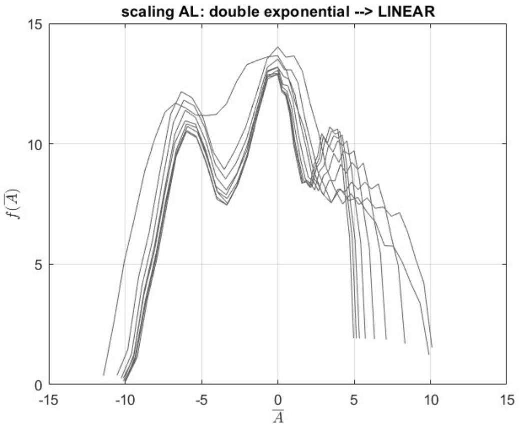

Figure 3.151: Bigger peak: linear scaling.

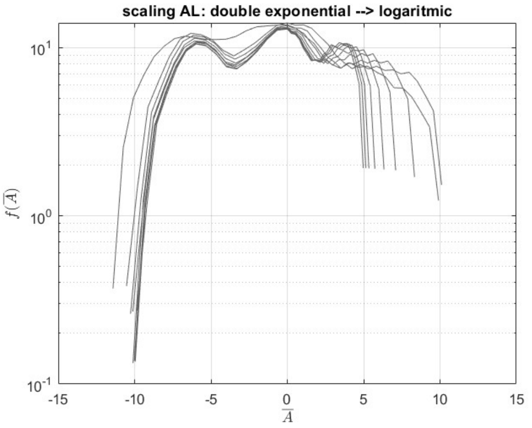

Figure 3.152: Bigger peak: logarithm scaling.

Its oscillating behaviour is all summarized by variance.
Whereas symmetry index strongly depends on which peak is considered: thus, symmetry factor tents to have positive or negative behaviour. This is the only case where variance

doesn't follow the correct path, due to irregular histogram trends, although lighter curve is wider, it's also higher on primary peak, otherwise in the thinner one, the chart exhibits an opposite trend: it brings variance trend to be upside down.

Obviously, if PDF is observed, the answer is clear, as two peaks originated are asymmetric, according to the mode mean data, showed in elaboration 1

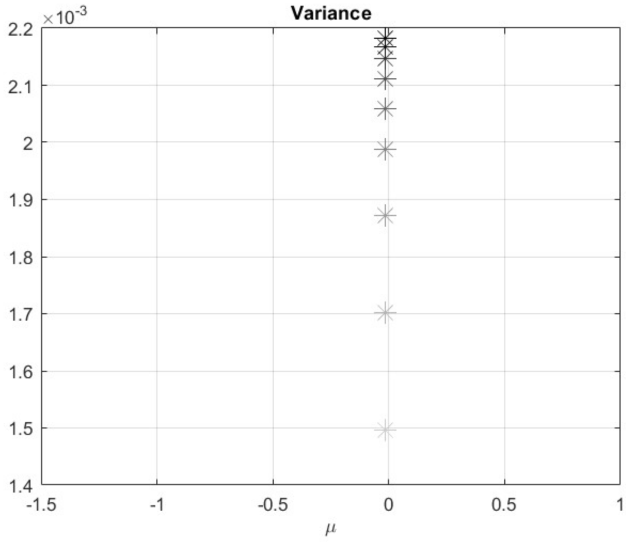

Figure 3.153: Variance at $\tau = 70$.

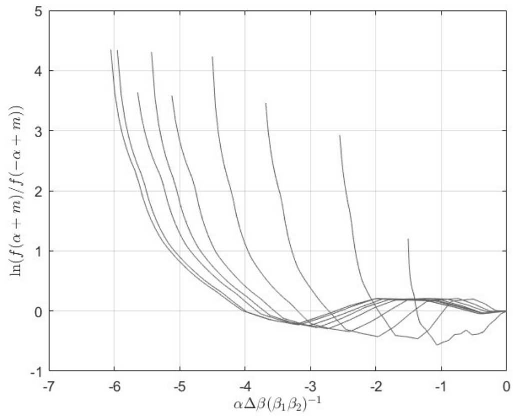

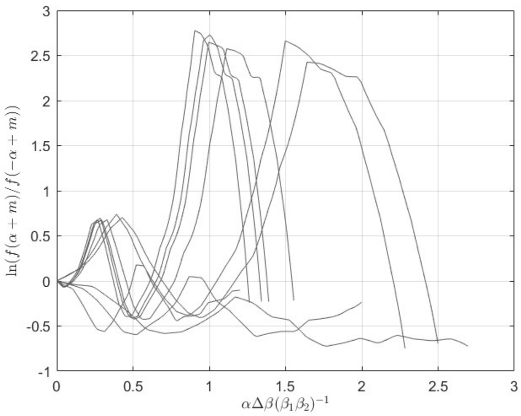

Figure 3.154: Negative symmetry factor.

Figure 3.155: Positive symmetry factor.

Symmetry factor extracted from histogram PDFs need to be distinctly considered. The negative peak origins an exponential decreasing factor, which the higher is τ, the more it is shifted. All curves converge into zero. Otherwise, starting from zero, primary peak provides an oscillating factor, with increasing amplitude.

Global asymmetric double distribution trends, based on scaled dependent variables, presents a quite divergent result. Where existing logarithm ratio is provided, all τ are linked to scratched linear-decreasing chart.

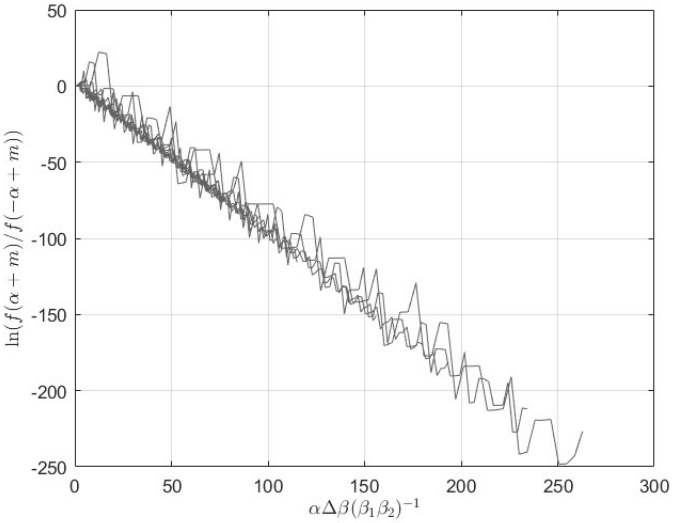

Figure 3.156: Global symmetry factor: ALD based.

3.6.2 Magnetic field data: local anomaly

Local anomaly PDFs quantify how much local measurements tent to their local mean: it's crucial comparing this analysis to the previous one because they exhibits two different properties of same data, thus local mean behaviour related to local system and overall one.

It's expected to be found a bundle of curves that generates just one peak: local mean summarizes all local variables measurements, compared to their trend, while previously, global mean didn't effectively described local variables, indeed it was found to show two different peak, the first related to data intervals that have local mean lower than global one, while the second was related to the ones that have local mean larger than global one.

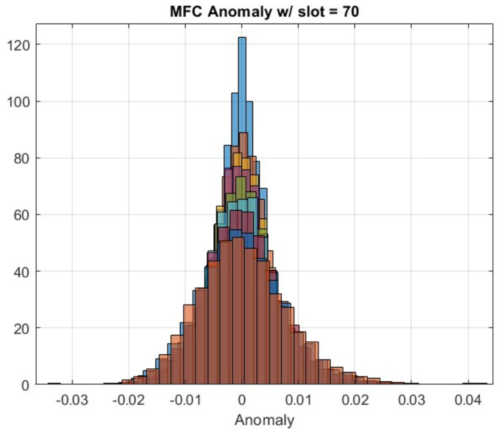

Figure 3.157: Histogram of magnetic field magnitude.

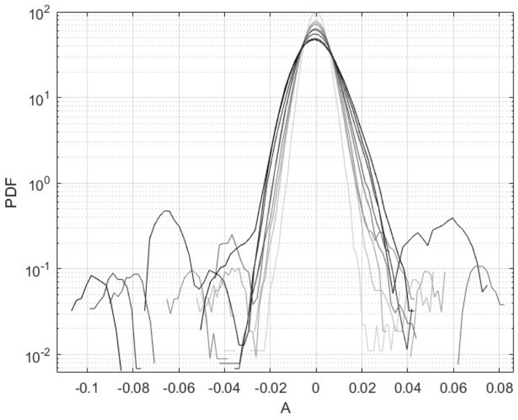

Figure 3.158: PDF of magnitude.

Giving that charts show one peak, PDFs variation is better exhibit: distinct charts present their changes to improve behaviour understanding. In addition, tails linearizing to explicit slopes is easier.

Moreover, overall scaling was applied into the central peak and was found to have a proportional bundle of string.

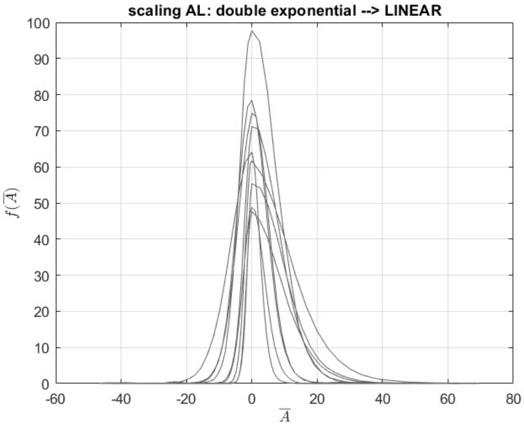

Figure 3.159: Linear scaling.

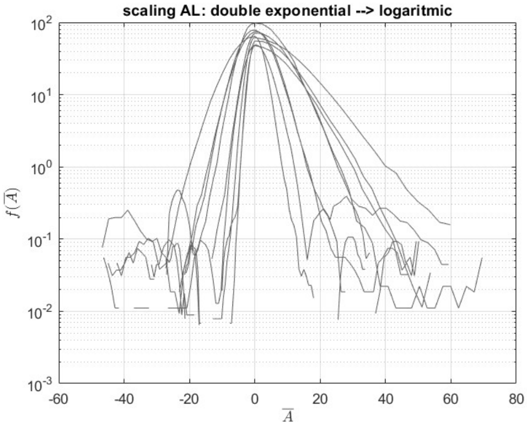

Figure 3.160: Logarithm scaling.

Then, symmetry factors, obtained by both Asymmetric Laplace PDFs and histogram PDFs query intepolation are compared:

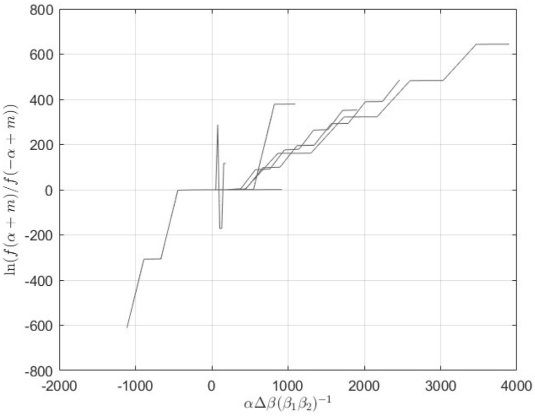

Figure 3.161: Symmetry factor by asymmetric double exponential PDF.

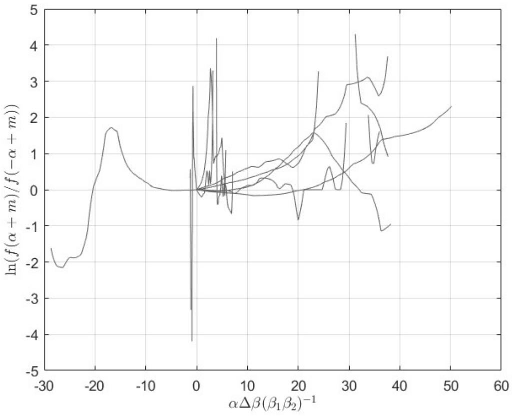

Figure 3.162: Symmetry factor by histogram PDF.

Firstly, increasing factor, described by a step function within a regular trend; the second one also exhibits a quite but more irregular than the previous, increasing factor.

One can be highlight as both factor have positive and negative value, due to PDFs' symmetric tendency. Furthermore, to justify, variance index, computed on overall data and mediated by different factor of τ is suddenly displayed.

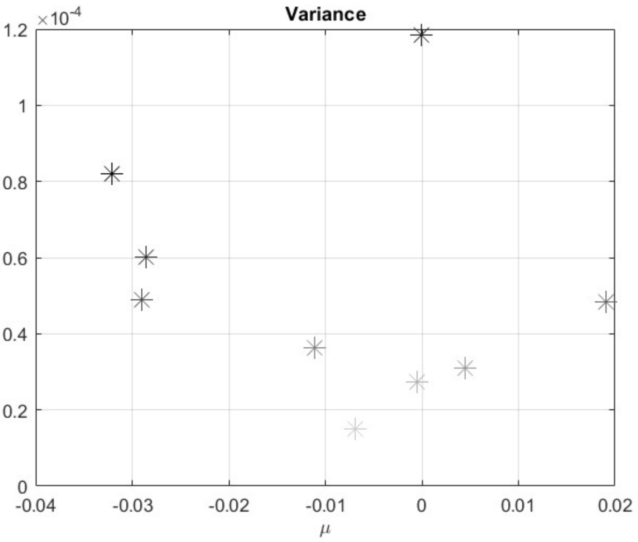

Figure 3.163: Variance at $\tau = 70$.

Variance trend is scattered: beside, as hypothesized, lighter probability function are narrower and higher. That's meanly confirmed by lower variance values linked to assumed conditions.

3.7 Elaboration 2: Voyager 2

Voyager 2 data are more intriguing, as summarize both last Outer Heliosphere layer and very first Interstellar one, therefore let's observe the evolution of global and local averages oscillations.

3.7.1 Magnetic field data: global anomaly

Again, global anomaly should exhibits two big peak, away from the mode, due to the assumption that states that the more the global mean tends to the mode, the more the PDF is symmetric.

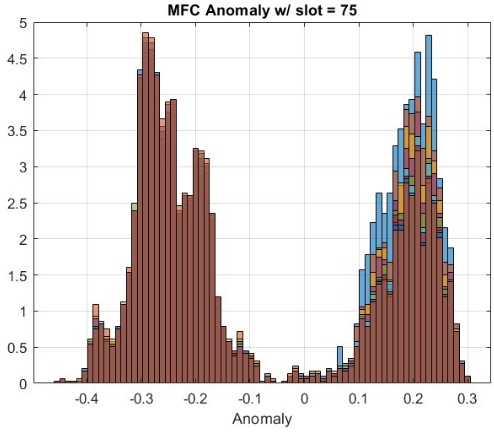

Figure 3.164: Histogram of magnetic field magnitude.

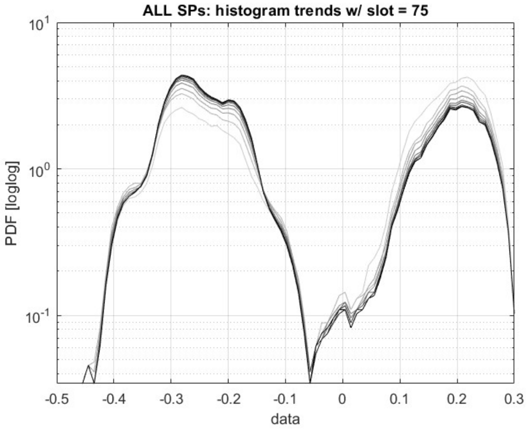

Figure 3.165: Complete PDF of magnitude.

But it is not true, thus, global anomaly will be separately analyzed by imposing $\tau = 35$. We will see how negative peak (values $<$ -0.05) carries out expected PDF and variance, whereas positive one doesn't show clearly this trend.

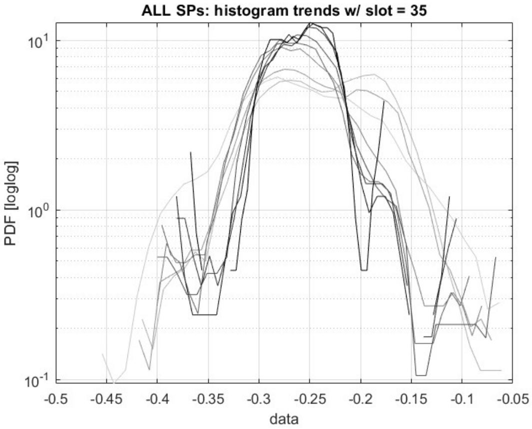

Figure 3.166: Negative peak: logarithmic PDF trend.

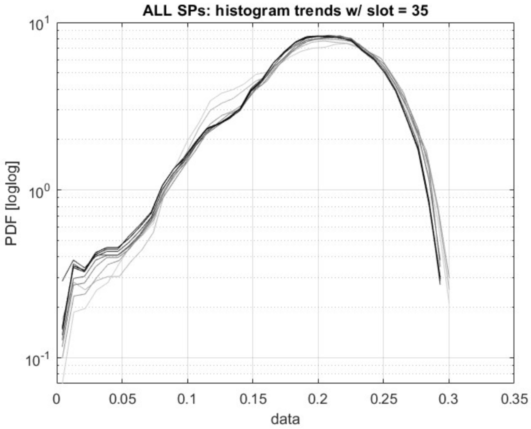

Figure 3.167: Positive peak: logarithmic PDF trend.

As previously assumed, at lower τ, global anomaly decreases, due to interval average being far away from the global mean, whereas at the highest value ($\tau = 35$), the charts steeply proceeds.

Concerning plots shape, positive peak has a denser bundle of string.

Now, both cases linear scaling charts, symmetry factor and variance are displayed and discussed.

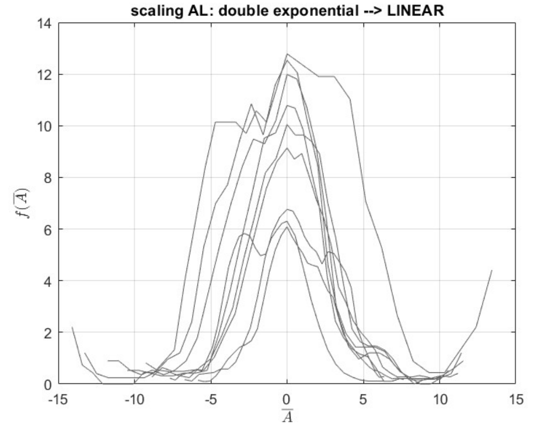

Figure 3.168: Negative peak: linear scaling.

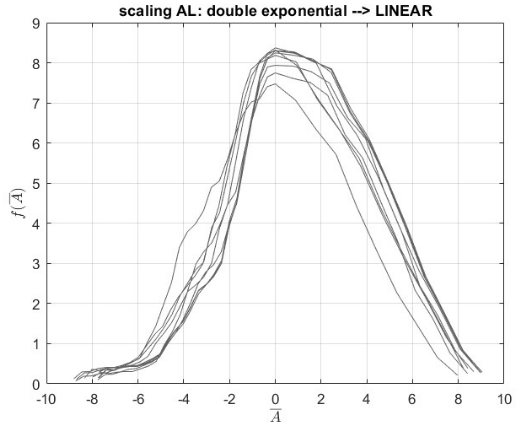

Figure 3.169: Positive peak: linear scaling.

Suddenly, symmetry factor provides more or less linear decreasing trend, obtained by asymmetric double exponential probability function. Denser trends imply less oscillating symmetry factor, as shown:

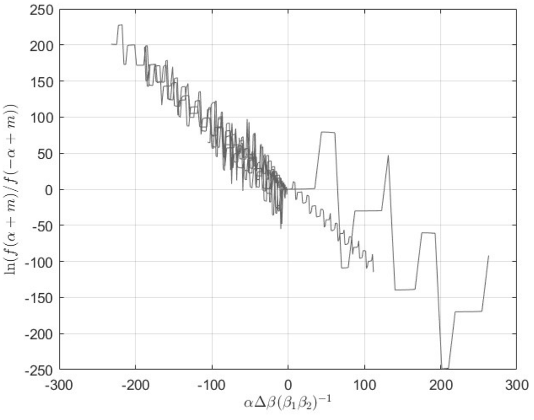

Figure 3.170: Negative peak: ALD symmetry index.

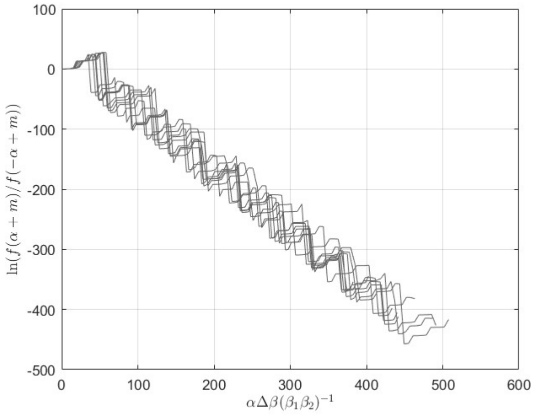

Figure 3.171: Positive peak: ALD symmetry index.

In conclusion, variance index is sparser and more scattered in the first case, while in the second one data are fixer. We will see how second peak oscillating behaviour imply a mean jump; by the way hypothesis are confirmed, despite Voyager 1 global case. In both cases, variance starts with lower values within less dispersion data, linked to higher τ, up to the lightest, linked to 4 $\tau = 4$.

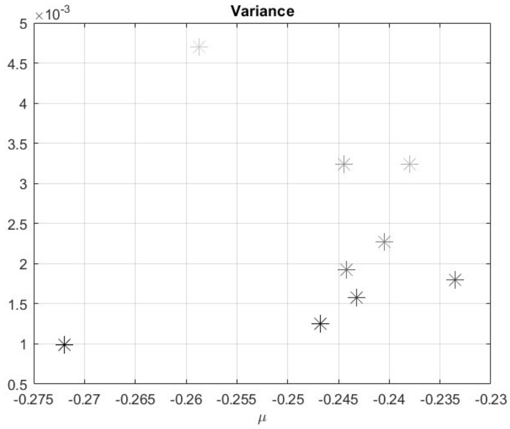

Figure 3.172: Negative peak: variance σ^2.

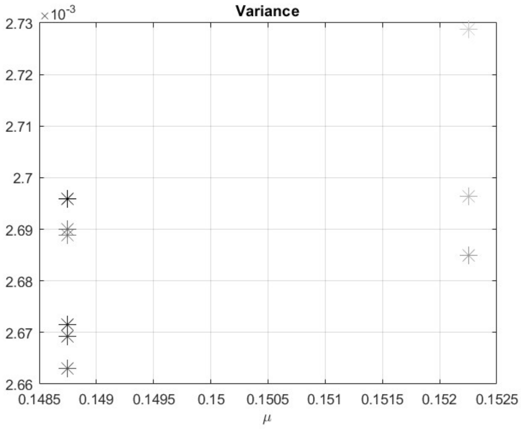

Figure 3.173: Positive peak: variance σ^2.

Globally, variance keeps the same plot, by focusing in the global mean, different from the mode:

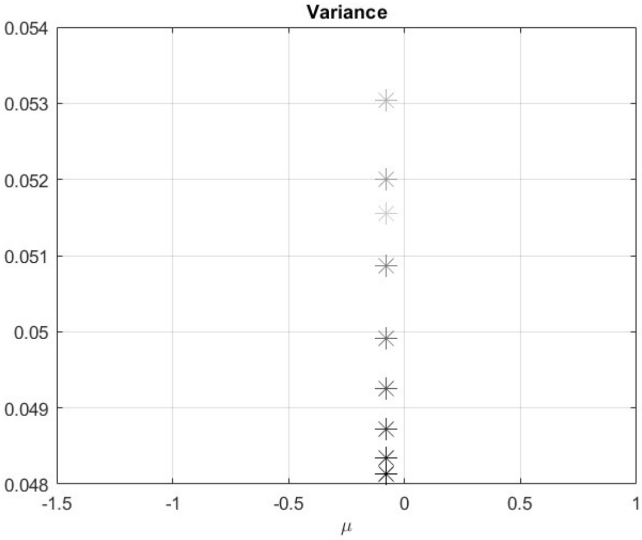

Figure 3.174: Variance at $\tau = 75$.

3.7.2 Magnetic field data: local anomaly

Voyager 2 probe's local anomaly study is the most interesting of all four.

Local anomaly PDFs quantify how much local measurements tent to their local mean: it's crucial comparing this analysis to the previous one because they exhibits two different properties of same data, thus local mean behaviour related to local system and overall one.

There will be shown how PDF trends and variance trends evolve smoothly and how much the analysis fits the hypothesis.

Probability function trends

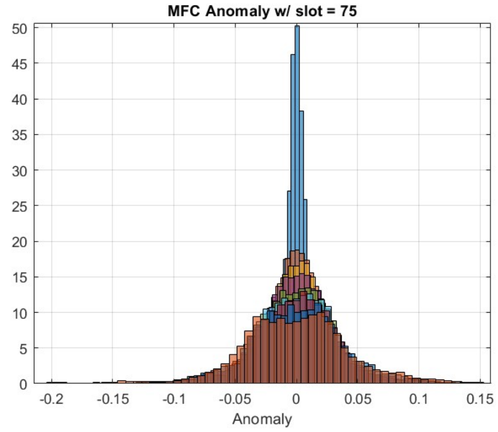

Figure 3.175: Local anomaly histograms.

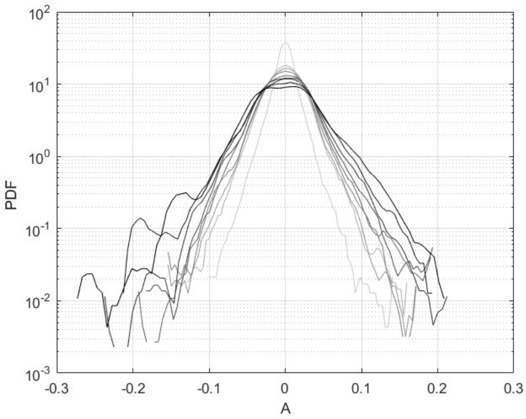

Figure 3.176: Local anomaly PDF trends.

It's already exhibit that $\tau = 4$ curve is narrower, due to its less dispersion: again, it has provided by the tendency of local mean to tent to local measurements, at lower τ.

Scaling trends

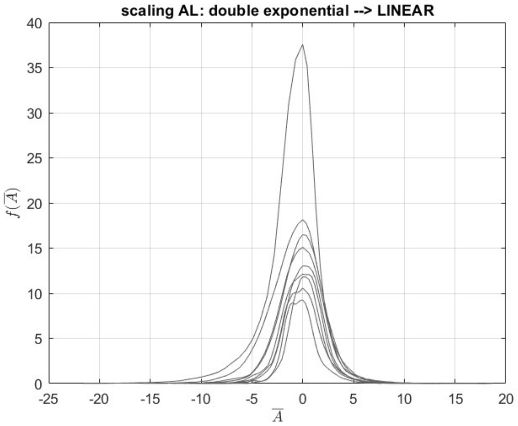

Figure 3.177: Linear scaling PDFs.

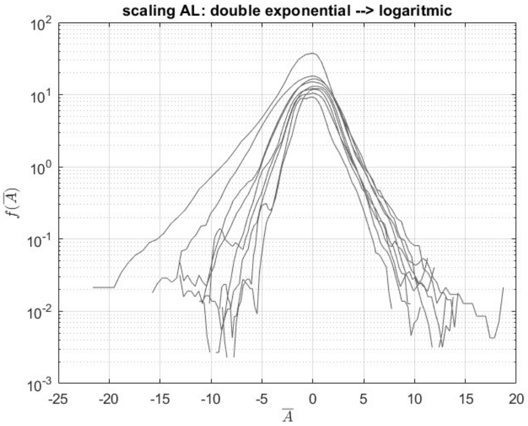

Figure 3.178: Logarithmic scaling PDFs.

The curves are aligned and also proportionally spaced, for the same reason given for the local anomaly evaluated in the case of magnetic field Magnitude of the Voyager 1 probe.

Symmetry factors

According to probability density function symmetry, symmetry factor is also extended from negative up to positive measurements. Essential is the linear decreasing aspect as regard double exponential scaling process.

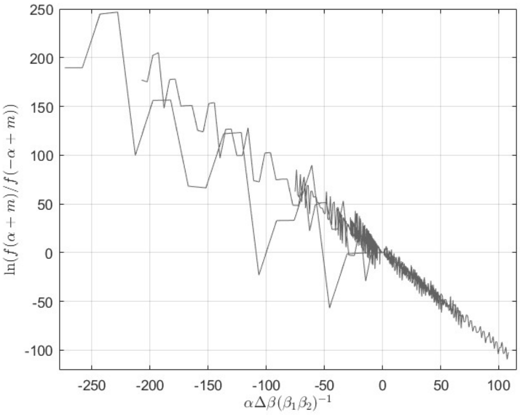

Figure 3.179: Symmetry factor: ALD implementation.

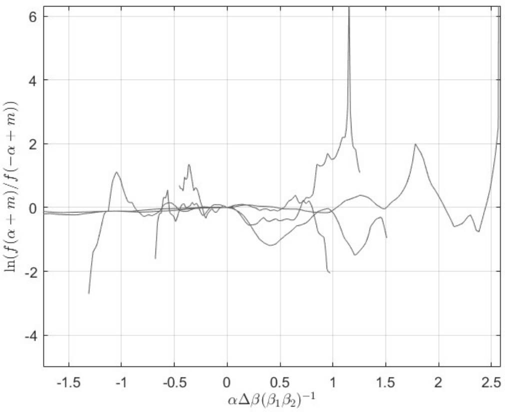

Figure 3.180: Symmetry factor: histogram implementation.

Variance

In conclusion, variance trend is discussed: as previously hypothesized, the variance was expected to behave oppositely to the case of the global anomaly. This has evidently occurred; notably, one can observe a greater harmony in the probability function when considering data of different magnitudes. When comparing pre and post-entry into interstellar space, there is a linear increase in variance, from light to dark asterisks, corresponding to low to high τ values. Crucially, there is an evolution towards consistently lower local means (dark lines correspond to lower μ values). In general, the magnetic field magnitude intensifies significantly between the Outer Heliosphere and the beginning of the Interstellar Medium. However, local variations in the data are much lower compared to within the solar system. Cosmic rays, as energy carriers, are likely deflected by something else, or there is a high energy dispersion, resulting in a less oscillating magnetic field and minimal deviation.

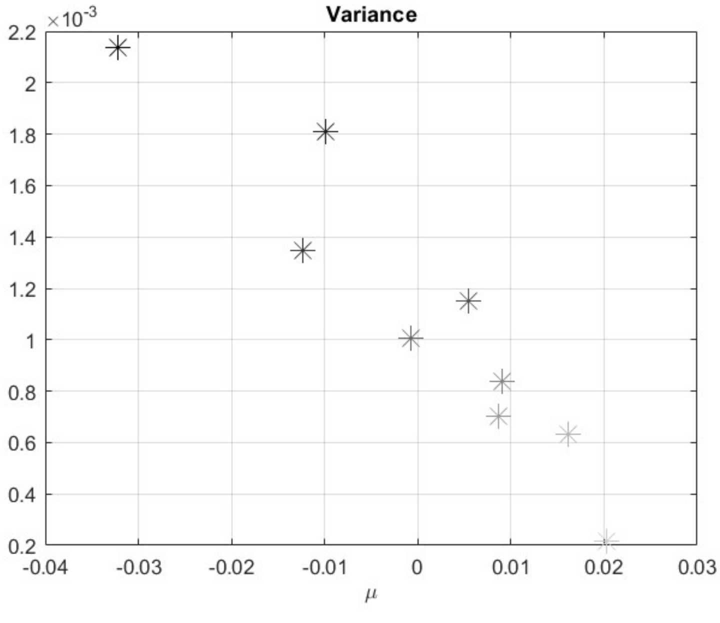

Figure 3.181: Variance at $\tau = 75$.

Chapter 4

Analysis 2 : Fourier Transform

4.1 Introduction

It is interesting to perform a second analysis on the magnetic field data provided by both probes. In this second case, we will use mathematical tools such as the Fourier transform, Fourier series, and power spectral density to expand the data domain, facilitate its interpretation, and, most importantly, explicit the signal power, both as a function of time instants and as a function of frequencies.

4.1.1 Fourier Series

Fourier discovered that every signal can be expressed as a periodic wave, which exhibits a certain repetitiveness within a given period T (hence, it is defined as periodic). However, the harmonic behaviour of the wave is excluded: thus, the wave is indeed periodic, but it does not have a smooth shape with constant and defined amplitude.
Through numerical computations, he concluded that a periodic wave can be written as a linear combination of multiple harmonic waves, which follow the following formula:

$$f(t) = A\cos\omega_0 t + \theta \tag{4.1}$$

Therefore, the Fourier series is a numerical series through which it is possible to write a periodic signal by combining sinusoidal sine and cosine functions. Considering a function of a real variable with complex values, periodicity of 2π, and being square-integrable (or square-sumable within a certain interval, meaning the integral of the square of its modulus over the interval is finite). Then, analysis and synthesis formulas are respectively defined:

$$F_n = \frac{1}{2\pi}\int_{-\pi}^{\pi} f(x)e^{-inx}dx \tag{4.2}$$

$$f(x) = \sum_{n=-\infty}^{\infty} F_n e^{inx} \tag{4.3}$$

If f(x) is a real value function, it's useful applying mathematical identity $\exp inx = \cos nx + i\sin nx$ to chart equally f(x) as a both cos(nx) and sin(nx) function.

This leads to the rectangular shape formulation of the Fourier series in terms of the period T:

$$f(x) = \frac{a_0}{2} + \sum_{n=1}^{\infty} \left[a_n \cos\left(\frac{2\pi n}{T}x\right) + b_n \sin\left(\frac{2\pi n}{T}x\right) \right] \tag{4.4}$$

Please note that even functions are composed only by cosine, whereas odd functions are composed by sine.

Where the coefficients of the function have the following expressions:

$$a_0 = \frac{2}{T} \int_{\frac{-T}{2}}^{\frac{T}{2}} f(x)dt \tag{4.5}$$

$$a_n = \frac{2}{T} \int_{\frac{-T}{2}}^{\frac{T}{2}} f(x) \cos\left(\frac{2\pi n}{T}x\right) dt \tag{4.6}$$

$$b_n = \frac{2}{T} \int_{\frac{-T}{2}}^{\frac{T}{2}} f(x) \sin\left(\frac{2\pi n}{T}x\right) dt \tag{4.7}$$

In particular, a_0 represents the average amplitude of the combined sinusoids, while a_n and b_n represent the weights of the cosine and sine functions, respectively.

In our specific case, the Fourier series of the 8th order is applied, which has the following formulation:

$$f(x) = a_0 + \sum_{n=1}^{8} a_k \cos(k\omega x) + b_k \sin(k\omega x) \tag{4.8}$$

4.1.2 Fourier Transform

Since the Fourier series allows interpreting the signal as a combination of harmonic sine and cosine functions, each with its own frequency (and period being $f = \frac{1}{T}$) and amplitude, the mathematical tool known as the Fourier Transform enables the extraction of the frequency content of these sinusoids. It is useful for transitioning from the time domain to the frequency domain and vice-versa, using the inverse Fourier Transform when transitioning from the frequency domain to the time domain.

Essentially, the complete frequency domain characteristic of the original function f(x) is explicitly represented on the x-axis. This includes every frequency of each individual sinusoid that makes up the initial function. Through the Discrete Fourier Transform DFT (FFT algorithm on MATLab, in our case), the intensities (amplitude) of the sinusoids, associated with a given frequency, can be calculated.

However, in this analysis, we will implement the Fourier Transform both considering the raw data and considering the data processed through the Fourier Series. We will observe how distinguishing individual frequencies in raw data will be challenging, as they appear convoluted. On the other hand, the processing through the series allows for a more organized and periodic form of the data, even though inherently containing errors in the numbers and not precisely representing the truth.

The analysis will focus on examining the data related to the magnitude of the magnetic field, as it is more representative than the three components, hence for convenience, the graphs of the magnetic field magnitude are presented as a function of the number of time steps.

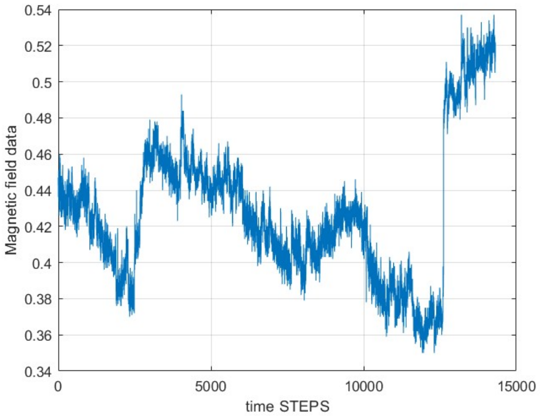

Figure 4.1: Voyager 1: magnetic field magnitude.

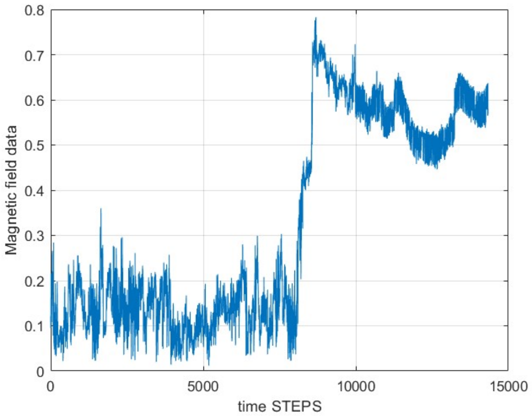

Figure 4.2: Voyager 2: magnetic field magnitude.

4.2 Voyager 1

4.2.1 Fourier Series

Let's begin by processing the raw data through the Fourier Series of the 8th order. This yields a series of harmonics with several amplitude and frequency, oscillating around the mean value of 0.4276 nT, as depicted in the figure:

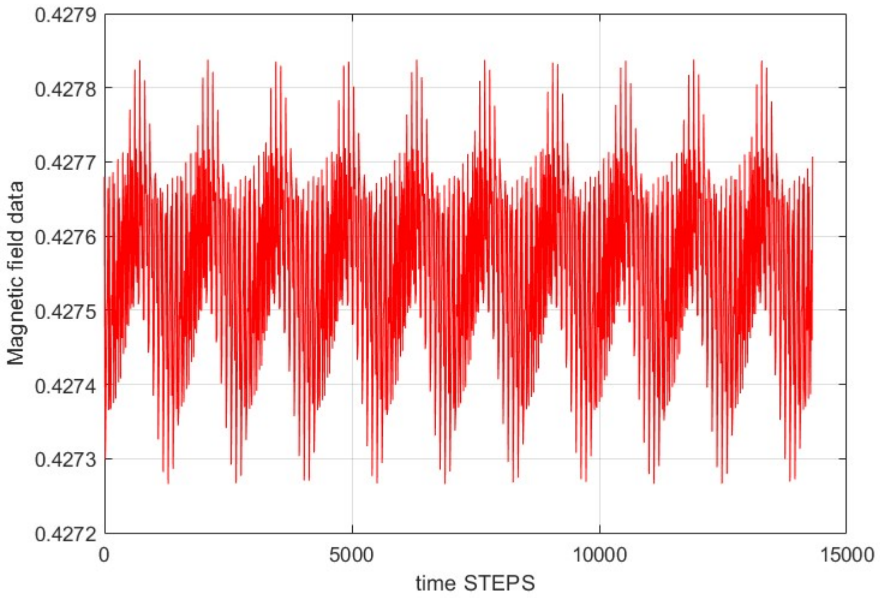

Figure 4.3: Fourier Series expanded.

Then, the fractional portions of the function for 1 period and $\frac{1}{16}$ of the period are plotted to better observe the behavior of the oscillating functions.

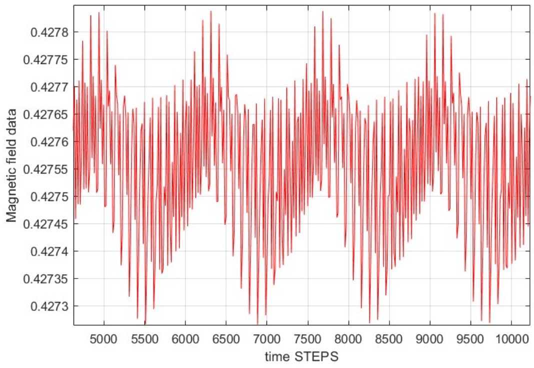

Figure 4.4: Fourier Series: 1 T.

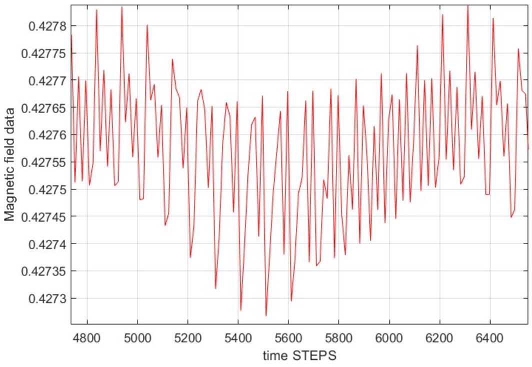

Figure 4.5: Fourier Series: $\frac{1}{16}$ T.

FFT

Successively, the function of real values over time is inputted into the FFT algorithm on the numerical computing software, in order to obtain the transform and perform an assessment of power and intensity. This allows for the discovery of the frequency at which signals travel in the interstellar medium and quantifies how much energy is being carried. The algorithm reduces the frequency by relating it to the period of the sinusoids themselves, so the graphs we obtain will be predominantly spread across a frequency range from 0 to 1 when observing the output transform, and within a frequency interval of -0.5 to +0.5 when observing the translated and centered transform.

The software reports the magnitude of the wave intensity at a given frequency; however, for accuracy, the complete transform is also provided to observe how the waves evolve. A positive or negative magnitude is, of course, related to the reciprocal phasing of the wave, a matter confirmed later by the phase diagram of the transform.

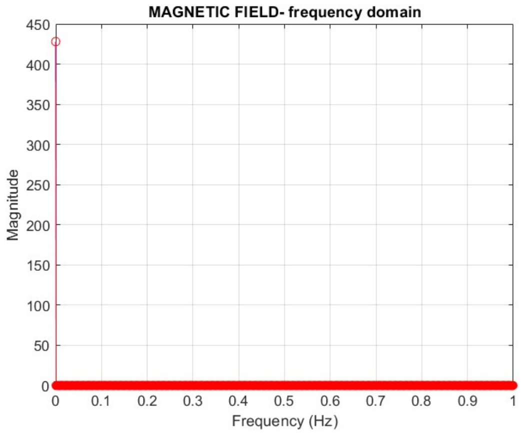

Figure 4.6: Magnitude of Fourier Transform.

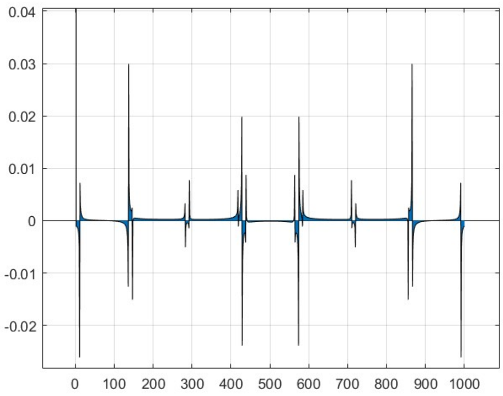

Figure 4.7: Fourier Transform complete.

It is evident that for zero frequency, there is a predominant intensity compared to higher frequencies: this means that the fraction of data that generates a wave at zero frequency, hence with an almost constant straight-line shape, is significantly more substantial and intense. This particular group of functions has such high amplitude compared to the scale represented by the Fourier Series graph that it is not even representable on the same graph. However, as just emphasized, the concept is well illustrated in the FFT graph.

Let's focus then on the arrangement and periodicity of the peaks of the higher-frequency waves:

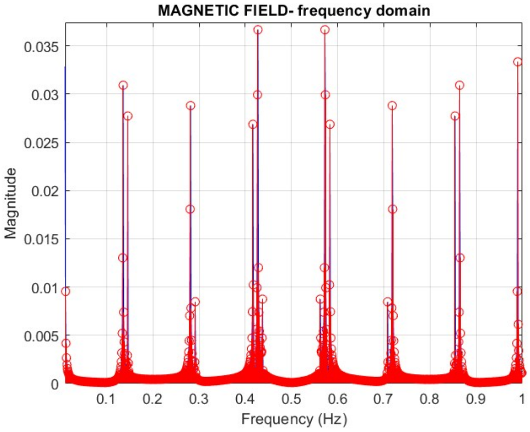

Figure 4.8: FFT of the higher-frequency waves.

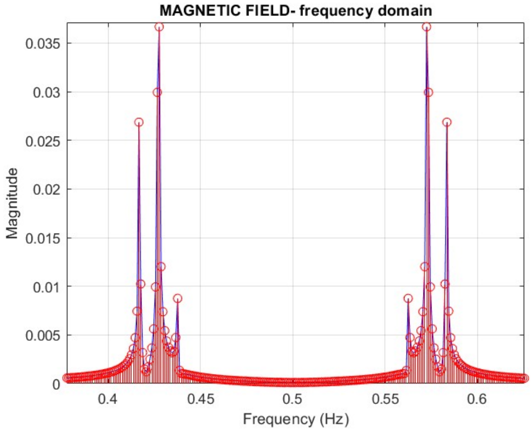

Figure 4.9: FFT of the central and higher-frequency waves.

There is observed repetitiveness of intensities around defined and central frequency values. As seen in the Fourier Series graph, there are multiple periodic primary waves with slight disorderly variations in amplitude near the peaks. The FFT graph indicates the frequencies of these primary waves, for example, approximately f = [0.146 0.281 0.423 0.569 0.71 0.855 0.999], with a periodicity factor of around 0.14, which is roughly the overall amplitude of the range of raw magnetic field magnitude data. The surrounding peaks have frequencies very close to the main ones, making them easily summable, with only the shape (and values) of the amplitude varying.

Relating to the frequency f = 0.5 Hz, the harmonic waves behave oppositely; the peaks are specular, a phenomenon confirmed by the periodicity of the Fourier series function itself. Since the graph and the data are normalized over the period, only one period is represented here. Therefore, f = 0.5 is the value of half the period where the concavity changes. This phenomenon allows for the same variations in the shape of the periodic wave, both for positive and negative real values.

The same behaviour is performed by shifted FFT function: frequencies range values [-0.5 +0.5] is displayed.

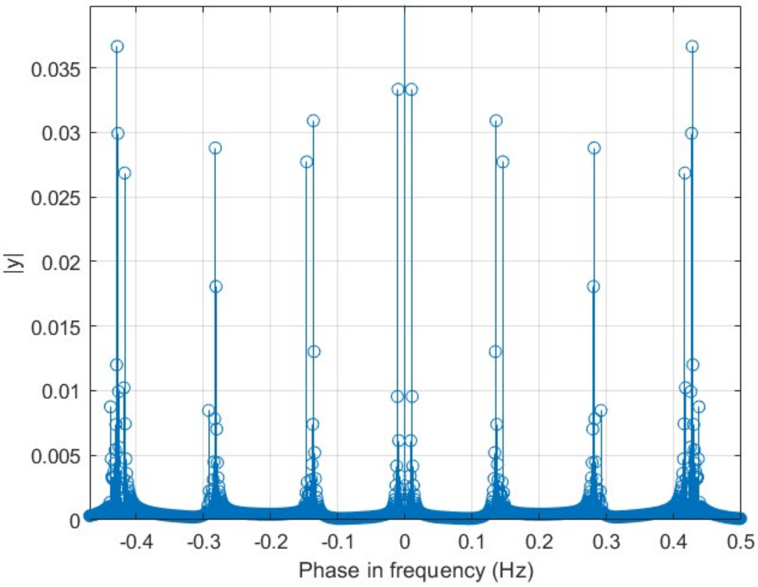

Figure 4.10: Shifted FFT.

Whereas, initial concept linked to positiveness or negativeness FFT magnitude is explained by FFT phase chart. Some harmonic waves are in phase opposition as they reduce the intensity of the overall periodic wave.

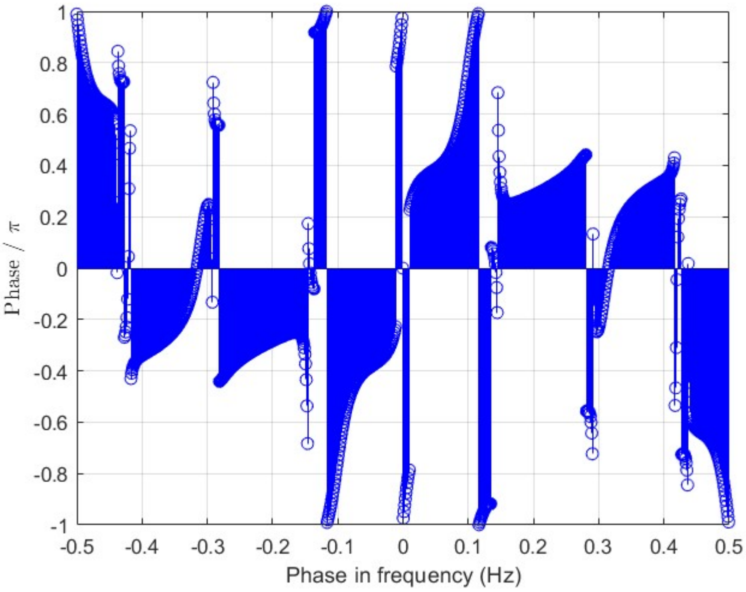

Figure 4.11: Shifted FFT phase.

Power and PSD

Subsequently, a power analysis of the signal is required to observe and quantify the energy carried by both the overall periodic wave and the individual harmonics. In this case, the harmonics are distinct and associated with a specific frequency value, so the power trend should be approximately defined, as shown:

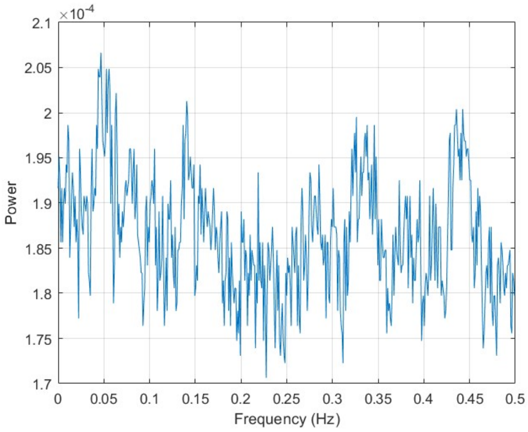

Figure 4.12: FFT harmonic waves power.

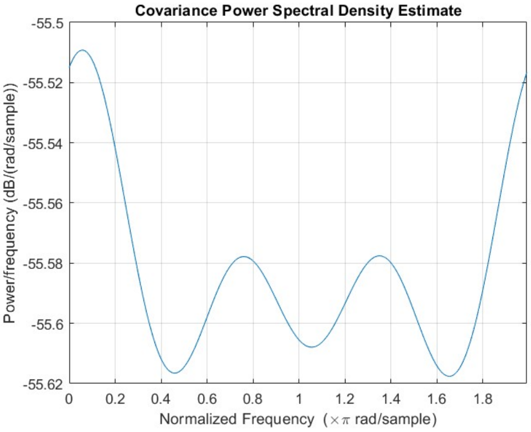

Figure 4.13: FFT Power Spectral Density.

The comparison of this first graph with that of the power spectral density, obtained through the covariance method, is intriguing. The Power Spectral Density (PSD) is a mathematical tool that helps quantify the concentration of power around a spectrum of frequencies. As confirmed by the variance calculated in the previous chapter, there is a decay in the values.

Four main peaks are evident in the power graph, corresponding to the primary frequencies. Similarly, the PSD graph also presents these peaks; however, the two central peaks can be associated with the central maxima of the power function, while the outermost ones are related to the extreme conditions of the frequency range (0 and 1) and are, therefore, simple singularities.

4.2.2 Raw data

. On the contrary, the analysis of raw data is much more complex: it is not possible to distinguish a true group of periodic waves or even harmonic waves that produce a linear combination. The input signals are characterized by very low or even zero frequencies. For this reason, the FFT shows a concentration of intensity for minimal frequency values, while for increasing values, there are slight or negligible intensities. In this case, the graph is also normalized for the period, as evidenced by a certain periodicity for the value of f = 1, where there is symmetric behavior and a concentration of higher values.

FFT

In this case, the intensity associated with zero frequency is approximately 20 times greater, due to the impossibility of reducing the raw data to a periodic waveform, as mentioned earlier. So let's display both the FFT and the full FFT:

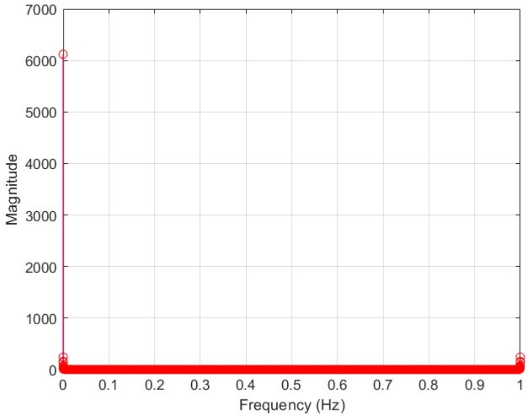

Figure 4.14: Magnitude of Fourier Transform.

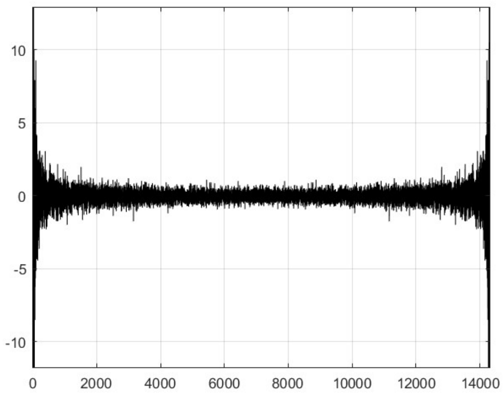

Figure 4.15: Fourier Transform complete.

To confirm what was mentioned earlier, the extreme left, right, and central zones of the FFT in question are also shown:

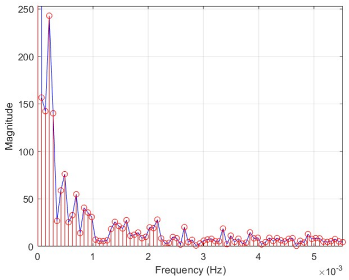

Figure 4.16: FFT: initial frequencies.

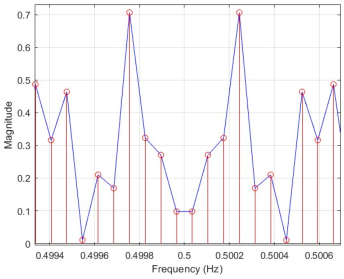

Figure 4.17: FFT central frequencies.

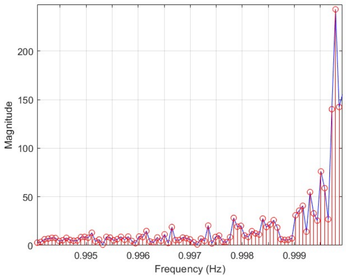

Figure 4.18: FFT ending frequencies.

Again, symmetry conditions are accomplished.

Power and PSD

The power is clearly proportional to the trend of the raw data, albeit of reduced intensity. While the PSD aligns with the distribution of intensity as a function of power, as shown by the FFT graph: there is low power concentration around the central frequencies and maximum (and singular) peaks related to the extreme frequency conditions in the graph.

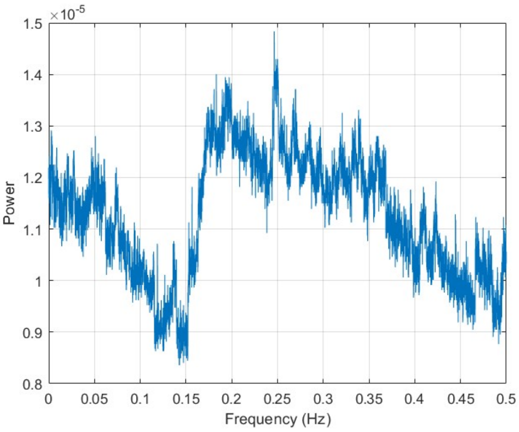

Figure 4.19: FFT power.

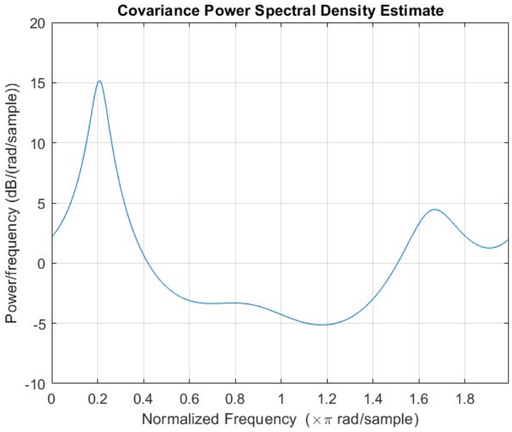

Figure 4.20: FFT power spectral density.

In conclusion, the power and energy concentrations represented by the magnetic field data from the Voyager 1 probe are remarkably stable. They are already related to the interstellar medium, so aside from the final jump related to the Oort Cloud, whose data appears negligible compared to the previous ones in this analysis, there are no excessive variations. It can be asserted that the waves have a constant momentum in this deep-space region, characterized mainly by waves of medium frequency and approximately constant amplitude.

4.3 Voyager 2

In the case of the Voyager 2 probe, the situation is entirely different: the data depicts the spacecraft's transition from the final region of the Outer Heliosphere to the initial region of the Interstellar Medium. For this reason, the data for all magnetic field components initially show approximately constant trends, followed by a jump (both positive and negative), before each stabilizes around a constant range of values.

All components start with an initial value close to zero. In particular, the tangential component (in green) is positive, while the normal component (in black) and the radial component (in blue) are negative. The components progress until reaching a final value that is respectively ten times, four times, and twice the initial value, passing through a point of homogeneity in the magnetic field around January 2017, approximately a year before entering the Very Local Interstellar Medium (VLIM). All final values turn out to be of the opposite sign compared to the initial ones, a situation arising from the inversion of gravitational and magnetic conditions between the final layer of the solar system and interstellar space. As mentioned in the introduction of this thesis, the dominance of the Sun's gravitational force ceases (except for residual influences), and the radiation pressure of cosmic rays and the resulting magnetic magnetization begin to take effect. The rays originate not from the solar system but from deeply cosmic and light-years-distant sources. Therefore, they come from directions that are tendentially transverse, opposite to the outgoing radial direction vector with the Sun as the origin. This leads the sensors on both

Voyager probes to record magnetic field data with extremely high intensity compared to the previous average and with the opposite sign. Linear regression rate explains efficiently the situation (magnetic field magnitude is in pink):

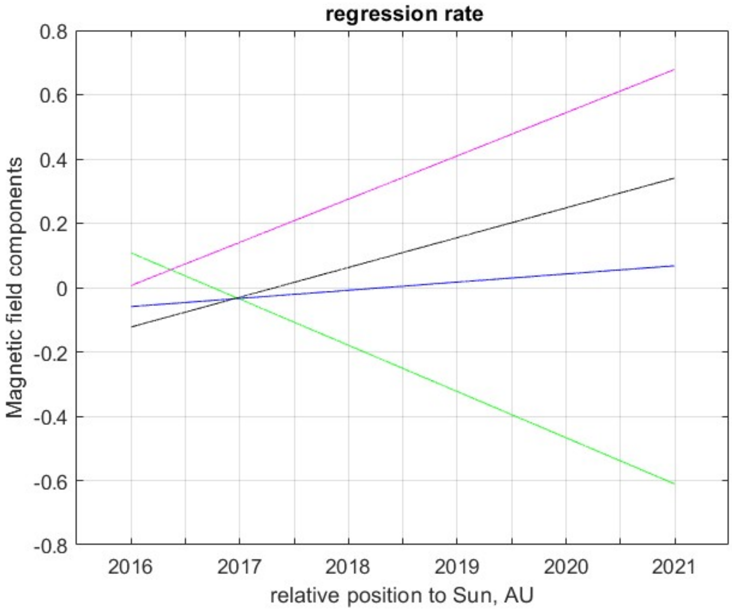

Figure 4.21: Regression rate trends of all magnetic field components and magnitude.

The relevant difference between Outer Heliosphere data and VLIM ones is despicted by proper regression rate charts:

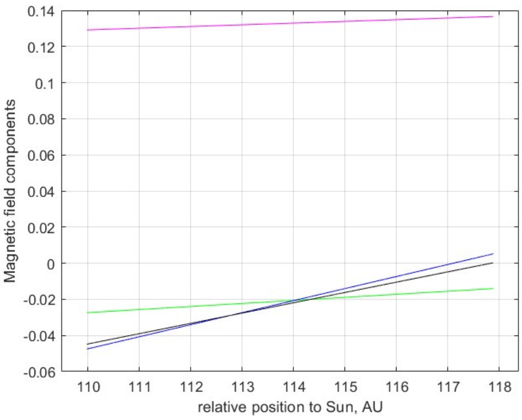

Figure 4.22: Outer Heliosphere data regression rate.

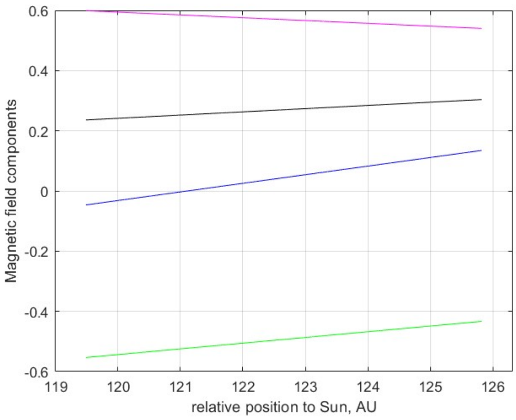

Figure 4.23: Very Local Interstellar Medium data regression rate.

Already by observing the regression lines, it is possible to notice that the data related to the Very Local Interstellar Medium (VLIM) show minor variations, indicating a more uniform trend compared to those related to the solar system. This phenomenon will be useful later for observing the signal power.

4.3.1 Fourier Series

Let's start again by processing the data through an 8th-order Fourier Series: we obtain a periodic wave characterized by various amplitudes and variations, each attributable to a harmonic wave of a certain frequency, as shown in the figure:

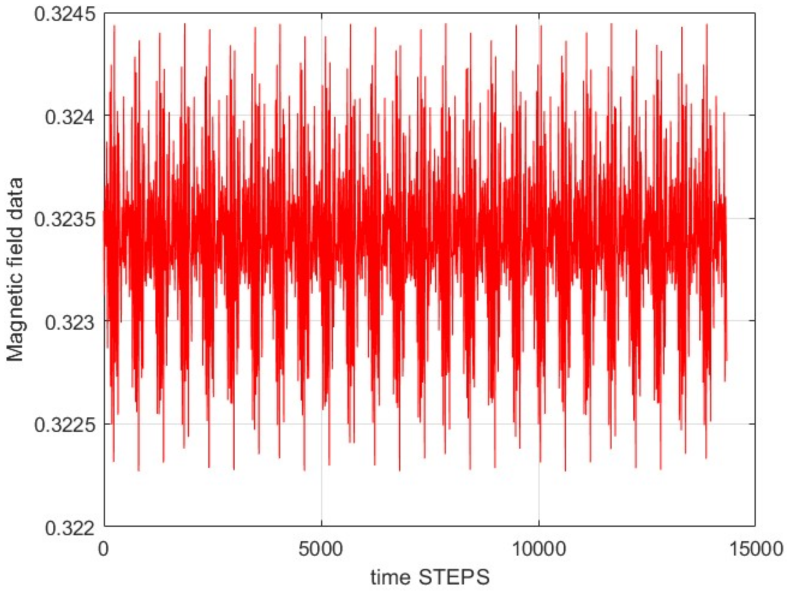

Figure 4.24: Fourier Series expanded.

Then, the fractional portions of the function for 1 period and $\frac{1}{16}$ of the period are plotted to better observe the behavior of the oscillating functions.

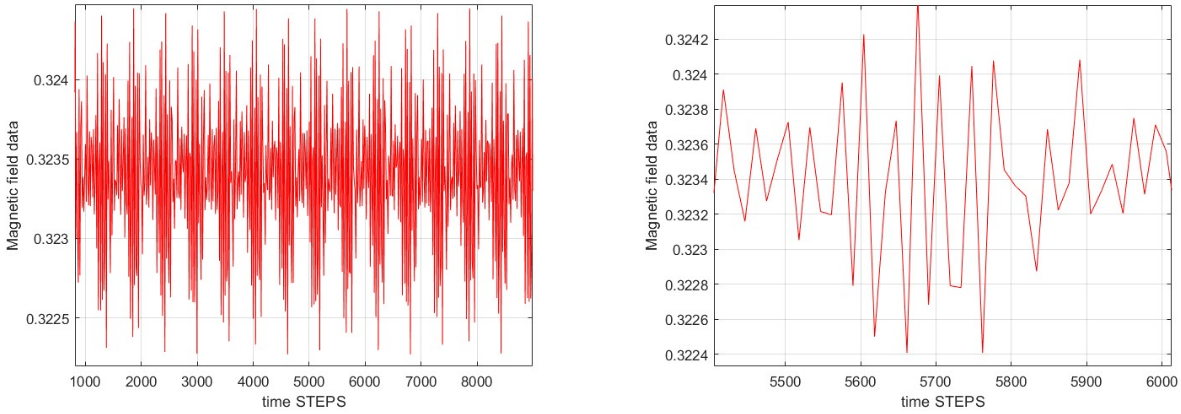

Figure 4.25: Fourier Series: 1 T.

Figure 4.26: Fourier Series: $\frac{1}{16}$ T.

In this particular case, as the dataset is composed of two distinct groups, it is useful to plot an 8th-order Fourier Series for both cases. This helps to explicitly show to what extent the data related to the solar system and the data related to the interstellar medium contribute to the periodic reprocessing and what their relative weights are in the function.

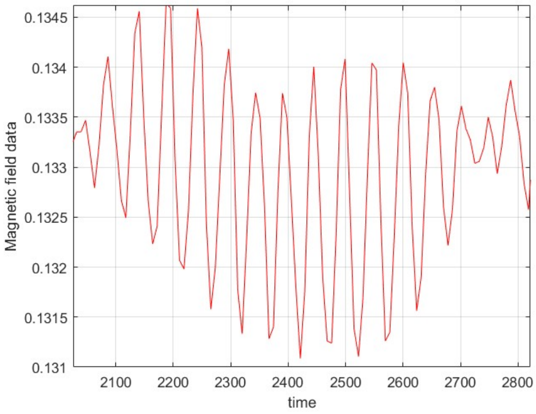

Figure 4.27: Fourier Series: Outer Heliosphere data.

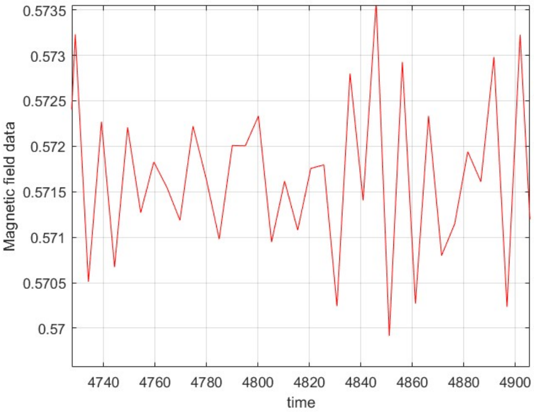

Figure 4.28: Fourier Series: Interstellar Medium data.

The overall Fourier Series oscillates around the value of approximately 0.3234 nT with a maximum amplitude of about 0.002 nT, as shown in Figure 4.26. When considering the Outer Heliosphere data, there is an oscillation around the value of 0.333 nT, with waves that are approximately constant and have a maximum amplitude of 0.003 nT. In the case of the Interstellar Medium, there are alternating oscillations, more or less extensive, around the value of 0.5715 nT, with a maximum amplitude of 0.0035 nT. Therefore, there is a greater amplitude in the Interstellar Medium field, albeit rare. As we will see later, this leads to a higher transported power. However, the constancy of the amplitudes of the waves in the first case has a greater effect on the overall Fourier Series. Consequently, as anticipated, the overall series oscillates around a value of approximately 0.3 but has a similar shape to the Interstellar Medium series. Since it has higher amplitude values, it scales through its proportions into the total series.

A confirming factor that the shape of the overall Fourier Series is attributable to the Interstellar Medium data is related to the instantaneous variation of the data itself:

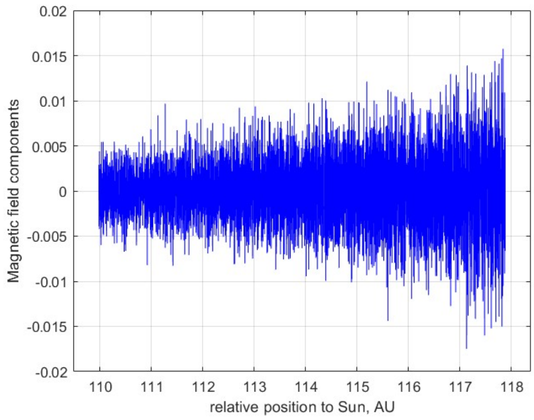

Figure 4.29: Magnitude data variation: Outer Heliosphere.

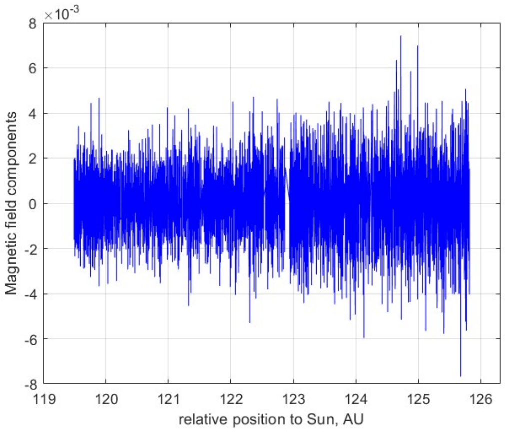

Figure 4.30: Magnitude data variation: Interstellar Medium.

As evident from the two graphs, the variations in the Interstellar Medium data exhibit a constant behavior, unlike those in the case on the left. This implies that the data is more easily representable through a series of stationary harmonic waves, making the Fourier Series produced to describe the Interstellar Medium data more accurate. Moreover, these graphs further confirm the stationarity of the field outside the Heliosphere.

FFT

Successively, the function of real values over time is inputted into the FFT algorithm on the numerical computing software, in order to obtain the transform and perform an assessment of power and intensity. This allows for the discovery of the frequency at which signals travel in the interstellar medium and quantifies how much energy is being carried. The algorithm reduces the frequency by relating it to the period of the sinusoids themselves, so the graphs we obtain will be predominantly spread across a frequency range from 0 to 1 when observing the output transform, and within a frequency interval of -0.5 to +0.5 when observing the translated and centered transform.

The software reports the magnitude of the wave intensity at a given frequency; however, for accuracy, the complete transform is also provided to observe how the waves evolve. A positive or negative magnitude is, of course, related to the reciprocal phasing of the wave, a matter confirmed later by the phase diagram of the transform.

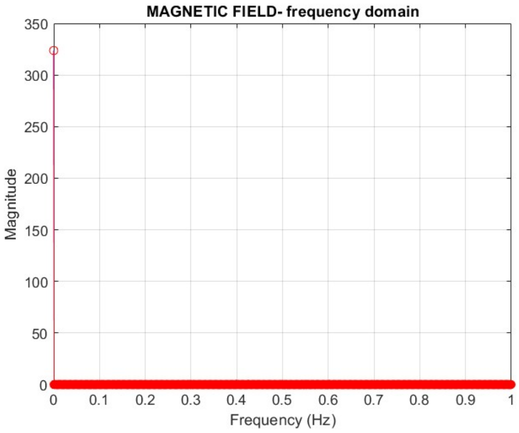

Figure 4.31: Magnitude of Fourier Transform.

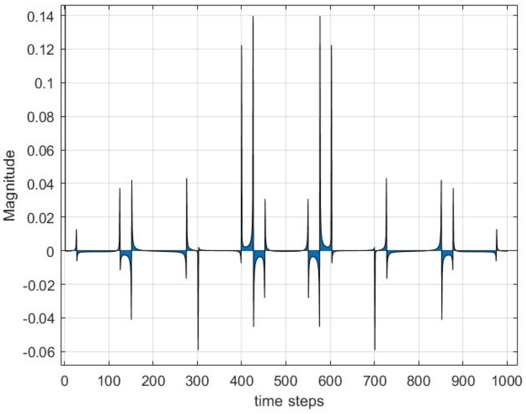

Figure 4.32: Fourier Transform complete.

It is evident that for zero frequency, there is a predominant intensity compared to higher frequencies: this means that the fraction of data that generates a wave at zero frequency, hence with an almost constant straight-line shape, is significantly more substantial and intense. This particular group of functions has such high amplitude compared to the scale represented by the Fourier Series graph that it is not even representable on the same graph. Crucial is to identify maximum intensity of OH or VLIM: despite OH is predominant, it's only 140 points of magnitude, compared to those of VLIM, that are truly higher (close to 600 pt.).

However, as just emphasized, the concept is well illustrated in the FFT graph.

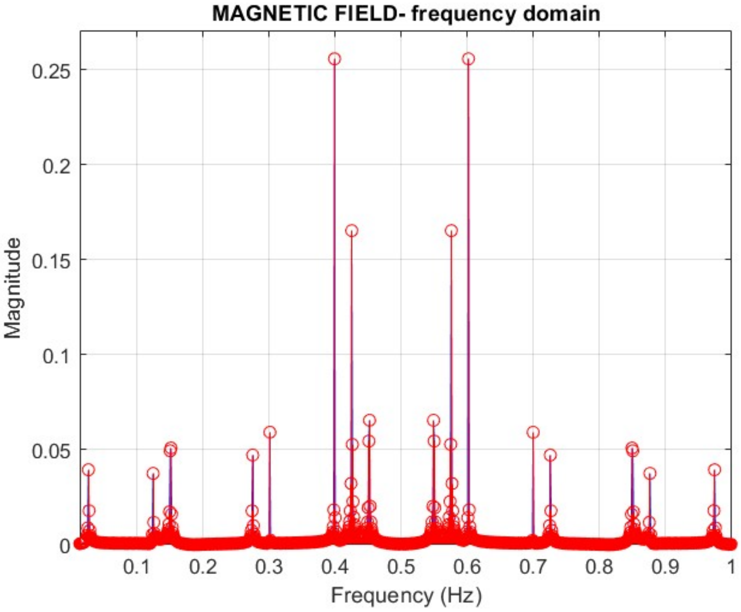

Figure 4.33: FFT of the higher-frequency waves.

Again, according to previous hypothesis, it's also useful pay attention on distinct cases, in order to allow for a better understanding:

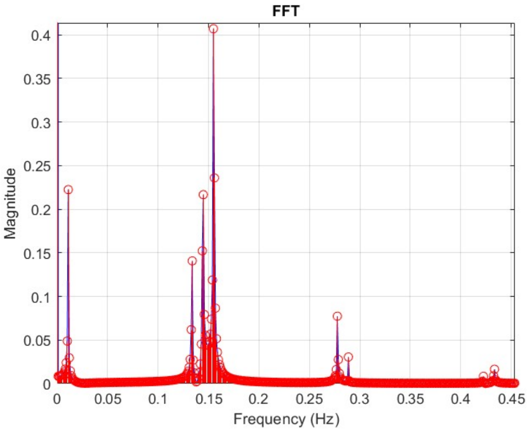

Figure 4.34: FFT of the higher-frequency waves: Outer Heliosphere case.

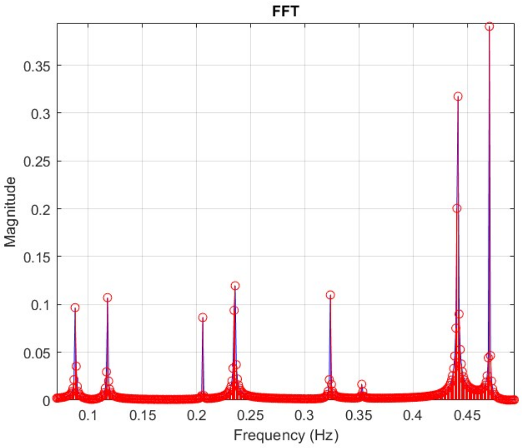

Figure 4.35: FFT of the higher-frequency waves: VLIM case.

Despite the frequencies on the x-axis being normalized for the period, it is evident that the two distinct FFT functions unfold on complementary frequencies. Therefore, the two separate Fourier Series are composed of harmonic waves with completely different frequencies but overall similar magnitudes. Specifically, the higher frequency with higher intensity is related to the Very Local Interstellar Medium (VLIM), a situation also evident in the overall FFT.

In general, the overall Fourier Series is composed of harmonics with frequencies imposed by the Outer Heliosphere data, but the distribution of amplitudes and intensities is attributed to the Interstellar Medium data.

Whereas, initial concept linked to positiveness or negativeness FFT magnitude is explained by FFT phase chart. Some harmonic waves are in phase opposition as they reduce the intensity of the overall periodic wave. For informational purposes, as with the data collected from the Voyager 2 probe, the phase diagram of harmonic waves at different frequencies is shown below:

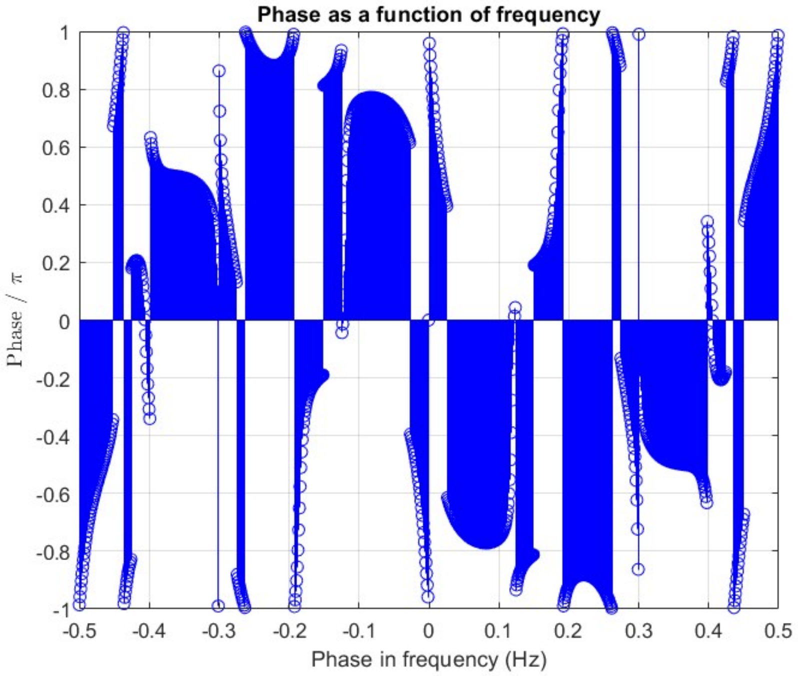

Figure 4.36: Shifted FFT phase.

Power and PSD

Subsequently, a power analysis of the signal is required to observe and quantify the energy carried by both the overall periodic wave and the individual harmonics. In this case, the harmonics are distinct and associated with a specific frequency value, so the power trend should be approximately defined, as shown:

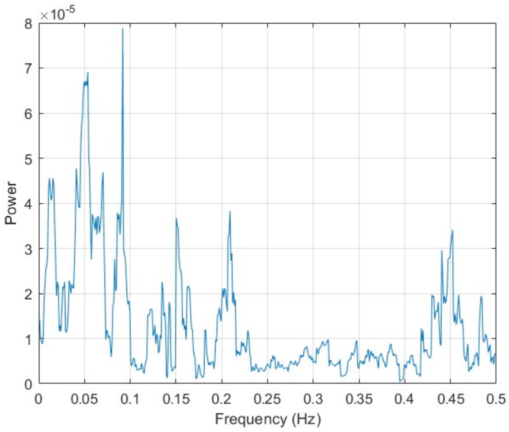

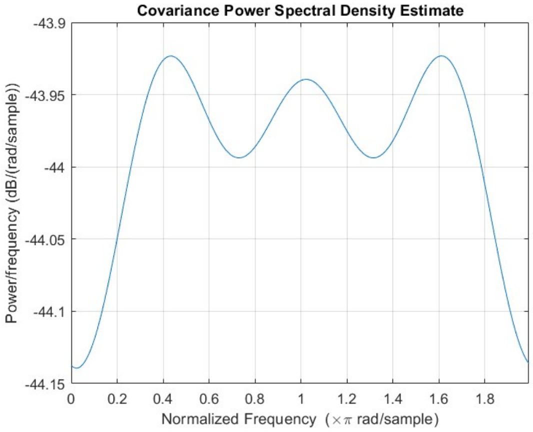

Figure 4.37: FFT harmonic waves power.

Figure 4.38: FFT Power Spectral Density.

The Power Spectral Density (PSD) defines three peaks, but considering the frequency range [0 1], the power trends are confirmed. There is higher transported power for lower frequencies, a situation proportional to the behavior of the FFT of the Outer Heliosphere data, while the intensity decreases with increasing frequency, undergoing a slight increase around f = 0.455 Hz, a frequency with higher intensity for the Interstellar Medium data.

However, as well known, power is proportional to frequency, particularly increasing with frequency. For this reason, the power spectrum of the FFT and the overall Fourier Series could only be the same power spectrum as that of the Outer Heliosphere data, as these data are responsible for the general frequencies. However, as seen earlier, there are harmonic waves with higher intensity and amplitude (and frequencies) in the case of the Interstellar Medium, which generate a more intense power spectrum as a function of frequencies, as shown below:

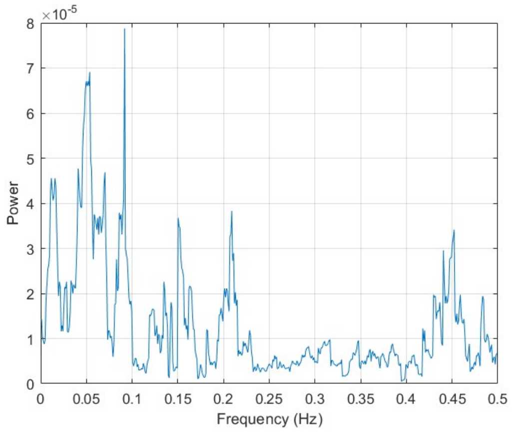

Figure 4.39: Power: Outer Heliosphere case.

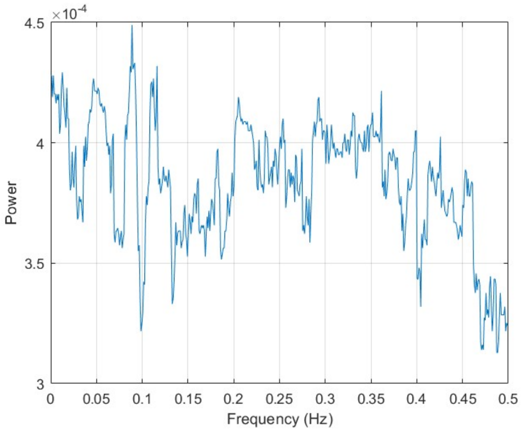

Figure 4.40: Power: Interstellar Medium case.

Due to Galactic Cosmic Rays, the energy carried by the magnetic field waves is intense by more than an order of magnitude: thus, there is a higher order in the vector field, with nearly constant field gradients but characterized by high kinetic energy transported.
The solar gravitational field acts as a shield for these radiations, creating a less harmful environment within the solar system. This is the reason for the accelerated degradation of onboard scientific instruments in recent years, leading to an approximate cessation of their functionality within a couple of years.

4.3.2 Raw data

On the contrary, the analysis of raw data is again much more complex: it is not possible to distinguish a true group of periodic waves or even harmonic waves that produce a linear combination. The input signals are characterized by very low or even zero frequencies. For this reason, the FFT shows a concentration of intensity for minimal frequency values, while for increasing values, there are slight or negligible intensities. In this case, the graph is also normalized for the period, as evidenced by a certain periodicity for the value of f =

1, where there is symmetric behavior and a concentration of higher values.

FFT

In this case, the intensity associated with zero frequency is approximately 20 times greater, due to the impossibility of reducing the raw data to a periodic waveform, as mentioned earlier. So let's display both the FFT and the full FFT:

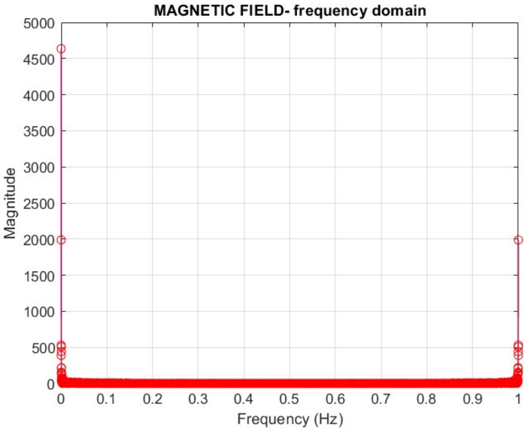

Figure 4.41: Magnitude of Fourier Transform.

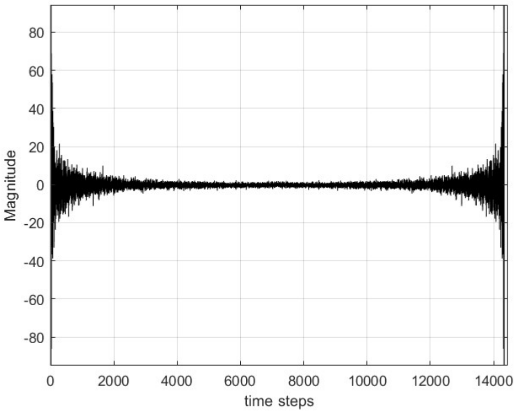

Figure 4.42: Fourier Transform complete.

To confirm what was mentioned earlier, the extreme left, right, and central zones of the FFT in question are also shown:

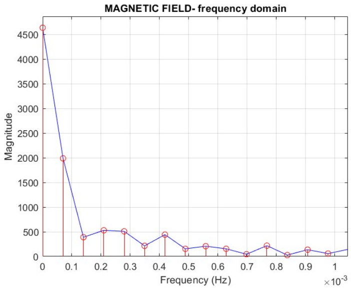

Figure 4.43: FFT: initial frequencies.

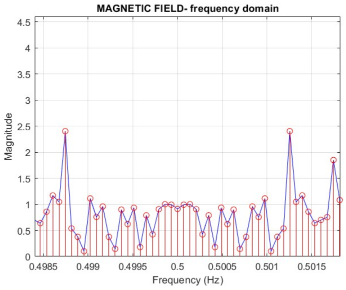

Figure 4.44: FFT central frequencies.

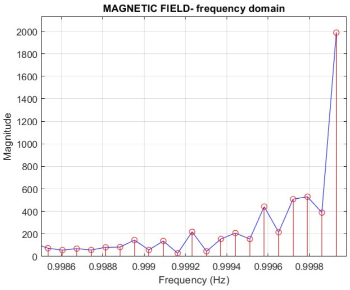

Figure 4.45: FFT ending frequencies.

Again, symmetry conditions are accomplished.

Power and PSD

The power is clearly proportional to the trend of the raw data, albeit of reduced intensity. While the PSD aligns with the distribution of intensity as a function of power, as shown by the FFT graph: there is low power concentration around the central frequencies and maximum (and singular) peaks related to the extreme frequency conditions in the graph.

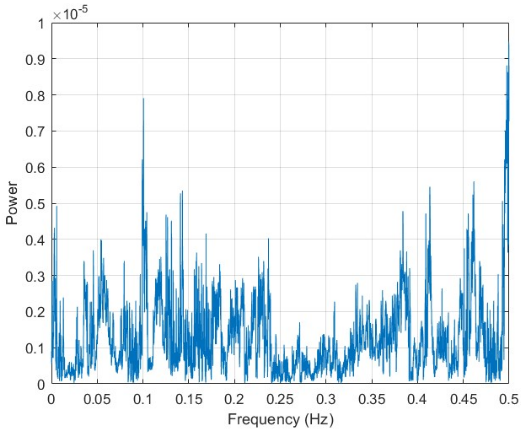

Figure 4.46: FFT power.

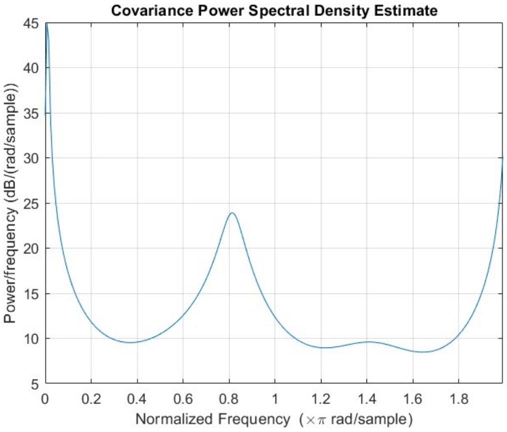

Figure 4.47: FFT power spectral density.

If we observe the two figures, considering a median frequency range, i.e., in the interval [0 1] Hz, it is possible to see that the graph of the Power Spectral Density (PSD) develops two peaks; however, the power graph, despite being jagged due to high alternation and difficult rewriting through harmonic waves, exhibits more than two peak maxima. In particular, the peak corresponding to the frequency f = 0.1 Hz is not a true concentration of power frequencies but a calculation anomaly. To confirm this, one can compare the graph of the evolution of raw magnetic field magnitude data and the processed Fourier Series, where there is no data with a value that generates the reported power.

As in the previous case, the data with greater influence pertains to the Outer Heliosphere. Therefore, the previous graphs have a tendency towards these data and reveal little about the power and power concentration of the Interstellar Medium. In any case, raw data is full of measurement and interpolation errors, preventing an objective analysis, unlike the application of the Fourier Series. For this reason, the more accurate analysis, and one to be taken into consideration, is related to the reprocessing through periodic waves and harmonic combination. The trend outlined by the data, albeit preliminary, still serves as a worthy reference base to identify how and with what intensity the data evolve in an environment external to the solar system.

Chapter 5

Conclusions and future applications

The most critical aspect of space exploration is the study of the space environment, particularly the radiation topic it entails. Since the early days of the Space Race in the early twentieth century, there have been numerous failed or interrupted space missions due to interference caused by abnormal environmental conditions, sometimes leading to catastrophic outcomes.

Through the analyses proposed in this thesis, the goal is to contribute to spatial analysis by providing the opportunity to observe environmental variations from a probabilistic perspective. This stems from the need to compare macroscopic phenomena to approximable microscopic phenomena (note that the magnetic field measurements used are on the order of nanoteslas), thus providing a more robust and effective prediction of the behaviors of the parameters in question. This allows for quantifying both the movement of the solar system and the shape of the clouds extending into the interstellar medium, as well as identifying areas where clusters of particles may cause strong shocks or deviations of solar and stellar winds.

Multiple advantages are related to the study of the space environment, especially in the terminal zones of the solar system but also beyond. Consider the engineering of production processes and the design of future spacecraft in light of the radiation environment. By extrapolating and projecting conditions onto future scenarios, it is possible to improve onboard instruments, scientific tools, and simply electronic and mechanical components (such as attitude control, propulsion, or energy subsystems) effectively implement algorithms for spacecraft control and maneuvering.

With a more elaborate study of Molecular Dynamics, one can examine particle flows and the energy produced/transported. Certain conditions can act as catalysts for specific chemical reactions, so these flows could be exploited for propulsion or other maneuvers.

As for sustainability and global warming, what better way to address the problem than being able to harness energy outside of Earth or the Solar System, considering the high amounts of energy carried by cosmic rays? In the future, a combination of quantum mechanics and molecular dynamics could lead to the capture, transport, and use of this source as an infinite energy source.

A more tangible aspect not to be underestimated concerns the reproduction of the space environment on Earth: several studies have already confirmed that the production of materials on Martian soil leads to greater mechanical efficiency, resulting in economic optimization and a reduction in production waste (thus environmental advantage).

Today, studies are still in the preliminary stages, and technologies are not yet discussed, mainly due to cost and time constraints. Sending unmanned probes is not as efficient as manned spacecraft, so the issue of supply and time is a hindrance, as launch windows between planets and Earth do not allow for useful and feasible journeys.

However, I am confident that these goals will be achieved in the future, even if not in the immediate future. Therefore, medicine and fluid dynamics may also require a careful examination of the space environment so that the human factor can be considered in missions.

References

[1] M. Abramowitz and I. A. Stegun. *Handbook of Mathematical Functions with Formulas, Graphs, and Mathematical Tables, 9th printing.* New York: Dover, 1972, p. 928.

[2] D.J. McComas et al. “Evolving outer heliosphere: Large-scale stability and time variations observed by the Interstellar Boundary Explorer”. In: *JOURNAL OF GEOPHYSICAL RESEARCH* 115 (2010).

[3] E. Grun et al. “Interstellar dust in the heliosphere”. In: *Astronomy and Astrophysics* (1994).

[4] Fathallah Alouani-Bibi et al. “KINETIC VERSUS MULTI-FLUID APPROACH FOR INTERSTELLAR NEUTRALS IN THE HELIOSPHERE: EXPLORATION OF THE INTERSTELLAR MAGNETIC FIELD EFFECTS”. In: *The Astrophysical Journal* (2011).

[5] J. R. Szalay et al. “The Heliosphere’s Interaction with Interstellar Dust”. In: *Heliophysics 2050 White Papers* (2021).

[6] J.D. Richardson et al. “Observations of the Outer Heliosphere, Heliosheat, and Interstellar Medium”. In: *Space Science Review* (2022), pp. 1–42.

[7] M. Baiesi et al. “Possible nonequilibrium imprint in the cosmic background at low frequencies”. In: *Physical Review Research* (2020), pp. 1–16.

[8] M.E. Hill et al. “Galactic Cosmic Rays Near the Interstellar Interface”. In: *Heliophysics 2050 White Papers* (2021).

[9] P.C. Frisch et al. “Mapping the Interstellar Magnetic Field Around the Heliosphere with Polarized Starlight”. In: (2018).

[10] R. Khatri et al. “Mixing of blackbodies: entropy production and dissipation of sound waves in the early Universe”. In: *Astronomy & Astrophysics Worldwide astronomical and astrophysical research* (2012).

[11] Stefano Marmi Antonio fasano. *Analytical Mechanics: An introduction.* Oxford: OUP Oxford, 2006.

[12] C. W. Smith Beau R. Bellamy Iver H. Cairns. “Voyager spectra of density turbulence from 1 AU to the outer heliosphere”. In: *JOURNAL OF GEOPHYSICAL RESEARCH* 110 (2005).

[13] P. Burgatti. *Lezioni di meccanica razionale.* Bologna: Zanichelli, 1919.

[14] NASA: GODDARD SPACE FLIGHT CENTER. *OMNIWeb Service.* `https://omniweb.gsfc.nasa.gov/`. Accessed: 2022. 31/12/2020.

[15] NASA JPL Eye. *Voyager 1.* `https://eyes.nasa.gov/apps/orrery/#/sc_voyager_1`. Accessed: 20/09/2023. 2021.

[16] Federico Fraternale. "Internal waves in fluid flows. Possible coexistence with turbolence." PhD thesis. Politecnico di Torino, 2017.

[17] A. Porporato J. Yin L. Rondoni. "Small Eartu Fluctuations: inexorable progression of climate change by asymmetric temperature extremes". In: (2023), pp. 1–13.

[18] Seth Redfield Jeffrey L. Linsky. "What Lies Outside of the Heliopause: Connecting the Outer Heliosphere with the Interstellar Medium". In: *Heliophysics 2050 White Papers* (2020).

[19] M. G. Kendall. *The Derivation of Multivariate Sampling Formulae from Univariate Formulae by Symbolic Operation.* Ann. Eugenics 10, 1940, pp. 392–402.

[20] W. S. Kendall and O. Barndorff-Nielson. *Current Trends in Stochastic Geometry: Likelihood and Computation.* Boca Raton, 1998.

[21] J. F. Kenney and E. S. Keeping. *Mathematics of Statistics, Pt. 2nd ed.* Priceton, 1951.

[22] J. F. Kenney and E. S. Keeping. *Moments About the Origin.* Priceton, 19 et 3, pp. 91–92.

[23] J. F. Kenney and E. S. "Skewness." §7.10 Keeping. *Mathematics of Statistics, Pt. 1, 3rd ed.* Priceton, 1962, pp. 100–101.

[24] J. Kratky and J. et al. Reinfelds. *Tables of Crude Moments Expressed in Terms of Cumulants.* University of Georgia, Athens, 1972.

[25] S. Lancelotti. *Analisi matematica II.* Torino: CELID, 2017.

[26] Ernst Paunzen Martin Piecka. "Mapping Local Interstellar Medium With Diffuse Interstellar Bands". In: *MNRAS* (2020).

[27] G. P. Zank et al. P. Mostafavi. "Shock Waves Propagation Beyond the Heliosphere: How Far Does the Sun's Influence Extend into the Interstellar Medium?" In: *Heliophysics 2050 White Papers* (2021).

[28] A. Papoulis. *Probability, Random Variables, and Stochastic Processes, 2nd ed.* New York: McGraw-Hill, 1984.

[29] P. J. Smith. *A Recursive Formulation of the Old Problem of Obtaining Moments from Cumulants and Vice Versa.* Amer. Stat. 49, 1995, pp. 217–218.

[30] The planetary society. *The Voyager missions.* `https://www.planetary.org/space-missions/voyager`. Accessed: 06/2023. 2021.

[31] A. Stuart and J. K Ord. "Kendall's Advanced Theory of Statistics, Vol. 1: Distribution Theory, 6th ed." In: *Oxford University Press* (1998).

[32] Y.G. Malama V.V. Izmodenov M. Gruntman. “Interstellar hydrogen atom distribution fuction in the outer heliosphere”. In: *JOURNAL OF GEOPHYSICAL RESEARCH* 106 (2001).